August 5, 2026

REPORT#E26-358

Repeatability, Testing, and Rating of HRV and ERV Technologies using CSA SPE-18:24

Prepared For NEEA:
John Arthur Wilson
Sr. Product Manager | Commercial HVAC

Prepared By:
Jie Ma, Research Scientist
Zicheng Wang, Research Scientist

Center for High-Performance Buildings,
Purdue University
585 Purdue Mall
West Lafayette, IN 47907

By accessing or downloading any Content from NEEA's Sites, you acknowledge and agree you read, understand, and will comply with NEEA's [Privacy and Terms of Use] and further understand NEEA retains all rights of ownership, title, and interests in the Sites and Content. You may not share, sell, or use the Content except as expressly permitted by NEEA's [Privacy and Terms of Use] without NEEA's prior written consent of its [legal counsel].

©2026 Copyright NEEA

Northwest Energy Efficiency Alliance
PHONE
503-688-5400
EMAIL
info@neea.org

Contents

Summary

This study presented a systematic laboratory evaluation of four commercial HRV/ERV units — a plate-type HRV (Unit A), two plate-type ERV (Unit B and Unit D), and a wheel-type ERV (Unit C)— tested in accordance with SPE-18:24 (CSA, 2024), load-based and climate-specific testing and rating procedures for seasonal performance of heat recovery and energy recovery ventilators (HRVs and ERVs). The work was structured around five primary objectives: evaluating the practical implementation of the standard, assessing test repeatability, developing and applying airflow-dependent empirical performance models, characterizing crossflow leakage behavior through tracer gas testing, and providing actionable technical feedback to support the continued refinement of SPE-18:24.

Energy performance testing was conducted across a range of prescribed indoor and outdoor boundary conditions, airflow settings, and operating modes. Core performance metrics — including net and recovered sensible and latent heat, apparent and sensible recovery effectiveness, and sensible heat recovery efficiency — were calculated in accordance with the standard's definitions. Measurement uncertainty was explicitly propagated through all computed metrics to quantify confidence in the reported results. Repeated independent tests conducted on each unit under nominally identical conditions demonstrated good repeatability across all four units, with measured performance exhibiting only modest test-to-test variability. Importantly, when these data were used to calibrate airflow-dependent empirical models and to drive seasonal simulations, the resulting variability in Seasonal Coefficient of Performance (SCOP) was found to be small. This finding confirms that SPE-18 test data provide a sufficiently robust basis for model-based seasonal performance evaluation, even in cases where individual test-point uncertainties are not negligible.

Airflow-dependent models for fan power and heat exchanger effectiveness were developed from the experimental datasets and subsequently applied to seasonal simulations across eight representative climate zones (as defined in SPE-18, Annex B): subarctic, very cold, cold and dry, cold and humid, marine, mixed hot and dry, and hot and humid. The resulting SCOP values, computed for both cooling and heating modes, reflected meaningful differences across unit technologies and frost control strategies. In computing SCOP values, this analysis deviated from SPE-18 in two ways. First, SPE-18 specifies calculating an annual SCOP ("$SCOP_{total}$"), along with SCOPs calculated individually for cooling and heating but using only occupied or only unoccupied hours ("$SCOP_{mode}$"). To better represent overall seasonal performance, and allow comparison to rated HVAC seasonal efficiencies, the SCOPs discussed in this analysis were refactored to include all cooling hours ("cooling SCOP"), and all heating hours ("heating SCOP"), each including both occupied and unoccupied hours for the respective season. Second, the cooling SCOP computation in SPE-18 includes latent recovery (unlike heating SCOP where latent is omitted because heating in the prototype building was deemed to be a sensible-only process). However, the determination of whether latent energy transfer is beneficial (when the sign is negative) or not is rather arbitrary, and depends heavily on climate and design objectives. Although the latent component of the cooling SCOPs are shown in figures throughout this analysis, the discussion is limited to the sensible component of SCOP only. Both of these changes are incorporated into the recommendations for any future work derived from SPE-18.

In this study, Unit A, operating as a sensible-only plate-type HRV, exhibited heating SCOP that was strongly penalized in cold climates by the activation of its electric preheater, while maintaining relatively stable cooling SCOP across all zones. Unit B, a plate-type ERV capable of both sensible and latent exchange, demonstrated substantially similar cooling and heating SCOPs when observing the sensible component of cooling performance. Unit C, the wheel-type ERV employing a shutdown-based defrost strategy, exhibited the most favorable heating SCOP across all climate zones due to the absence of resistive preheating, while its sensible cooling performance was reduced substantially, mostly due to the additional energy requirement of the wheel motor. Unit D, a plate-type ERV utilizing a duty-cycle-based frost control strategy, similarly achieved high heating SCOP across all climate zones, with only moderate degradation in the coldest regions, demonstrating the energetic advantage of intermittent fan suspension over continuous preheating. The sensible cooling SCOP for unit D was between that of units A and B, and that of unit C.

Tracer gas testing was conducted to characterize crossflow leakage and exhaust air transfer for the plate-type HRV and wheel-type ERV. The plate-type unit exhibited predominantly pressure-driven leakage behavior, with the direction and magnitude of the static pressure differential governing the direction and degree of transfer. The wheel-type unit demonstrated measurable transfer even under pressure conditions expected to suppress leakage in a fixed-plate core, reflecting additional transfer mechanisms including rotational carry-over and seal-related effects. Both sets of results highlight the diagnostic value of tracer gas testing, while also underscoring its technical demands in terms of instrumentation, environmental control, and operational cost.

Based on the collective findings, several high level recommendations are offered for the refinement of SPE-18. First, the most severe low-temperature test condition (Condition F) proved difficult to reliably achieve and sustain under laboratory conditions, and a single low-temperature condition is insufficient to adequately characterize the wide range of manufacturer-specific frost control strategies encountered across different unit designs. It is recommended that low-temperature test procedures be made optional and structured in a manner that is adapted to the declared frost control strategy of the unit under test, rather than applying a uniform test sequence irrespective of control logic. Second, manufacturers should be required to explicitly classify their frost control strategy — whether by airflow modulation, electric preheating, intermittent fan cycling, wheel speed modulation, or protective shutdown, including any multi-stage strategies, to allow test procedures and performance interpretations to be properly tailored. Third, tracer gas testing should be maintained as an optional component of the standard rather than elevated to a mandatory requirement, given the specialized infrastructure and high cost, and its limited applicability in laboratories primarily focused on energy performance evaluation. The test should also be reconfigured to be conducted in a closed-loop test configuration to minimize waste of tracer gas. Finally, a number of specific recommendations are made, to correct errors and to modify or clarify test procedures so that in can be conducted consistently.

In conclusion, SPE-18 provides a technically sound and practically implementable framework for laboratory-based performance characterization and seasonal efficiency evaluation of HRV/ERV systems. The results of this study demonstrate that the standard generates data of sufficient quality and repeatability to support empirical model development and climate-specific SCOP assessment across diverse unit technologies and operating strategies. The recommendations presented herein are intended to strengthen the standard's ability to capture real-world operational behavior — particularly under low-temperature conditions — and to improve the consistency, interpretability, and practical accessibility of the resulting performance data across a broad range of laboratory environments.

1 Introduction

Space heating and cooling represent a significant fraction of total energy consumption in commercial buildings in the United States. As building envelopes continue to improve in airtightness to reduce uncontrolled infiltration losses, mechanical ventilation has become the primary mechanism for supplying outdoor air required to maintain acceptable indoor air quality. While essential, ventilation introduces substantial sensible and latent loads associated with conditioning outdoor air, thereby increasing HVAC energy use. Energy recovery ventilators (ERVs) and heat recovery ventilators (HRVs) mitigate this penalty by transferring heat and, in the case of ERVs, moisture between exhaust and supply airstreams, reducing the net ventilation load imposed on the primary HVAC system. ERVs and HRVs are implemented using several heat exchanger configurations, including plate-type, rotary, and heat pipe systems. Regardless of configuration, the performance of ERV/HRV systems depends on a complex interaction of airflow rate, heat exchanger characteristics, fan and motor heat addition, and embedded control strategies. Consequently, ERV/HRV performance cannot be adequately characterized by a single operating point or efficiency value, particularly when performance data are intended for use in energy modeling, system design, or seasonal performance evaluation.

To enable product comparison and support equipment certification, laboratory testing and rating standards have been developed for ERV and HRV systems. In North America, performance evaluation has historically relied on standards such as AHRI 1060 (AHRI, 2014) and CSA C439 (CSA, 2019), which define prescribed test conditions, measurement procedures, and performance metrics. These standards provide a consistent basis for rating equipment but are primarily structured around a limited number of fixed operating points and focus on heat or energy recovery effectiveness. Moreover, earlier standards were largely developed for traditional ERV/HRV configurations in which the tested device consisted of a heat or energy exchanger alone, without explicitly accounting for integrated components such as supply and exhaust fans, preheaters, defrost systems, or advanced control strategies. As ERV/HRV systems have evolved into increasingly integrated and actively controlled units, the limitations of fixed-condition rating approaches have become more pronounced. Performance data generated under legacy standards provide limited insight into airflow-dependent behavior, interactions between recovered energy and fan power consumption, or performance variations across different operating modes. These limitations constrain the usefulness of traditional ratings for performance mapping, system simulation, and annual energy analysis, particularly when ERV/HRV data are applied in whole-building energy models.

To address these limitations, a next-generation testing and rating methodology for ERV/HRV systems has been developed by the Canadian Standards Association and published as SPE-18. The methodologies underlying this special publication were developed through a multi-year research effort led by Purdue University in collaboration with the Northwest Energy Efficiency Alliance (NEEA). The intent of SPE-18 is to enable laboratory-based testing of ERV/HRV equipment in environmental chambers in a manner that supports performance mapping and subsequent energy analysis. Rather than relying on one to two prescribed rating points, the standard is structured to generate datasets suitable for developing empirical performance models. Under the SPE-18 framework, ERV/HRV performance is characterized over a range of airflow rates and inlet air conditions, with explicit consideration of integrated system components and operating modes such as cooling, heating, economizer operation, and frost protection. The resulting performance models are intended to capture both energy recovery and electrical power consumption, allowing predicted performance to be evaluated under climate-specific weather conditions. In this way, SPE-18 represents a shift from single-condition equipment ratings toward model-based seasonal performance assessment across multiple representative climates.

This shift in scope places increased importance on the quality and consistency of laboratory test data. When laboratory measurements are used to train empirical models, test-to-test variability can influence model coefficients and, in turn, predicted seasonal energy outcomes. Although SPE-18 defines testing procedures and data requirements, it does not prescribe repeatability criteria or statistical acceptance thresholds. Nevertheless, understanding repeatability is essential for evaluating the practical implementation of the standard and for interpreting the robustness of the performance models derived from the test data.

In the context of the this study, repeatability is therefore used as an analytical tool to assess the reliability and usability of the SPE-18 testing methodology. Repeated tests conducted on the same unit under nominally identical conditions provide insight into the sensitivity of measured performance to experimental uncertainty, control behavior, and transient effects. Assessing repeatability is particularly important when performance data are aggregated across multiple operating points to develop airflow-dependent performance models. Variability at individual test points can propagate through the modeling process and affect predicted seasonal efficiency, especially when electrical power consumption and energy recovery are evaluated simultaneously. A structured repeatability analysis therefore provides essential context for interpreting both laboratory results and model-based seasonal performance estimates generated under the SPE-18 framework. The present project addresses these issues through a systematic laboratory evaluation of four ERV and HRV units tested in accordance with SPE-18. The main objectives of this research are as follows:

a) To provide an overall evaluation of the SPE-18 test procedures, with particular emphasis on identifying practical challenges, sources of ambiguity, and potential points of misinterpretation when applying the standard in a laboratory environment.

b) To assess test repeatability as a means of evaluating the reliability of the performance data generated under the new standard, and to examine how experimental variability influences performance modeling and seasonal efficiency assessment.

c) To develop and apply airflow-dependent performance models based on the laboratory test data, incorporating both energy recovery and electrical power consumption, in order to demonstrate the application of the SPE-18 framework to seasonal performance evaluation.

d) To evaluate crossflow leakage between supply and exhaust air streams of different HRV/ERV technologies and evaluate method of test of leakage. Testing for crossflow leakage is currently a required test in SPE-18.

e) To provide specific, actionable technical feedback to the CSA committee and related stakeholders, supporting future refinement of SPE-18 and facilitating its effective implementation for ERV/HRV performance evaluation.

Through these objectives, this work contributes to the validation and refinement of a next-generation ERV/HRV testing and rating methodology, with the goal of improving the reliability, transparency, and practical usefulness of laboratory-based performance data for energy modeling and seasonal efficiency assessment.

2 Energy Performance Testing

The performance testing methodology adopted in this study is primarily based on the requirements and procedures outlined in CSA SPE-18, supplemented by established experimental practices developed in previous laboratory investigations conducted at Purdue University.

2.1 Testbed configuration

The experiments were conducted in a controlled laboratory environment consisting of a pair of psychrometric chambers, where both temperature and humidity were regulated within acceptable accuracy limits. One chamber was used to emulate indoor conditions, while the other simulated outdoor conditions. The unit was mounted in either the indoor or outdoor chamber, depending on whether it was designed for indoor or outdoor installation, respectively. Mounting a test unit in its appropriate chamber allows factors such as the unit casing's thermal transmittance and air leakage to be accounted for automatically during testing. In this study, all four test units were installed in the outdoor chamber.

As illustrated in Figure 2.1, the experimental setup consisted of two independent open-air circuits: an outdoor–supply air (OA–SA) circuit and a room–exhaust air (RA–EA) circuit. In the OA–SA circuit, outdoor air (OA) entered the test unit through a short, straight duct section and was discharged into the indoor chamber as supply air (SA). In the RA–EA circuit, room air (RA), also referred to as extract air (EXA), was drawn from the indoor chamber into the ERV unit and exhausted to the outdoor chamber as exhaust air (EA). Four measurement stations were installed along the ductwork at the inlet and outlet of both air streams, as shown in Figure 2.1. These stations were used to measure the key thermodynamic and flow parameters required for performance evaluation. The measured variables and corresponding instrumentation are described in detail below.

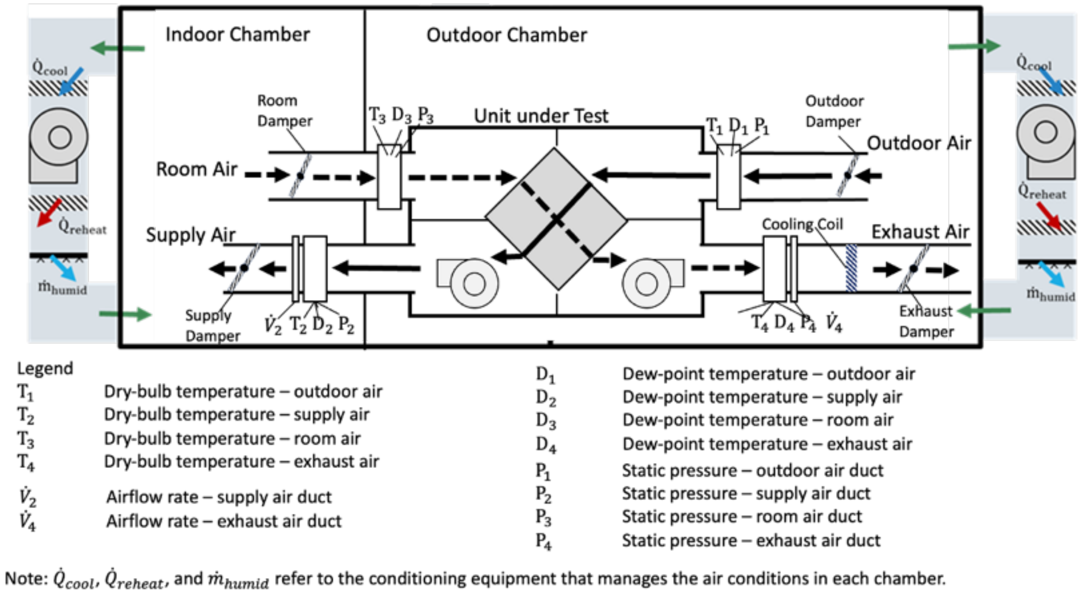

Figure 2.1: ERV performance testbed configuration.

Temperature and humidity measurement

Dry-bulb and dew-point temperatures at the OA and RA inlet stations, as well as at the SA and EA outlet stations, were measured to characterize the entering and exiting air conditions. The dry-bulb temperature at each station was measured using a 3×3 thermocouple grid, and the average value was used for analysis. Dew-point temperatures were measured using chilled-mirror hygrometers at all four stations. The absolute measurement uncertainty for both dry-bulb and dew-point temperatures was $\pm 0.1°C$.

Airflow measurement

The airflow rates of the two air streams were measured at the SA and EA stations, assuming constant flow in each loop (i.e., the OA and SA flow rates are approximately equal, as are the RA and EA flow rates). Ebtron airflow meters employing hot-wire anemometers were used at both stations. The relative measurement uncertainty of the airflow rate is $\pm 0.3\%$.

Static pressure measurement

The airflow resistance of the testbed was set prior to all testing. The target condition was to maintain an equivalent external static pressure difference across each air circuit, approximately 0.6 in H_2O at the nominal (i.e., full) airflow rate. Additional dampers were installed at the inlet or outlet sections of the ducts to achieve the desired resistance, as the inherent pressure drop of the system alone was less than 0.6 in H_2O.

The static pressure at each station was measured using differential pressure sensors, which recorded the pressure difference between the air in the duct and the surrounding atmospheric pressure.

Power measurement

The power input of all major components was measured using power transducers. The essential components in each test unit included the supply fan, exhaust fan. For units equipped with an electric preheater or enthalpy wheel, additional power transducers were installed to capture their power consumption. The measurement uncertainty of each power transducer was ±0.2%
.

2.2 Test conditions

Based on the standard, the testing conditions used in this study are summarized in Table 1. Conditions A and B correspond to cooling-mode operation, while Conditions C and D represent heating-mode operation. These four conditions (A–D) form the primary dataset used for subsequent performance evaluation, airflow-dependent model development, and repeatability analysis, as they span the representative operating envelope defined by the standard under normal cooling and heating conditions.

Conditions E and F were conducted under low-temperature operating conditions and were specifically designed to investigate unit behavior in cold-climate applications. These tests were used to assess low-temperature performance characteristics — including frosting-related behavior and overall operational stability under extreme cold conditions — rather than to support regression-based performance modeling. Condition F is applicable to long-duration cold-climate test only and was not successfully tested due to limitations of the test facility.

Test	**Outdoor**		**Indoor**	
	Dry-bulb (°C / °F)	Wet-bulb (°C / °F)	Dry-bulb (°C / °F)	Wet-bulb (°C / °F)
A	35 (95)	26.1 (78.9)	24 (75.2)	17 (62.6)
B	30 (86)	21.9 (71.4)		
C	10 (50)	4.5 (40.1)		
D	0 (32)	−3.4 (25.9)	21 (69.8)	11.4 (52.5)
E*	−10 (14)	−12 (10.4)		
F†	−25 (−13)	−25.7 (−14.3)		

* Optional test, used to estimate parameters for frost control.
† Applicable to long-term cold-climate testing only.

Table 1: Outdoor and indoor air conditions for test cases

2.3 Testing tolerance

Although the applicable testing standards do not prescribe a mandatory tolerance, maintaining appropriate airflow and energy balance during testing is considered critical to ensuring data quality and result credibility.

Maintaining airflow rate balance between the supply air (SA) and exhaust air (EA) streams is a fundamental requirement for accurate performance evaluation of HRV/ERV systems and for proper building operation. In practical applications, the outdoor air supplied to a space should be approximately balanced with the exhaust air removed in order to maintain near-neutral indoor pressure, apart from temporarily unbalanced flow, which may be a legitimate function or stage of a frost control strategy. Significant airflow imbalance may result in unintended building pressurization or depressurization, leading to increased uncontrolled infiltration or exfiltration, elevated heating and cooling loads, and potential moisture-related durability concerns.

In addition, conducting an energy balance check between the two air circuits of the test unit remains an essential diagnostic procedure for assessing measurement consistency and identifying potential instrumentation or data-processing errors. Agreement between the independently calculated heat transfer rates on the two airstreams provides confidence in the validity of the measured temperatures, humidity ratios, airflow rates, and associated performance metrics.

2.3.1 Airflow rate balance

From a testing and performance evaluation perspective, most heat and energy recovery metrics are derived under the assumption of balanced mass flow rates on the supply and exhaust sides. Airflow imbalance alters the heat capacity rates of the two air streams and changes the effective driving potential for heat and mass transfer within the heat exchanger. If not properly controlled or accounted for, this imbalance can introduce systematic bias in calculated effectiveness values, particularly under part-load or low-flow operating conditions.

Airflow rate balance is assessed by comparing the measured supply and exhaust volumetric flow rates at each test condition. The airflow imbalance is quantified as:

$$\Delta_{\text{airflow}} = \frac{\left|\dot{Q}_{\text{SA}} - \dot{Q}_{\text{EA}}\right|}{\left(\dot{Q}_{\text{SA}} + \dot{Q}_{\text{EA}}\right)/2} \times 100\% \tag{2.1}$$

where $\dot{Q}_{\text{SA}}$ and $\dot{Q}_{\text{EA}}$ denote the supply and exhaust airflow rates in $m^3/s(ft^3/min)$, respectively.

In this study, airflow rate balance was verified for all test points prior to performance analysis. The supply and exhaust airflow rates were maintained within $\pm 10\%$ imbalance for all test conditions, ensuring compliance with the prescribed airflow balance tolerance.

Energy balance

In this study, the energy balance is evaluated across the heat exchanger core (HX-core) only, and does not include sensible heat added by the supply or exhaust fans. This distinction is essential because fan motor heat is introduced downstream or upstream of the HX-core and does not represent heat transfer attributable to the recovery device itself.

For a physically consistent measurement, the sensible heat transferred through the HX-core and calculated from the supply air side should match that calculated from the exhaust air side within the bounds of measurement uncertainty. Deviations from this balance may indicate errors in airflow measurement, temperature measurement bias, unaccounted heat losses to the surroundings, or incorrect attribution of fan heat.

The sensible heat transfer rate across the HX-core is calculated independently from the supply and exhaust air sides as:

$$\dot{q}_{s,\mathrm{SA,core}} = \dot{m}_{\mathrm{SA}}\, c_{p,SA}\, (T_{\mathrm{SA}} - T_{\mathrm{OA}}) - \dot{q}_{\mathrm{in,SF}} - \dot{q}_{\mathrm{in,D}} - \dot{q}_{\mathrm{in,Saux}} \tag{2.2}$$

$$\dot{q}_{s,\mathrm{EA,core}} = \dot{m}_{\mathrm{EA}}\, c_{p,\mathrm{EA}}\, (T_{\mathrm{EA}} - T_{\mathrm{RA}}) - \dot{q}_{\mathrm{in,EF}} - \dot{q}_{\mathrm{in,D}} - \dot{q}_{\mathrm{in,Eaux}} \tag{2.3}$$

where:
$\dot{m}_X$ = mass flow rate of the outdoor air stream measured at SA and EA stations, $kg/s[lbm/s]$;
c_p = specific heat of air,$kJ/(kg \cdot K)[Btu/(lbm \cdot {}^\circ F)]$;
T_X = dry-bulb temperature in $^\circ C(\ ^\circ F)$ respectively at OA, SA, RA and EA stations;
$\dot{q}_{\mathrm{in,SF/EF}}$ = the power of air-moving fan(s) in the supply air(SA) or exhaust air (EA), $kJ/h[Btu/h]$;
$\dot{q}_{\mathrm{in,D}}$ = the power of any frost control heater, $kJ/h[Btu/h]$;
$\dot{q}_{\mathrm{in,Saux/Eaux}}$ = the power of any additional heat-producing device located in the air stream (such as a rotary wheel motor), $kJ/h[Btu/h]$;

The sensible energy balance deviation (Δq_{sen}) is expressed as:

$$\Delta q_{\mathrm{sen}} = \frac{|\dot{q}_{\mathrm{sen,SA,core}} - \dot{q}_{\mathrm{sen,EA,core}}|}{(\dot{q}_{\mathrm{sen,SA,core}} + \dot{q}_{\mathrm{sen,EA,core}})\,/2} \times 100\% \tag{2.4}$$

For ERV units, the latent energy transfer associated with moisture exchange across the HX-core is evaluated using the change in humidity ratio. The latent heat transfer rate is calculated as:

$$\dot{q}_{l,\mathrm{SA,core}} = \dot{m}_{\mathrm{SA}}\, h_{fg}\, (\omega_{\mathrm{SA}} - \omega_{\mathrm{OA}}) \tag{2.5}$$

$$\dot{q}_{l,\mathrm{EA,core}} = \dot{m}_{\mathrm{EA}}\, h_{fg}\, (\omega_{\mathrm{EA}} - \omega_{\mathrm{RA}}) \tag{2.6}$$

where:
h_{fg} = latent heat of vaporization of water, taken as a constant in this study with a value of $= 244,309 J/kg$;
ω_X = humidity ratio in $kg_{water}/kg_{dry,air}(lbm_{water}/lbm_{dry,air})$, calculated from the measured dry-bulb temperature and dew-point temperature at the OA, SA, RA, and EA measurement stations.

The latent energy balance deviation (Δq_{lat}) is defined as:

$$\Delta q_{\text{lat}} = \frac{|\dot{q}_{\text{lat,SA}} - \dot{q}_{\text{lat,EA}}|}{(\dot{q}_{\text{lat,SA}} + \dot{q}_{\text{lat,EA}})\,/2} \times 100\% \tag{2.7}$$

Both sensible and latent energy balance deviations are evaluated for all test conditions and operating modes as a data quality check. Although no explicit acceptance tolerance is prescribed by the testing standard, an energy balance deviation within ±10% is considered acceptable for all tests, while deviations within ±5% are regarded as indicative of good measurement agreement. The calculated deviations for all four test units, across all test conditions, are reported in Figures 3.1, 3.5, 3.9, and 3.13, and are examined for magnitude and trends to confirm measurement consistency and to support confidence in the subsequent calculations of recovery effectiveness and recovered energy.

2.4 Energy performance evaluation

The energy performance of HRV and ERV units is determined by evaluating their ability to transfer sensible and latent energy between the supply and exhaust air streams under controlled operating conditions. Following verification of airflow rate balance and energy balance consistency, performance metrics are calculated to quantify both the magnitude and effectiveness of energy recovery attributable to the heat exchanger core as well as the overall unit. Accordingly, HRV/ERV energy performance is assessed using the following indicators, which collectively characterize sensible and latent heat recovery, moisture transfer, and overall system efficiency across the tested operating range.

2.4.1 Net and recovered heat

The sensible and latent recovered energy rates are defined as the heat transfer occurring within the heat exchanger core and is evaluated based on measurements in the outdoor air (OA) and supply air (SA) streams. When air temperatures and humidity are measured immediately upstream and downstream of the heat exchanger core, or obtained from the model, the sensible and latent recovered heat rate in the supply air stream are calculated as:

$$\dot{q}_{s,\text{SA,core}} = \dot{m}_{\text{SA}}\, c_{p,SA}\, (T_{\text{SA,core}} - T_{\text{OA,core}}) \tag{2.8}$$

$$\dot{q}_{l,\text{SA,core}} = \dot{m}_{\text{SA}}\, h_{fg,SA}\, (\omega_{\text{SA,core}} - \omega_{\text{OA,core}}) \tag{2.9}$$

Here, the subscript "core" denotes air properties evaluated at the inlet and outlet of the heat exchanger core, exclusive of any thermal influence from fan motors or auxiliary energy sources. It does, notably, include the influence of the rest of the system, including case losses (conductive and leakage) and cross-flow leakage.

When the recovered sensible heat is instead evaluated using temperatures measured at the measurement stations shown in Figure 2.1, the corresponding sensible recovered heat rate in the supply air stream is calculated as shown in Eq.2.2, with the heat contributions from the fan motor and other auxiliary devices removed.

In contrast, the net sensible recovered energy ($\dot{q}_{s,\mathrm{SA,net}}$) accounts for additional sensible heat introduced into the supply air stream by unit components located upstream or downstream of the heat exchanger core, including the supply fan and auxiliary devices. The net latent recovered energy ($\dot{q}_{s,\mathrm{SA,net}}$), is identical to the latent recovered energy, as no additional latent effects are introduced by these components. Accordingly, the net sensible and latent recovered heat rates in the supply air stream are calculated as:

$$\dot{q}_{s,\mathrm{SA,net}} = \dot{q}_{s,\mathrm{SA,core}} + \dot{q}_{\mathrm{in,SF}} + \dot{q}_{\mathrm{in,SD}} + \dot{q}_{\mathrm{in,Saux}} \tag{2.10}$$

$$\dot{q}_{l,\mathrm{SA,net}} = \dot{q}_{l,\mathrm{SA,core}} \tag{2.11}$$

The distinction between recovered and net energy enables separation of the intrinsic thermal performance of the heat exchanger core from the overall thermal impact of the complete HRV/ERV unit.

2.4.2 Apparent and sensible recovery effectiveness

The apparent sensible effectiveness ($\varepsilon_{s,\mathrm{app}}$) represents the ratio of the actual sensible heat transfer between the outdoor and supply air streams to the theoretical maximum sensible heat transfer achievable between the room air and outdoor air streams. This metric reflects the apparent thermal performance of the unit without explicitly correcting for fan heat contributions. The apparent sensible effectiveness is calculated as

$$\varepsilon_{s,\mathrm{app}} = \frac{\dot{m}_{\mathrm{SA}}\,(T_{\mathrm{SA}} - T_{\mathrm{OA}})}{\dot{m}_{\mathrm{min}}\,(T_{\mathrm{RA}} - T_{\mathrm{OA}})} \tag{2.12}$$

where:

$\dot{m}_{\mathrm{min}}$ = minimum mass flow rate between the supply air and room air streams, $kg/s(lbm/s)$;

In addition, the sensible and latent recovery effectiveness (ε_s and ε_l), exclusive of fan and auxiliary sensible heat impacts, are calculated as follows:

$$\varepsilon_s = \frac{\dot{m}_{SA} \times (T_{SA} - T_{OA}) - \dot{q}_{in,SF} - \dot{q}_{in,SD} - \dot{q}_{in,Saux}}{\dot{m}_{min} \times (T_{RA} - T_{OA})} \tag{2.13}$$

$$\varepsilon_l = \frac{\dot{m}_{SA} \times (\omega_{SA} - \omega_{OA})}{\dot{m}_{min} \times (\omega_{RA} - \omega_{OA})} \tag{2.14}$$

2.4.3 Adjusted sensible recovery efficiency

The metric of sensible heat recovery efficiency (SHRE) in SPE-18 is not defined properly, nor does it serve its intended purpose. SHRE is defined in Equation 17 of SPE-18, as the net energy transferred divided by the total energy input. Although originally intended as a coefficient of performance for individual test conditions, the concept was updated to be comparable to the adjusted sensible recovery efficiency (ASRE) as defined in C439, Equation 23, which is the net energy transferred divided by the available energy difference between the indoor and outdoor air streams. However, the equation in SPE-18 was not updated accordingly. While the test methods of SPE-18 and C439 differ, and the results are not entirely equivalent, this study will recommend redefining SHRE as ASRE to meet that objective, using the following equation:

$$ASRE = \frac{|\dot{q}_{s,SA,net}| - \dot{q}_{in,SD}}{|\dot{m}_{max} c_p (T_{RA} - T_{OA})| + \dot{q}_{in,ED}} \tag{2.15}$$

2.5 Uncertainty Propagation

Uncertainty in each derived performance metric is estimated using first-order (Taylor series) propagation, assuming the input measurements are independent. For any calculated quantity $y = f(x_1, x_2, ..., x_n)$, the combined standard uncertainty is:

$$u_y = \sqrt{\sum_{i=1}^{n} \left(\frac{\partial f}{\partial x_i}\right)^2 u_{x_i}^2} \tag{2.16}$$

where u_{x_i} is the standard uncertainty of the measured (or modeled) input x_i, and $\frac{\partial f}{\partial x_i}$ is the sensitivity coefficient that quantifies how strongly y changes with x_i.

To apply Eq. 2.16 for a specific metric (e.g.,recovered energy, effectiveness, or ASRE):

- Express the metric as an explicit function of its measured inputs (mass flow rate(s), temperatures, humidity ratios, and/or power terms);
- For each input, compute the sensitivity coefficient by perturbing that input by a small amount while holding all others constant, and record how much the metric changes;
- Multiply each sensitivity coefficient by the corresponding elemental uncertainty of that input;
- Sum all contributions in quadrature (square each term, add them, then take the square root) to obtain the combined uncertainty of the metric.

3 Analysis of Energy Performance Test Results

To comprehensively evaluate the thermal and moisture-transfer performance of the test units, a set of key performance parameters was calculated for each of the three repeated tests under operating conditions A to D. These parameters quantify the unit's ability to recover sensible and latent energy, characterize the heat-exchange process, and provide a consistent basis for comparing performance across airflow settings and environmental conditions. Specifically, the following metrics were computed:

- **Net sensible recovered energy**, representing the useful sensible heat recovered after accounting for fan-induced thermal gains or penalties.
- **Sensible recovered energy**, corresponding to the sensible heat exchange rate occurred only in the heat exchanger core.
- **Latent recovered energy**, corresponding to the latent heat recovered by the test unit.
- **Sensible and latent recovery effectiveness**, quantifying the fraction of the maximum possible sensible and latent heat transfer achieved under the measured (or modeled) temperature and humidity conditions.
- **Apparent sensible recovery effectiveness**, representing the ratio of the net sensible heat added to the supply airstream, including heat recovery and fan/auxiliary heating, to the maximum sensible recovered energy.
- **Adjusted sensible recovery efficiency**, providing an overall indicator of the unit's energy-recovery performance relative to the total thermal load imposed by the outdoor conditions.

Together, these parameters form a complete framework for assessing unit performance, enabling both a detailed diagnostic interpretation of individual heat- and mass-transfer behaviors and a robust comparison of operational characteristics across test conditions. Subsequent sections present the calculated results and discuss the observed trends, sensitivities, and implications for practical system operation.

In addition to the standard operating conditions, dedicated low-temperature test conditions are included to capture performance characteristics specific to cold-climate operation. The E condition is primarily intended to support parameter estimation for frost control modeling. The F condition extends this assessment to sustained low-temperature operation representative of long-term cold-climate exposure, where cumulative frost effects, defrost strategies, and associated performance degradation become critical. The extended test time of 72 hours is derived from C439, where the test period is not only to evaluate performance but is also effectively a "stress test" for cold climates. Together, these low-temperature conditions provide essential data for characterizing frost-related behavior and for ensuring that the derived performance models remain applicable to cold and very cold climate applications.

3.1 Plate HRV – Unit A

The first test unit evaluated in this study is a fixed-plate heat recovery ventilator (HRV), designed to facilitate sensible heat exchange exclusively between the supply and exhaust air streams, with no intentional moisture transfer across the heat exchanger core. Because of this configuration, the unit's performance is governed solely by dry-bulb temperature differences, making it well suited for isolating and characterizing sensible heat recovery behavior under controlled conditions. The unit is rated for a nominal airflow of 1000 CFM, which defines the reference operating point for performance evaluation and provides a consistent basis for comparison across test conditions and airflow settings.

3.1.1 Energy balance

Figure 3.1 compares the sensible heat transfer calculated from the OA–SA stream with that from the RA–EA stream to evaluate the sensible energy balance of Unit A, an essential diagnostic for verifying measurement accuracy. The data points for all four conditions cluster closely around the 1:1 line and remain within the ±5% bounds, indicating strong agreement between the two calculations and demonstrating that no significant bias or systematic error exists in the sensible heat-transfer measurements. This high level of conformity confirms the reliability of the instrumentation and data-processing procedures, providing confidence in the subsequent performance metrics derived from these measurements.

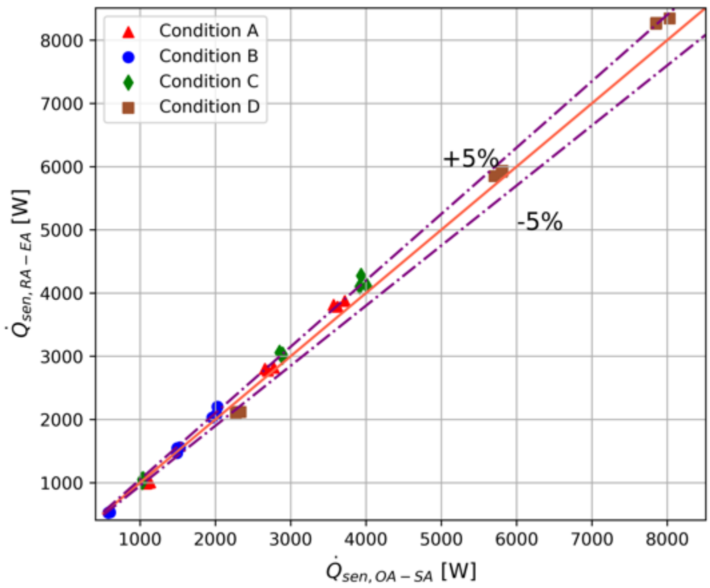

Figure 3.1: Sensible energy balance of unit A.

3.1.2 Recovery energy

Figure 3.2 presents the sensible energy recovery performance of Unit A under four testing conditions (A–D) at three airflow settings: 100%, 65%, and 25% of the maximum rated air flow (CFM_{max}). Figure 3.2 (a) shows the net recovered energy, which accounts for fan heat addition, whereas Figure 3.2 (b) presents the sensible recovered energy at the heat exchange core. Together, these results provide insight into both the thermal exchange characteristics of the HRV core and the impact of fan operation. Across all conditions, the sensible recovered energy decreases with airflow, reflecting the reduced heat available at lower mass flow rates. For each airflow setting, the three repeated tests exhibit strong repeatability, with deviations typically within a few percent, demonstrating stable and reliable thermal performance.

Condition A exhibits full-flow net recovered energy around 3100 W to 3250 W and core recovered energy around 3600 W to 3720 W. The difference between plots 3.2 (a) and 3.2 (b) highlights the effect of fan heat, which reduces the net sensible recovery by approximately 15% in cooling operation. At reduced flow (65% and 25% of CFM_{max}, both net and core values decrease proportionally, with repeatability maintained across tests. Condition B, representing a milder temperature differential, shows correspondingly lower recovered energy. At 100% flow, net recovery is approximately 1500 W to 1560 W, while recovery is slightly higher at 1960W to 2020W. This consistent offset across airflow levels confirms that fan heat contributes a significant reduction in net performance during cooling operation. Condition C yields higher recovered energy due to a larger indoor–outdoor temperature gradient. Full-flow net recovery ranges from 4370 W to 4470 W, with the corresponding recovery reaching nearly 5000 W. Condition D, the most severe thermal condition, shows the highest sensible recovery. C and D are heating conditions, and show the net recovery impact increasing from the addition of fan heat. Despite the larger magnitudes, the repeatability across the three test runs remains strong, and the relative impact of fan heat aligns with the trends seen in other conditions.

The comparison of net and sensible recovery demonstrates that:

- Sensible recovered energy scales predictably with airflow and thermal driving conditions.
- Fan heat addition consistently reduces the net energy recovery during cooling mode while increasing the net recovery during heating mode, with an impact that remains stable across tests and operating conditions.
- Test-to-test variability is low, indicating robust HRV performance and reliable measurement procedures.

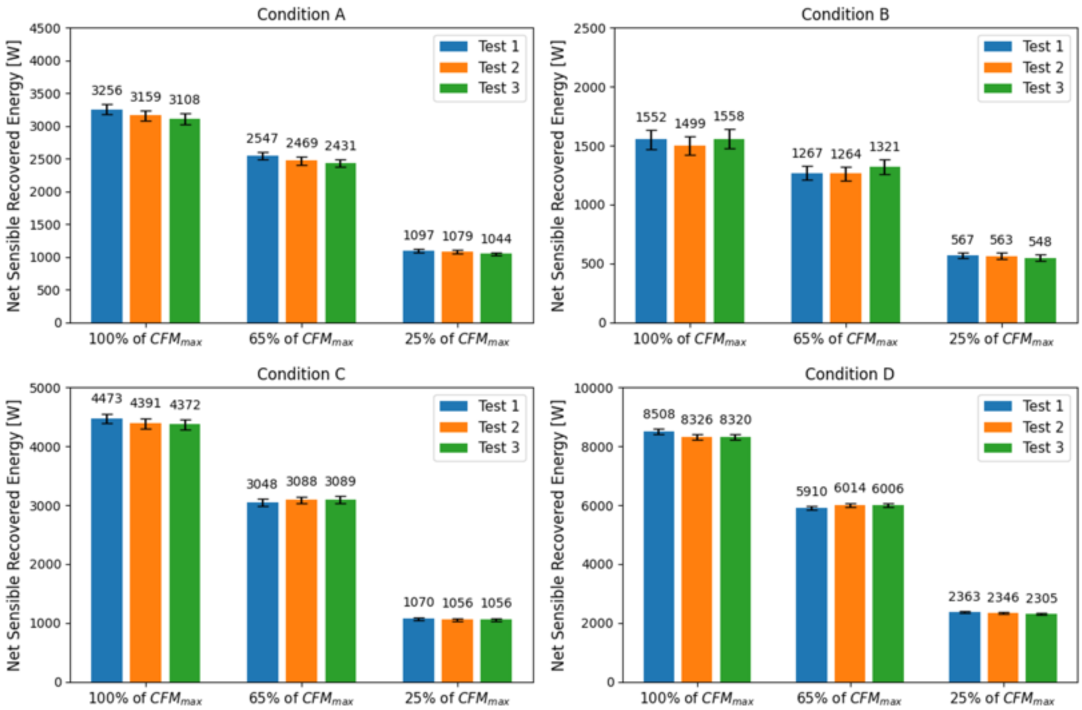

(a)

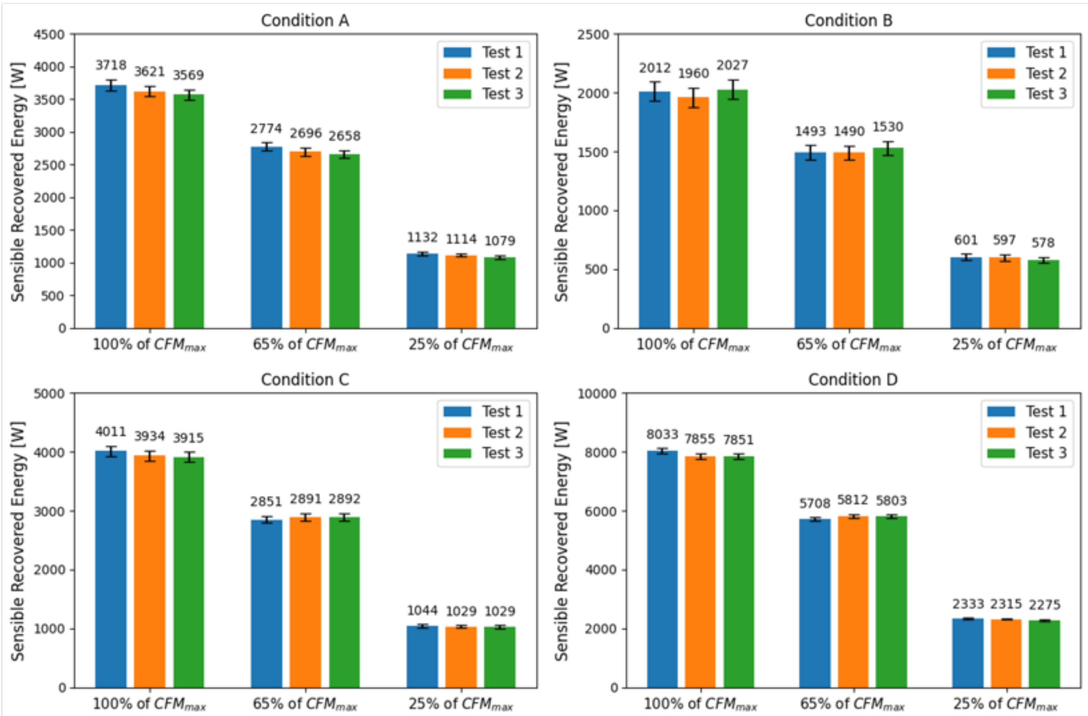

(b)

Figure 3.2: Recovered energy of Unit A: (a) Net recovered energy (including fan impact), and (b) recovered energy (at the heat exchanger core).

3.1.3 Recovery effectiveness

Figure 3.3 illustrates the sensible recovery effectiveness and the apparent sensible recovery effectiveness of Unit A across four conditions (A, B, C, and D) and three airflow levels at 100%, 65%, and 25% of rated airflow. The results reflect both the intrinsic heat-exchange capability of the core and, where indicated as "apparent", the influence of fan-induced thermal effects.

Across all conditions, the sensible recovery effectiveness remains consistently high, generally ranging between 0.73 and 0.87. At 100% and 65% airflow, effectiveness values are tightly clustered around 0.75 to 0.78 for all conditions, showing minimal dependence on the specific thermal boundary conditions. At 25% airflow, effectiveness increases modestly to approximately 0.84 to 0.87. This increase at low flow rates is expected since reduced airflow increases air residence time within the core, improving heat-transfer capability. The small variation among the three repeated tests indicates good measurement repeatability and confirms the stability of the sensible heat-exchange performance.

The apparent sensible recovery effectiveness, which incorporates the impact of fan heat addition on the supply and exhaust air streams, exhibits consistently lower values than the sensible recovery effectiveness. This reduction reflects the penalty imposed by fan power, which introduces additional heat to the supply airstream and therefore diminishes the net sensible recovery. At 100% airflow, apparent effectiveness values range from approximately 0.56 to 0.67 across the four conditions, depending on the magnitude of fan power and the thermal conditions. As airflow decreases to 65% and 25% of full airflow, apparent effectiveness increases, consistent with lower fan power and reduced fan heat influence at reduced flow. For 25% airflow, the apparent effectiveness rises to approximately 0.82 to 0.88 for all conditions. The close alignment of the three test repetitions again demonstrates strong repeatability.

The comparison between sensible recovery effectiveness and apparent sensible recovery effectiveness highlights several important trends:

1) The HRV core exhibits inherently high and stable sensible heat-transfer performance, with effectiveness largely independent of environmental conditions and only moderately influenced by airflow.

2) Fan heat addition has a measurable impact, reducing the apparent sensible recovery effectiveness by 10–20% points in cooling conditions, and increasing it in heating conditions.

3) Both effectiveness metrics increase at lower airflow rates, driven by enhanced residence time and reduced fan heat addition (for apparent effectiveness).

4) Repeatability across all conditions and airflow rates is strong, indicating reliable and consistent HRV performance.

These results confirm that Unit A delivers robust sensible heat-recovery capability and that fan-related thermal effects must be incorporated when evaluating net performance for seasonal or system-level energy assessments.

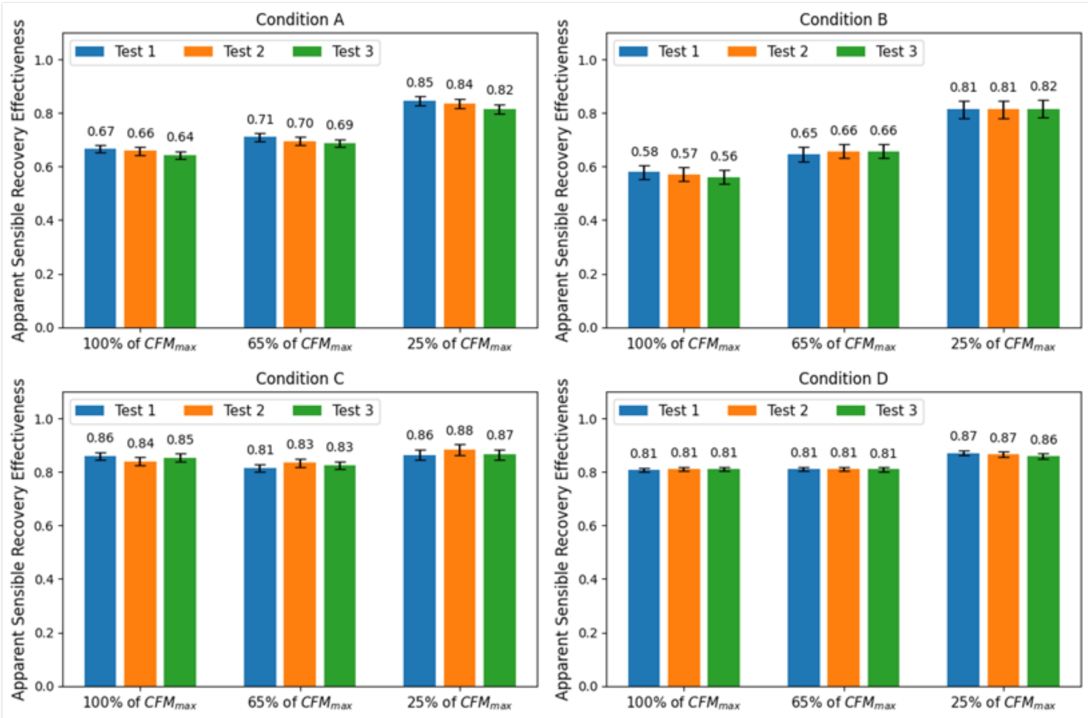

(a)

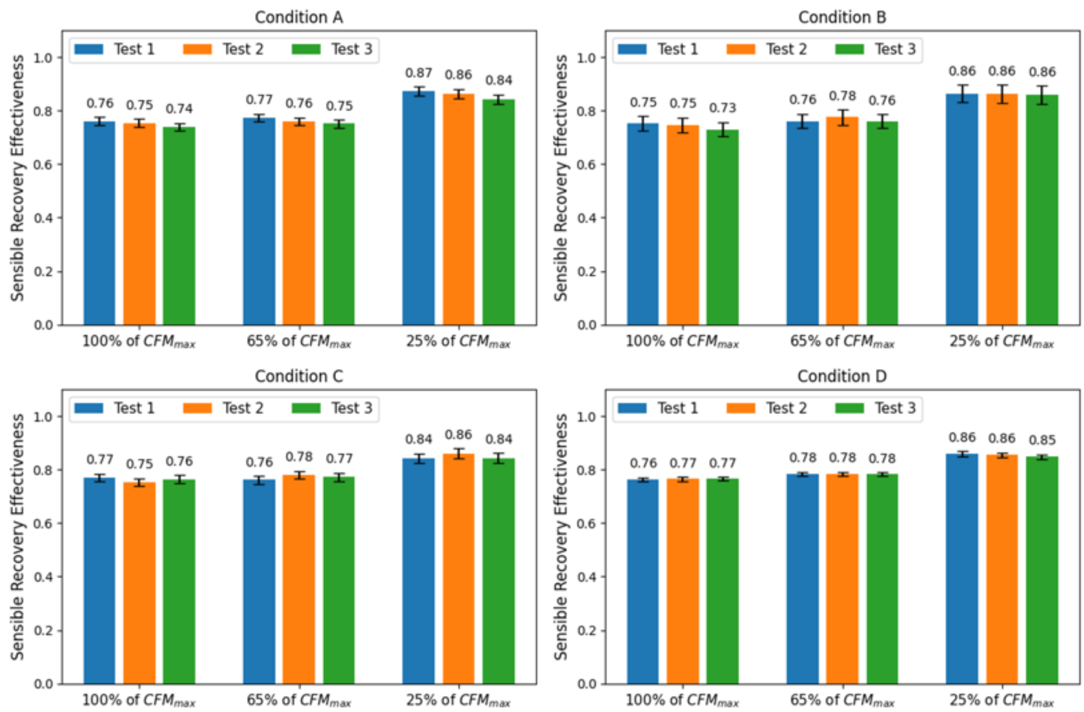

(b)

Figure 3.3: Recovery effectiveness of Unit A: (a) apparent sensible recovery effectiveness (including fan impacts), and (b) sensible recovery effectiveness (at the heat exchange core).

3.1.4 Adjusted sensible recovery efficiency

Figure 3.4 presents the adjusted sensible recovery efficiency (ASRE) of the HRV unit across four test conditions (A–D) at three airflow rates (100%, 65%, and 25% of maximum air flow), each measured across three repeated trials. Conditions C and D yielded the highest ASRE values, consistently in the range of 0.75–0.83, indicating strong sensible heat recovery performance under those operating parameters. Conditions A and B produced notably lower ASRE values (0.54–0.73), suggesting that the thermal or airflow conditions in those cases were less favorable for heat exchange efficiency. Repeatability across the three trials was excellent throughout. The maximum variation between any three tests at a given condition and flow rate was 0.03, demonstrating that the test methodology is highly reproducible and that the measured ASRE values are reliable.

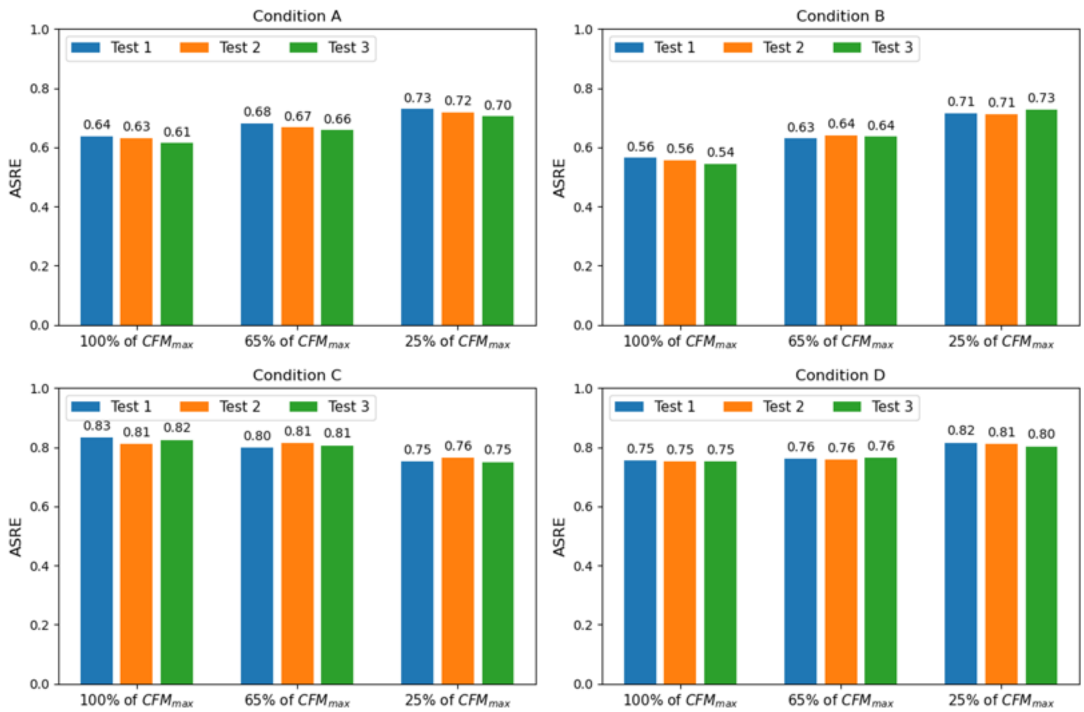

Figure 3.4: Adjusted sensible recovery efficiency (ASRE) for Unit A.

3.2 Plate ERV - Unit B

The second test unit, hereafter referred to as Unit B, is a plate-type ERV incorporating a fixed-core heat and moisture exchanger that transfers both sensible and latent energy between fully separated supply and exhaust air channels. The unit has a nominal airflow rate of 1000 CFM, with both the supply air (SA) and exhaust air (EA) fans located downstream of the heat recovery core.

3.2.1 Energy balance

Figure 3.5 evaluates the energy balance of Unit B by comparing the recovered sensible (top) and latent (bottom) energy measured on the room-air to exhaust-air (RA–EA) side with the corresponding values measured on the outdoor-air to supply-air (OA–SA) side. Perfect energy balance would result in a 1:1 relationship, represented by the solid diagonal line. The dashed lines denote a ±5% tolerance band, indicating acceptable agreement for both sensible and latent heat recovery measurements.

Across all operating conditions A to D, the measured data align closely with the 1 : 1 line, demonstrating that the ERV core maintains a consistent and symmetric energy transfer between the two airflow paths. Most points fall within the ±5% bounds, confirming good agreement between the RA–EA and OA–SA measurements and indicating minimal imbalance due to instrumentation error, leakage, or unaccounted fan heat effects. The clustering of data along the diagonal further reflects stable and repeatable performance across different environmental conditions and flow settings. The larger latent deviation for condition D is due to condensation that is not accounted for in the transfer equations, for the test duration.

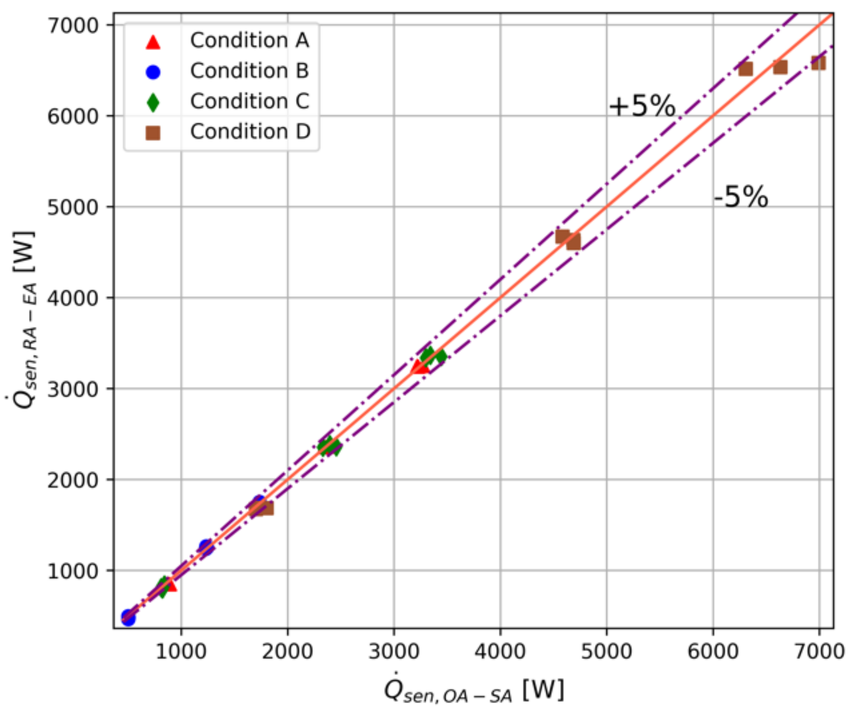

(a)

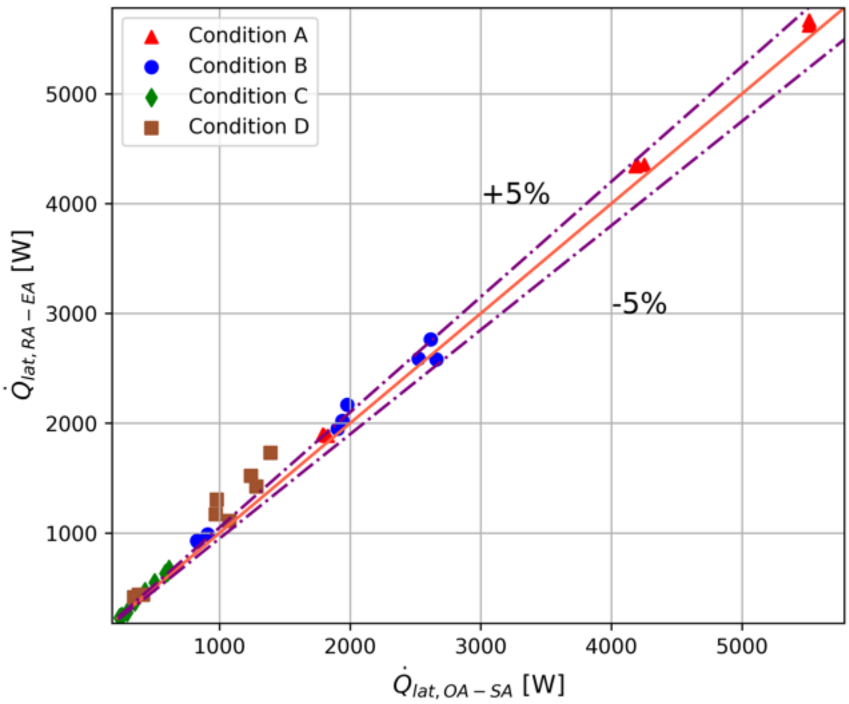

(b)

Figure 3.5: Energy balance of unit B: (a) sensible energy, and (b) latent energy.

3.2.2 Recovery energy

Figures 3.6 (a) to (c) summarize the recovered energy of Unit B across four test conditions A to D, and three airflow ratios (100% of CFM_{max}, 65% of CFM_{max}, and 25% of CFM_{max}). The axis scales differ across the figures for test conditions A, B, C, and D, reflecting the considerable variation in underlying values among the four conditions. Across all conditions, the three repeated tests exhibit small variations, demonstrating good experimental repeatability and confirming the consistency of the measurement methodology.

Figure 3.6 (a) shows the net sensible recovered energy generally increases with airflow rate, consistent with the higher heat transfer potential at larger volumetric flow. At 100% of CFM_{max}, Condition D produces the highest recovered sensible energy (approximately 6.7 kW to 7.4 kW), driven by the largest indoor–outdoor temperature differential. Conditions A and C follow, with A showing 2.7kW to 2.8 kW and C showing 3.75 kW to 3.90 kW. Condition B exhibits the lowest values , reflecting its smaller driving temperature difference. At the reduced airflow of 65% of CFM_{max}, the recovered energy decreases proportionally but retains the same ranking of conditions. At 25% of CFM_{max}, net sensible recovery falls to its minimum range, indicating the system's diminished capacity under low-flow operation.

The sensible recovered energy, shown in Figure 3.6 (b), exhibits similar trends to the net sensible results but without the correction for fan power or auxiliary loads. This allows the thermal performance of the heat-exchange core to be directly assessed. Across all airflow settings, the spread among the three repeated tests is less than 3%, confirming the stability of the system's sensible heat-transfer characteristics. Heavy-load conditions (Condition D) again produce substantially larger heat-transfer rates, reaching approximately 6.4 kW to 7.0 kW at full flow.

Comparison of Figures 3.6 (a) and 3.6 (b) demonstrates that the difference between the net and sensible recovered energy arises from the additional sensible heat imparted to the airstream by the fans. This parasitic heat load reduces the effective (net) sensible recovery relative to the value in cooling-mode operation, but increases it in heating mode where the added heat contributes beneficially to the total sensible energy gain.

Latent recovered energy exhibits stronger condition dependence, reflecting the humidity ratio gradients imposed in Conditions A to D. In Condition A, which features high indoor humidity, latent recovery is substantial—approximately 5.5 kW to 5.6 kW at 100% airflow and 4.2 kW to 4.3 kW at 65% airflow. These magnitudes demonstrate that the membrane subsystem is highly effective under moisture-rich operating conditions. Conversely, Conditions C and D exhibit markedly lower latent-energy recovery. The large error bars shown in Figure 3.6(c) indicate a higher level of uncertainty in the latent effectiveness. This is expected, as latent performance calculations depend on both dry-bulb temperature and dew-point temperature measurements, resulting in greater propagation of measurement uncertainty compared to sensible effectiveness.

In general, Unit B exhibits strong and repeatable thermal performance across all performance evaluation conditions. Sensible recovery is stable and scales predictably with airflow. Latent recovery is highly effective under high-humidity conditions but becomes measurement-sensitive as the humidity gradient decreases.

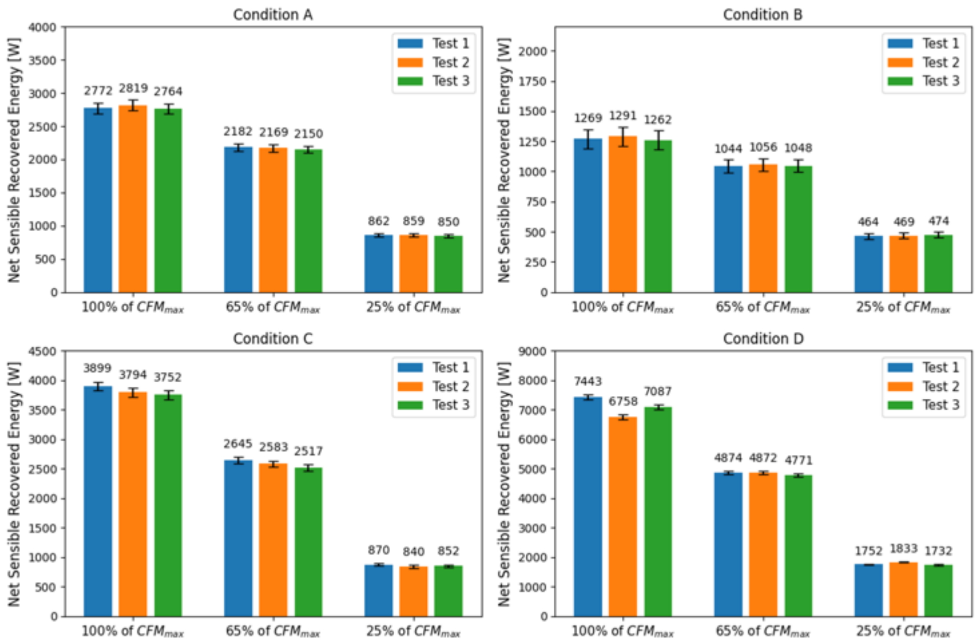

(a)

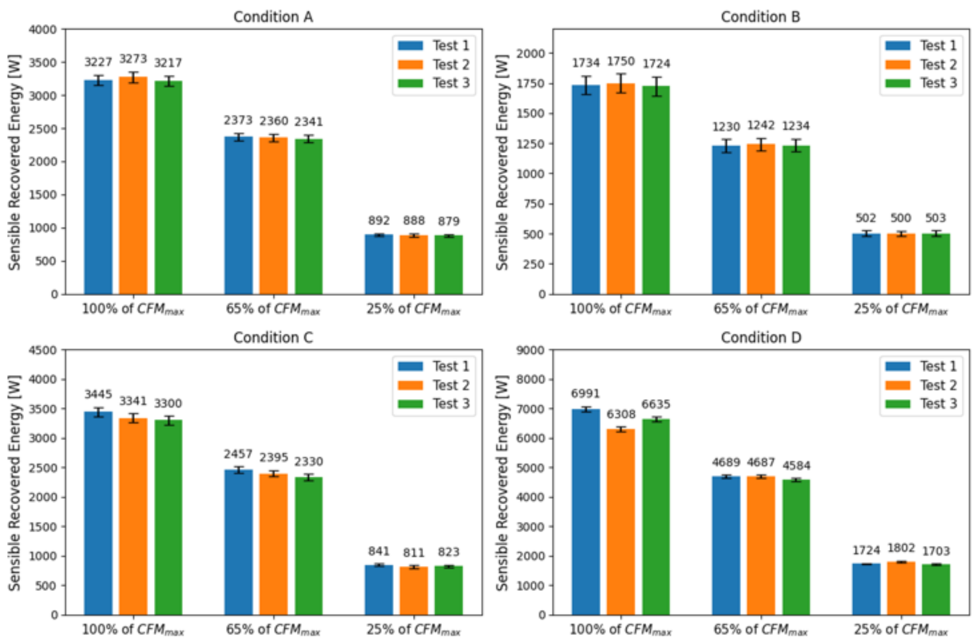

(b)

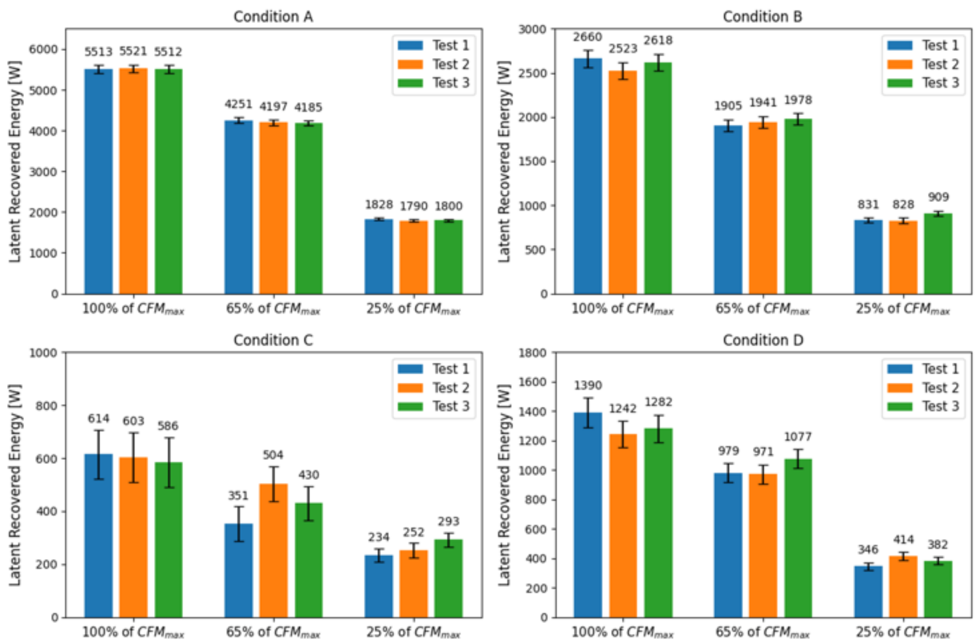

(c)

Figure 3.6: Recovered energy of Unit B: (a) Net sensible recovered energy (including fan impact), (b) sensible recovered energy (at the heat exchanger core), and (c) latent recovered energy.

3.2.3 Recovery effectiveness

Figure 3.7 summarizes the sensible, latent, and apparent sensible recovery effectiveness of Unit B for four performance test conditions A to D at three airflow settings (100%, 65%,and 25% of maximum airflow). Across all metrics, the three repeated tests exhibit minimal variation, demonstrating strong repeatability and stable ERV performance under controlled conditions.

In Figure 3.7 (a), the sensible recovery effectiveness remains consistently high, typically between 0.70 and 0.87, with modest increases at lower airflow rates. This trend reflects longer residence time within the plate core, which enhances sensible heat transfer. Differences among conditions are relatively small, indicating that sensible effectiveness is only weakly dependent on the indoor–outdoor temperature gradient for this plate-type ERV. In Figure 3.7 (b), the latent recovery effectiveness exhibits a similar dependence on airflow rate, increasing from approximately 0.55 to 0.63 at full airflow and from about 0.72 to 0.76 at 25% of the nominal flow rate. The higher values observed under Conditions A and C correspond to larger humidity differentials compared to Condition D. Under Condition D, the outdoor air temperature is lower than the indoor air dew-point temperature, resulting in condensation within the heat exchanger core, which reduces the apparent latent recovery effectiveness. As shown in 3.7 (c), the apparent sensible recovery effectiveness is lower than the sensible effectiveness at the same operating points under Conditions A and B but higher under Conditions C and D. It follows the same general pattern of improvement with decreasing airflow.

These results show that Unit B provides robust and predictable recovery effectiveness across a wide range of airflow and boundary conditions. The increasing trends at reduced airflow are consistent with expected heat- and mass-transfer behavior in plate ERV cores, while the close alignment of repeated measurements confirms the reliability of the experimental data.

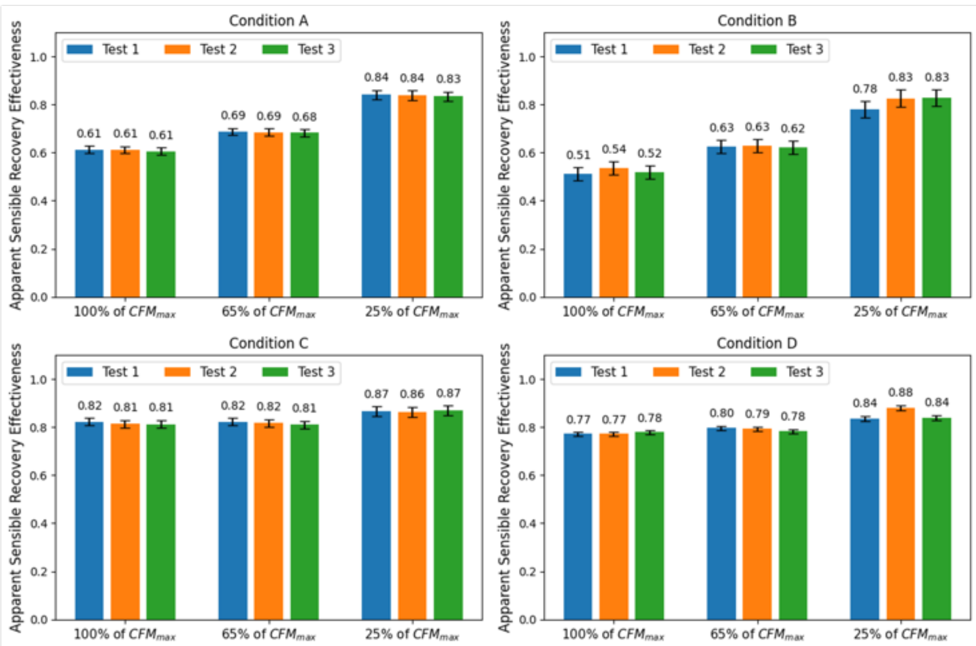

(a)

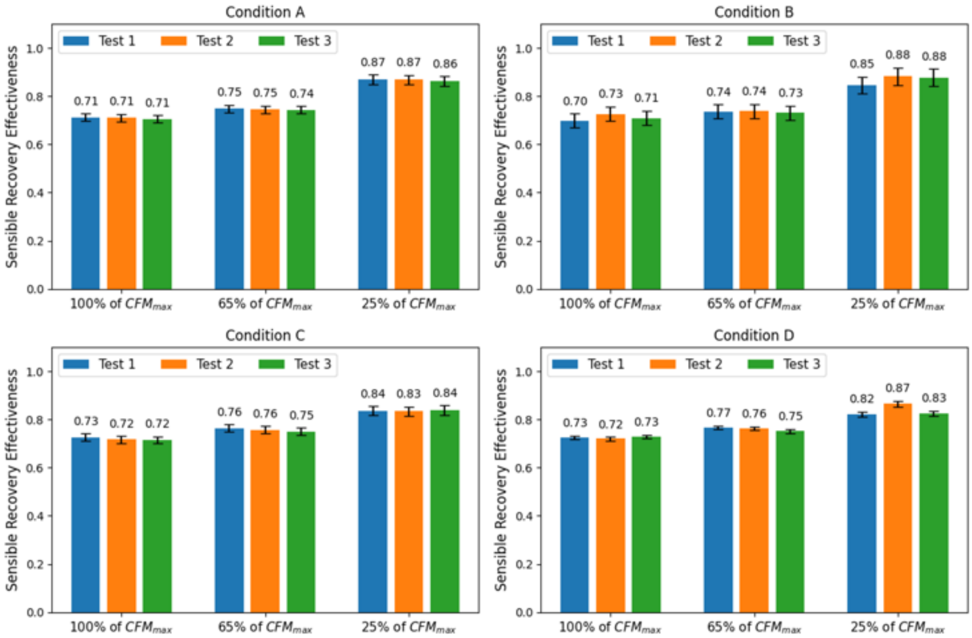

(b)

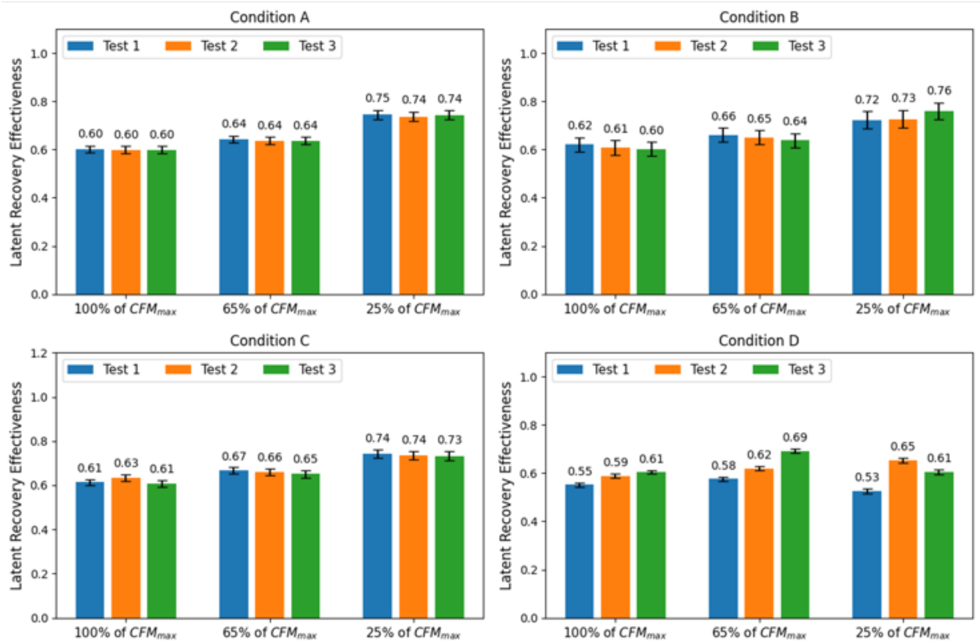

(c)

Figure 3.7: Recovery effectiveness of Unit B: (a) apparent sensible recovery effectiveness (including fan impacts), and (b) sensible recovery effectiveness (at the heat exchange core), and (c) latent recovery effectiveness.

3.2.4 Adjusted sensible recovery efficiency

Figure 3.8 shows the ASRE of the Unit B across the same four conditions and airflow rates tested in triplicate. Conditions C and D again achieved the highest sensible recovery efficiency (0.69–0.84), while Conditions A and B produced lower values (0.50–0.76). Compared to the HRV results, ASRE in Conditions A and B increased more as airflow decreased, whereas Conditions C and D showed less sensitivity to flow rate. Trial-to-trial repeatability remained high across all conditions.

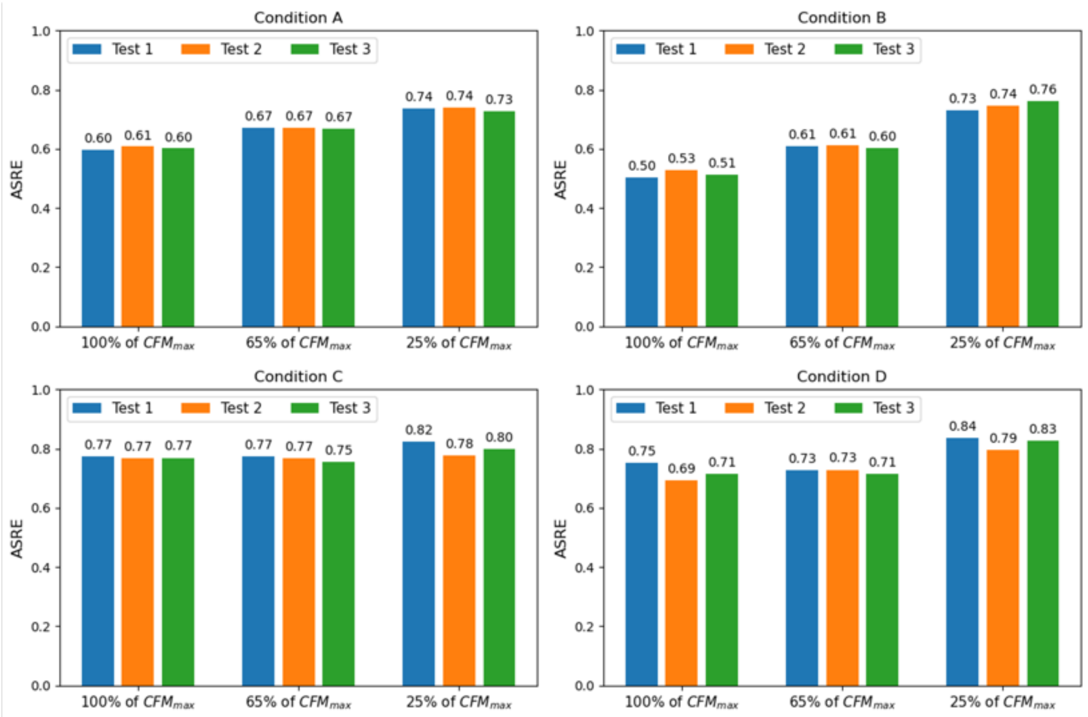

Figure 3.8: Adjusted sensible recovery efficiency (ASRE) for Unit B.

3.3 Wheel-type ERV – Unit C

The unit under test is a wheel-type ERV that primarily consists of a rotary enthalpy wheel serving as the energy recovery core, a dedicated motor for wheel rotation, supply and exhaust fans to provide airflow, and filters installed at each air inlet. The nominal (maximum) airflow rate of Unit C is 2000 CFM, and both the supply and exhaust fans are located downstream of the enthalpy wheel.

3.3.1 Energy balance

Figure 3.9 presents the sensible and latent energy balance of Unit C by comparing the recovered energy calculated on the OA–SA side with that on the RA–EA side. In Figure 3.9 (a), the sensible energy balance shows good agreement across all performance evaluation conditions (A to D), with nearly all data points falling within the $\pm 5\%$ tolerance bands. This indicates that the sensible heat transfer through the heat exchanger core is well balanced between the two air streams and that the sensible energy accounting is consistent across the tested range of operating conditions.

In contrast, Figure 3.9 (b) shows that while Conditions A to C maintain a reasonably balanced latent energy exchange within the $\pm 5\%$ bounds, a noticeable deviation is observed for Condition D. Under Condition D, condensation occurs on the exhaust air (EA) side of the heat exchanger core. The presence of condensation introduces additional latent heat effects associated with phase change and potential liquid water retention or drainage, which are not fully captured by the standard latent energy calculation based solely on humidity ratio differences. As a result, the latent energy balance between the OA–SA and RA–EA streams is disrupted, leading to the observed imbalance for Condition D.

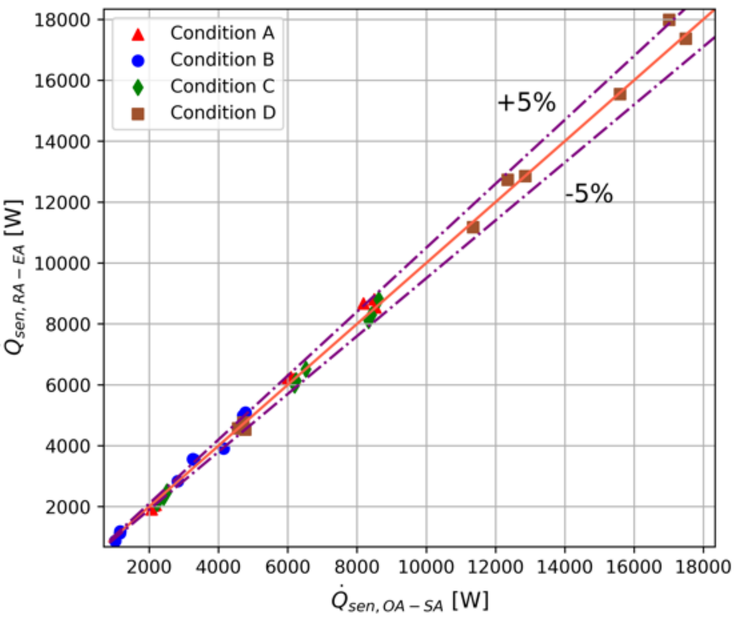

(a)

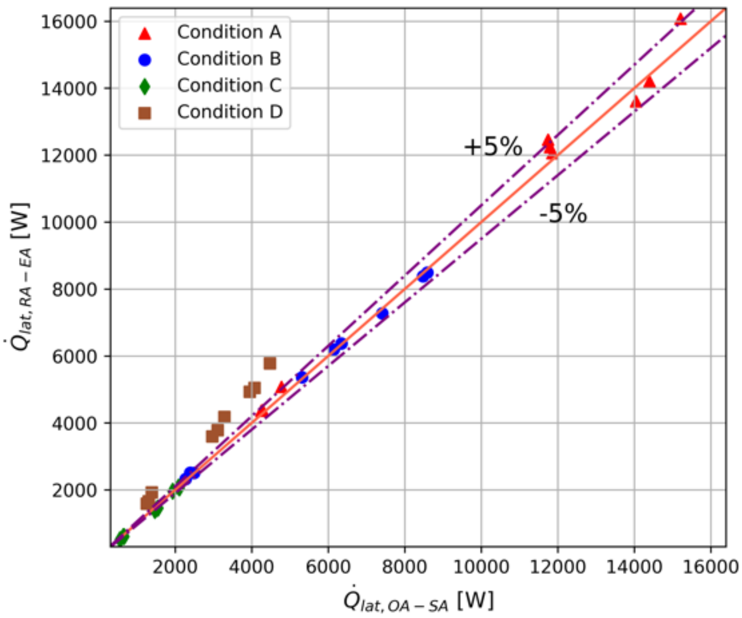

(b)

Figure 3.9: Energy balance of unit C: (a) sensible energy balance, and (b) latent energy balance.

3.3.2 Net and sensible recovered energy

Figure 3.10 summarizes the recovered energy performance of Unit C under Conditions A to D across three airflow levels and repeated tests. Condition A exhibits both strong sensible and latent recovery, reflecting pronounced thermal and moisture driving forces, with a stable net sensible offset and good repeatability. Condition B shows lower recovered energy due to milder boundary conditions, while maintaining consistent airflow dependence and repeatable behavior. Condition C is dominated by sensible recovery with relatively small latent contributions, indicating a weak moisture gradient under this condition. Condition D yields the highest sensible recovered energy, corresponding to the most severe thermal environment, yet preserves consistent airflow scaling and strong repeatability across tests. Overall, the results demonstrate physically consistent trends with airflow and boundary conditions, and confirm that the energy balance framework provides reliable and repeatable characterization of Unit C's performance across a wide range of operating conditions.

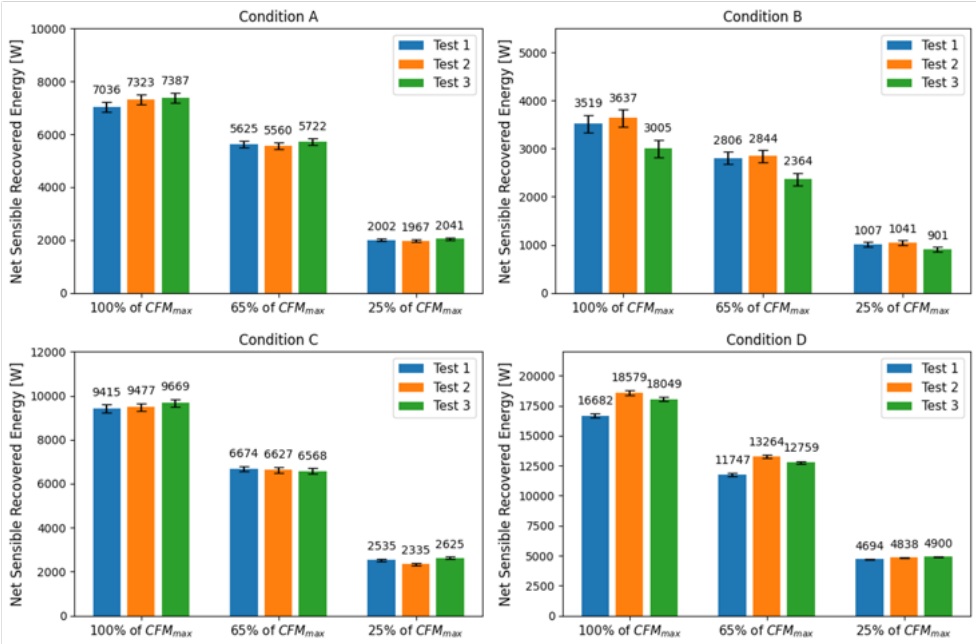
Condition A
Condition B
Condition C
Condition D
Net Sensible Recovered Energy [W]
Test 1
Test 2
Test 3
100% of CFM_{max}
65% of CFM_{max}
25% of CFM_{max}
7036 7323 7387
5625 5560 5722
2002 1967 2041
3519 3637 3005
2806 2844 2364
1007 1041 901
9415 9477 9669
6674 6627 6568
2535 2335 2625
16682 18579 18049
11747 13264 12759
4694 4838 4900

(a)

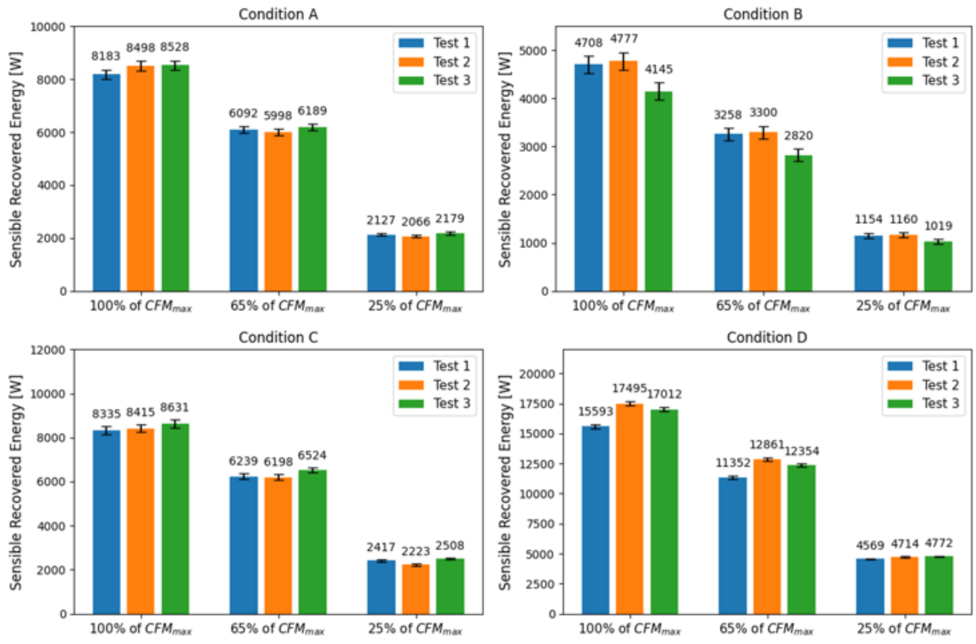
Condition A
Condition B
Condition C
Condition D
Sensible Recovered Energy [W]
Test 1
Test 2
Test 3
100% of CFM_{max}
65% of CFM_{max}
25% of CFM_{max}
8183 8498 8528
6092 5998 6189
2127 2066 2179
4708 4777 4145
3258 3300 2820
1154 1160 1019
8335 8415 8631
6239 6198 6524
2417 2223 2508
15593 17495 17012
11352 12861 12354
4569 4714 4772

(b)

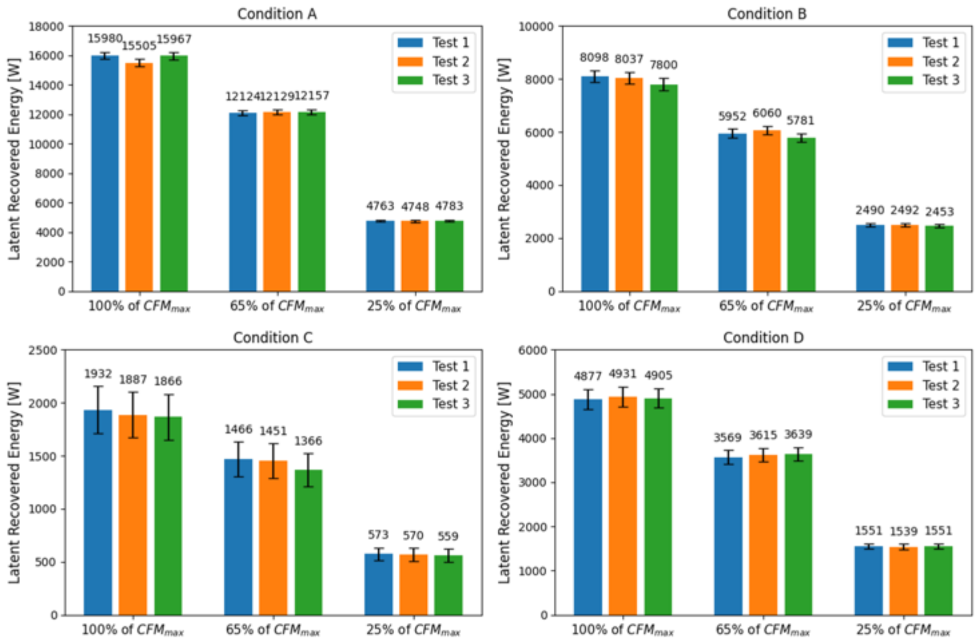

(c)

Figure 3.10: Recovered energy of Unit C: (a) Net recovered energy (including fan impact), (b) recovered energy (at the heat exchanger core), and (c) latent recovered energy.

3.3.3 Apparent and sensible recovery effectiveness

Figure 3.11 summarizes the recovery effectiveness of Unit C under Conditions A to D across three airflow levels and repeated tests.

Under Condition A, sensible and latent recovery effectiveness both increase as airflow is reduced, indicating improved heat- and mass-transfer effectiveness at lower face velocities. Apparent sensible effectiveness follows the same trend, reflecting the combined influence of sensible and latent processes. Repeatability across tests remains strong. For Condition B, effectiveness values are slightly higher than in Condition A at reduced airflow, particularly for latent and apparent sensible effectiveness. This suggests that, despite milder boundary conditions, the core operates efficiently. No abnormal behavior is observed across tests. In Condition C, sensible and apparent sensible effectiveness are relatively high and stable across airflow levels, while latent effectiveness shows a modest increase at reduced flow. This behavior is consistent with a weaker moisture gradient, where latent transfer is limited but still benefits from lower airflow. Condition D exhibits consistently high sensible and apparent sensible effectiveness, with latent effectiveness notably lower than in other conditions. This reflects operation dominated by sensible heat transfer under cold conditions, while moisture transfer plays a reduced role. Despite the severity of the condition, effectiveness trends remain smooth and repeatable.

The effectiveness results demonstrate that Unit C maintains stable and physically consistent performance across a wide range of operating conditions. Effectiveness generally improves at reduced airflow, and the close agreement among repeated tests confirms the robustness of the measured effectiveness metrics.

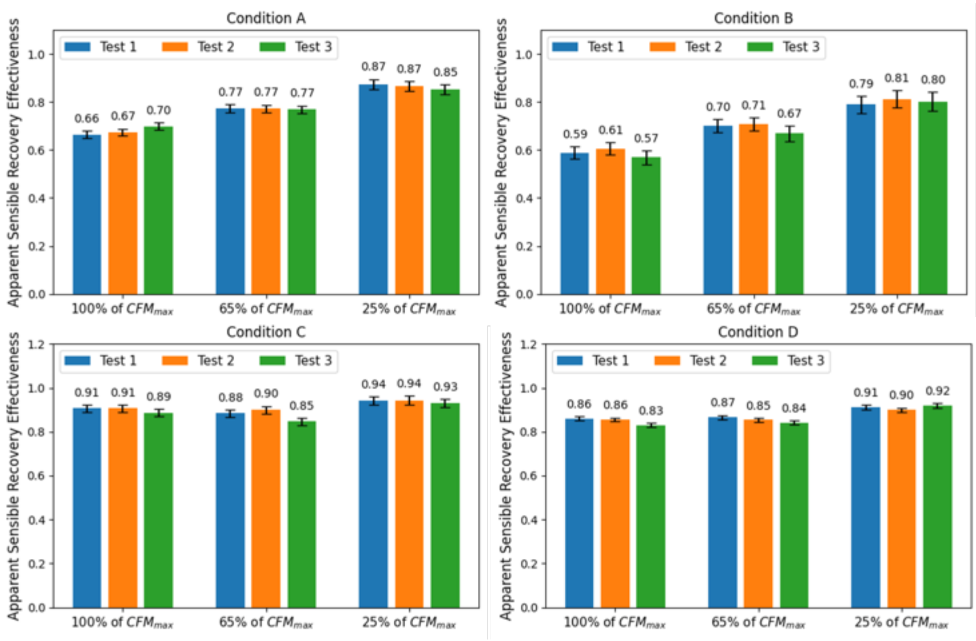

(a)

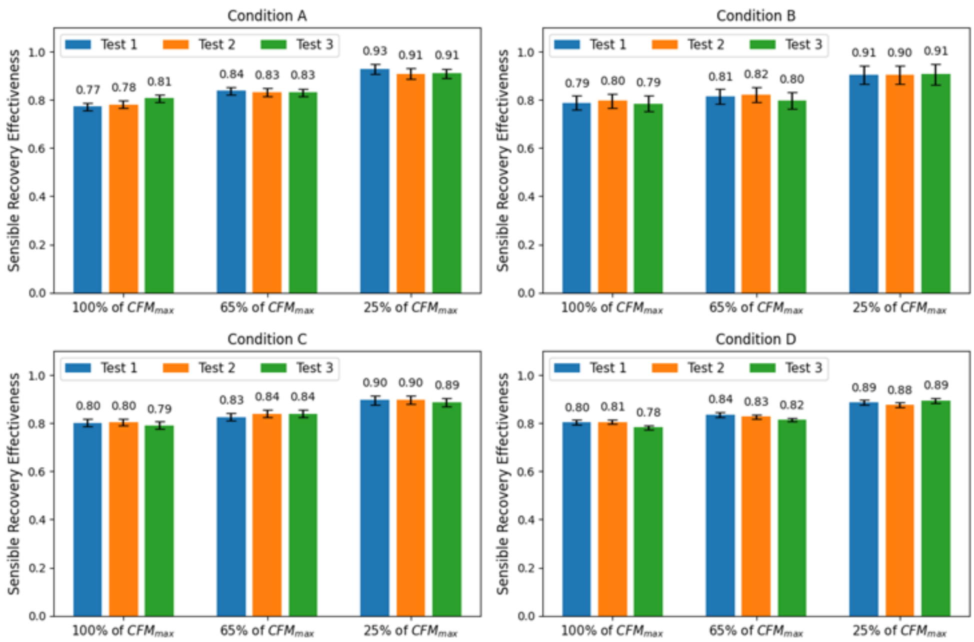

(b)

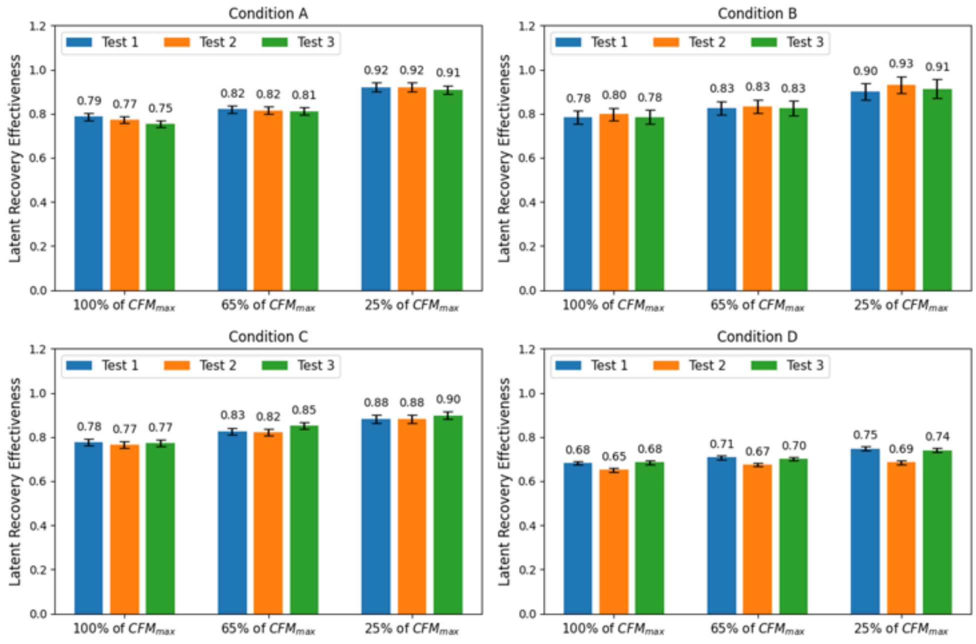

(c)

Figure 3.11: Recovery effectiveness of Unit C: (a) apparent sensible recovery effectiveness (including fan impacts), and (b) sensible recovery effectiveness (at the heat exchange core), and (c) latent recovery effectiveness.

3.3.4 Adjusted sensible recovery efficiency

Figure 3.12 shows the ASRE of the Unit C across four conditions and three airflow rates, each tested in triplicate. Conditions C and D consistently achieved substantially higher sensible recovery efficiency compared to Conditions A and B, with the performance gap being quite pronounced across all flow rates. In Conditions A and B, ASRE improved steadily as airflow decreased from 100% to 25% of maximum airflow, while Conditions C and D exhibited relatively stable ASRE values across the full range of airflow rates. Repeatability across the three trials was good throughout, with only minor inter-test variation observed.

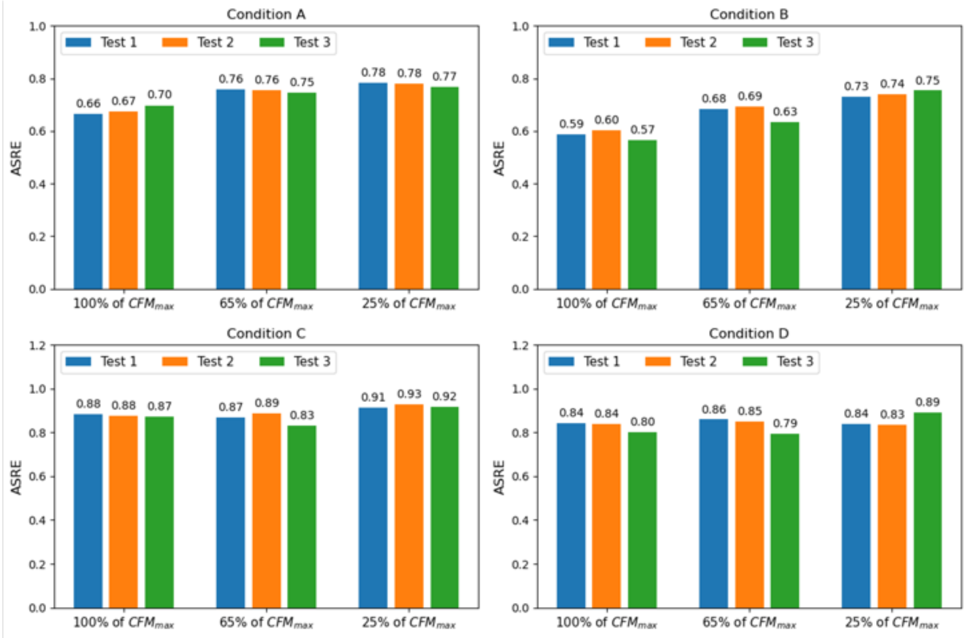

Figure 3.12: Adjusted sensible recovery efficiency (ASRE) of Unit C.

3.4 Plate-type ERV–Unit D

Unit D is a plate-type ERV with a nominal airflow rate of 1000 CFM. The unit employs a fixed-plate enthalpy heat exchanger to enable simultaneous sensible and latent energy recovery between the outdoor and exhaust air streams. Both the supply and exhaust fans are located downstream of the heat exchanger core, resulting in fan heat being added to the air streams after energy recovery. This configuration affects the measured net sensible recovery and is explicitly considered in the performance analysis.

3.4.1 Energy balance

Figure 3.13 evaluates the energy balance across the HX-core by comparing the recovered energy determined from the OA–SA side with that from the RA–EA side, without including any sensible heat addition from the supply or exhaust fans. For the sensible energy balance (Fig. 3.13 (a)), the data points for Conditions A–D closely follow the $1:1$ line and are largely contained within the $\pm 5\%$ bounds, indicating that the measured sensible heat transfer through the core is internally consistent between the two air streams.

For the latent energy balance (Fig. 3.13 (b)), most cases also remain within the $\pm 5\%$ tolerance band, although the scatter is slightly larger than in the sensible case. This behavior is expected because latent transfer is more sensitive to humidity measurement uncertainty and mass-balance errors. Furthermore, a noticeable latent energy imbalance is observed under Condition D, which is attributed to condensation occurring within the HX-core (like the other ERV units).

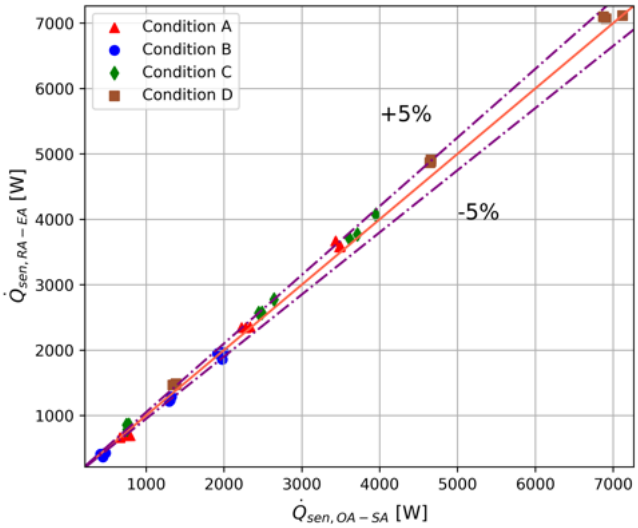

(a)

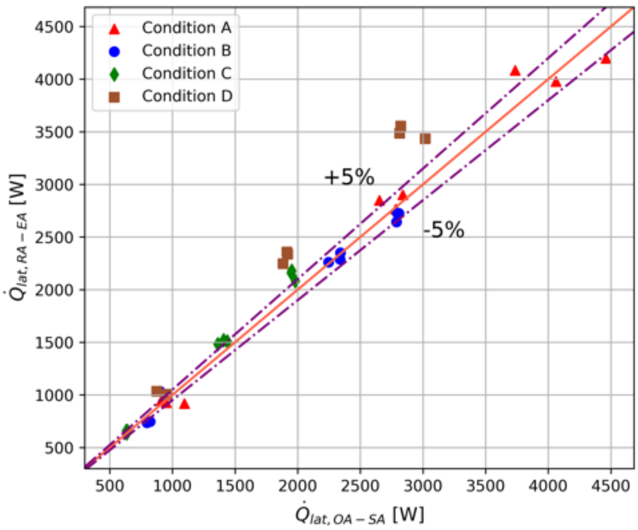

(b)

Figure 3.13: Energy balance of unit D: (a) sensible energy balance, and (b) latent energy balance.

3.4.2 Net and sensible recovered energy

Figure 3.14 presents the recovered energy of Unit D, including net sensible recovered energy, sensible recovered energy attributed solely to the HX-core, and latent recovered energy, evaluated under Conditions A–D at three airflow levels. For all operating conditions, recovered sensible and latent energy decreases with decreasing airflow rate, consistent with reduced air mass flow and the corresponding reduction in heat and moisture transfer through the HX-core.

The net sensible recovered energy (Fig. 3.14(a)) shows good repeatability across repeated tests, indicating stable overall unit performance when both HX-core behavior and downstream effects are included. When isolating HX-core performance (Fig. 3.14(b)), the sensible recovered energy exhibits slightly improved consistency, reflecting the removal of downstream fan heat and confirming internally consistent sensible heat transfer within the core. The latent recovered energy (Fig. 3.14(c)) follows similar airflow-dependent trends but shows greater test-to-test variation than the sensible components, consistent with the higher sensitivity of humidity-based measurements.

The relative differences among operating conditions and the observed trends in recovered energy are consistent, supporting the robustness of the recovered energy evaluation for Unit D.

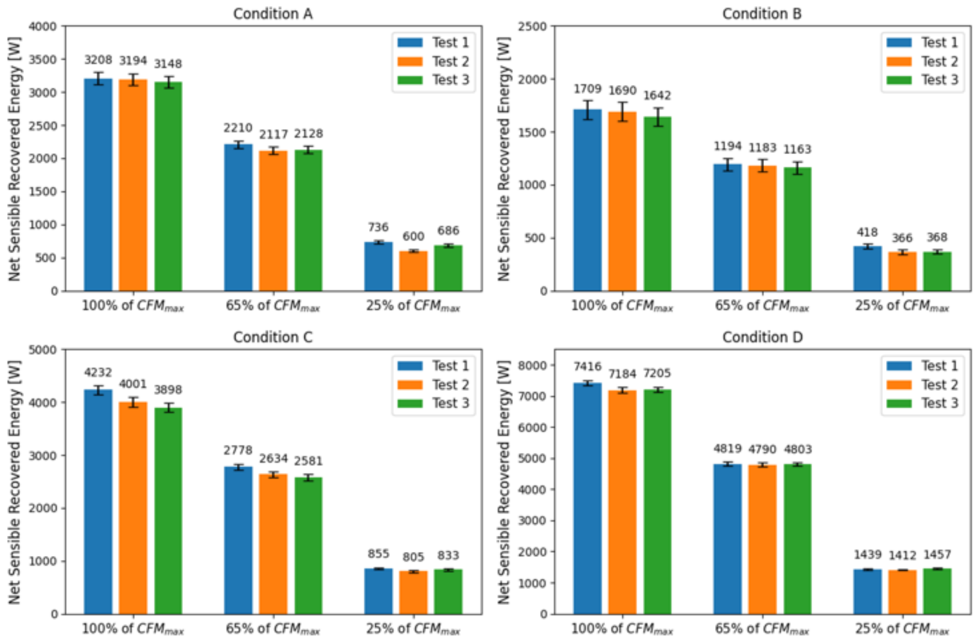

(a)

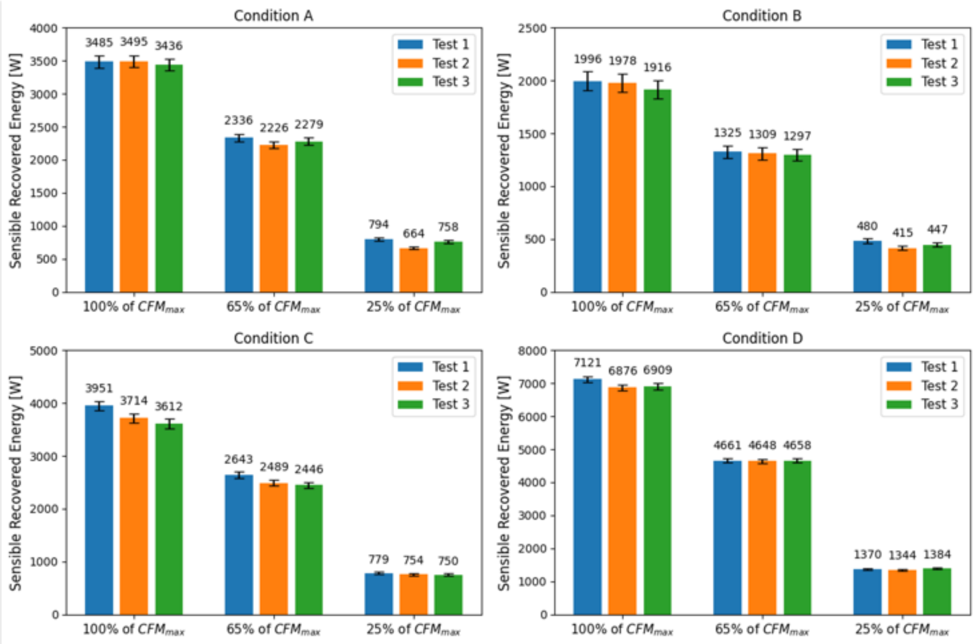

(b)

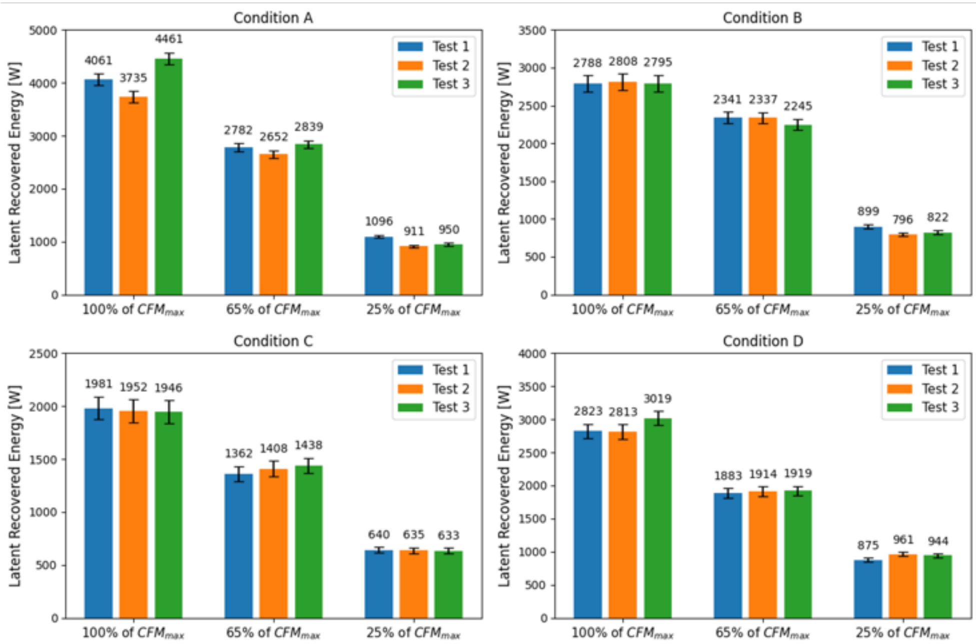

(c)

Figure 3.14: Recovered energy of Unit D: (a) Net recovered energy (including fan impact), (b) recovered energy (at the heat exchanger core), and (c) latent recovered energy.

3.4.3 Apparent and sensible recovery effectiveness

Figure 3.15 presents the recovery effectiveness results of Unit D, including (a) sensible recovery effectiveness, (b) latent recovery effectiveness, and (c) apparent sensible recovery effectiveness, evaluated under Conditions A to D at three airflow levels. Across all operating conditions, both sensible and latent recovery effectiveness generally increase as airflow is reduced from 100% to 25% of CFM_{max}.

For the sensible recovery effectiveness shown in Fig. 3.15(a), the results demonstrate good repeatability among the three tests for each condition and airflow level. Conditions C and D exhibit slightly higher sensible effectiveness than Conditions A and B, reflecting larger temperature driving forces under colder outdoor air conditions. The increase in sensible effectiveness at reduced airflow is consistent across all conditions, indicating stable core thermal performance.

The latent recovery effectiveness shown in Fig. 3.15 (b) exhibits similar airflow-dependent trends, with effectiveness increasing as the airflow rate is reduced for all operating conditions. Conditions A and B demonstrate relatively high latent effectiveness due to large humidity ratio differences between the air streams, whereas Condition C shows more moderate latent effectiveness. Under Condition D, latent effectiveness is lower at the highest airflow rate but increases substantially at reduced airflow, which is attributed to the onset of condensation within the heat exchanger core.

Figure 3.15 (c) compares the apparent sensible recovery effectiveness with the sensible recovery effectiveness. In cooling mode, the apparent sensible effectiveness is consistently lower than the corresponding sensible effectiveness, whereas in heating mode it is higher. This behavior arises because the apparent sensible effectiveness is calculated using temperatures measured across the entire unit and therefore includes the influence of downstream fan heat and auxiliary components. The discrepancy between sensible and apparent sensible effectiveness becomes more pronounced at lower airflow rates, where fan heat constitutes a larger fraction of the total sensible energy change in the supply air stream.

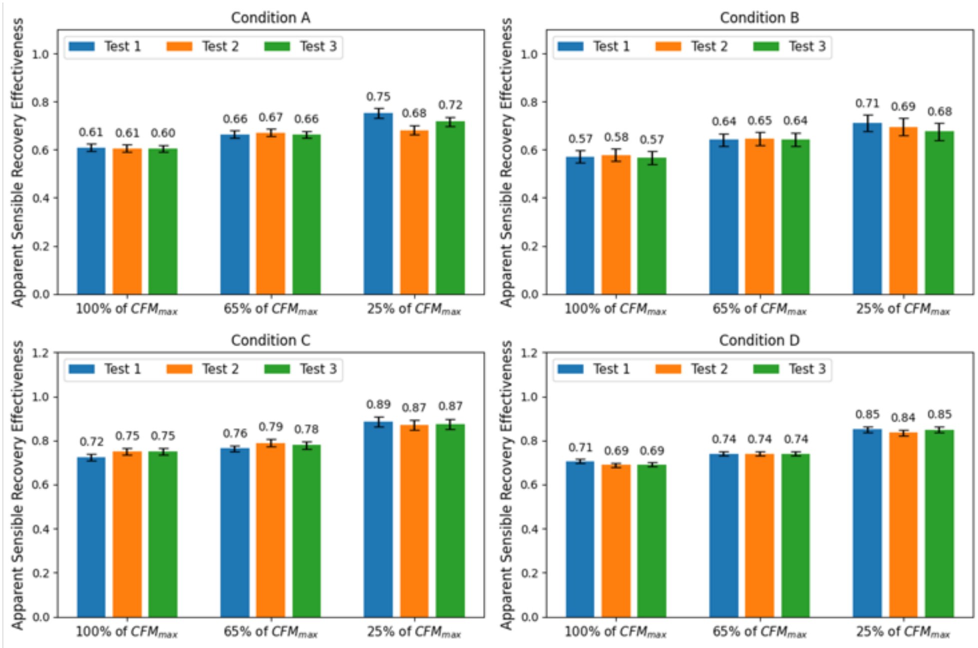
Condition A
Condition B
Condition C
Condition D
Test 1
Test 2
Test 3
Apparent Sensible Recovery Effectiveness
100% of CFM_{max}
65% of CFM_{max}
25% of CFM_{max}
0.61 0.61 0.60
0.66 0.67 0.66
0.75 0.68 0.72
0.57 0.58 0.57
0.64 0.65 0.64
0.71 0.69 0.68
0.72 0.75 0.75
0.76 0.79 0.78
0.89 0.87 0.87
0.71 0.69 0.69
0.74 0.74 0.74
0.85 0.84 0.85

(a)

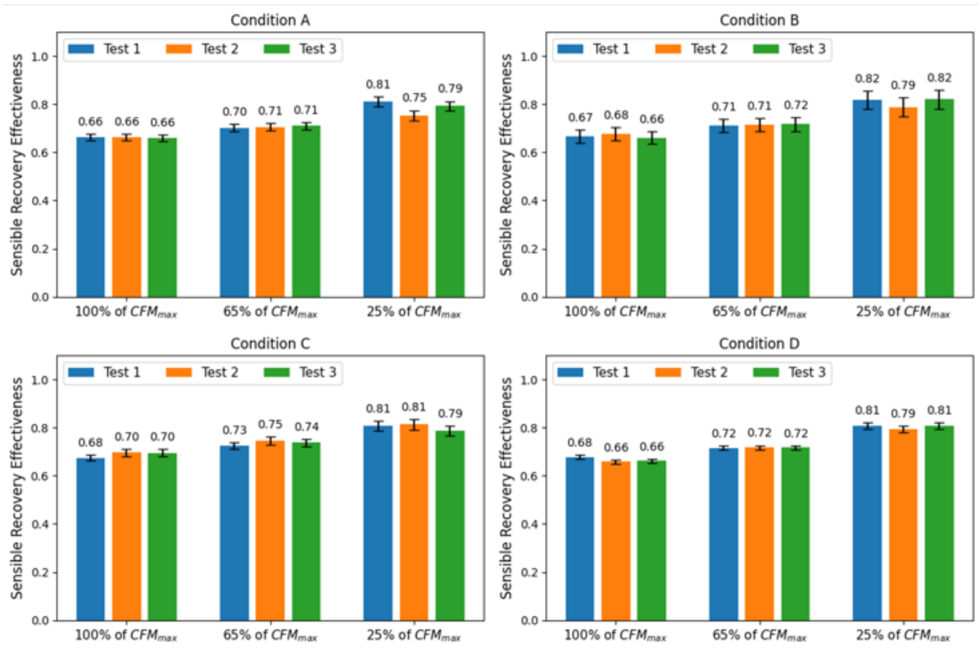
Condition A
Condition B
Condition C
Condition D
Test 1
Test 2
Test 3
Sensible Recovery Effectiveness
100% of CFM_{max}
65% of CFM_{max}
25% of CFM_{max}
0.66 0.66 0.66
0.70 0.71 0.71
0.81 0.75 0.79
0.67 0.68 0.66
0.71 0.71 0.72
0.82 0.79 0.82
0.68 0.70 0.70
0.73 0.75 0.74
0.81 0.81 0.79
0.68 0.66 0.66
0.72 0.72 0.72
0.81 0.79 0.81

(b)

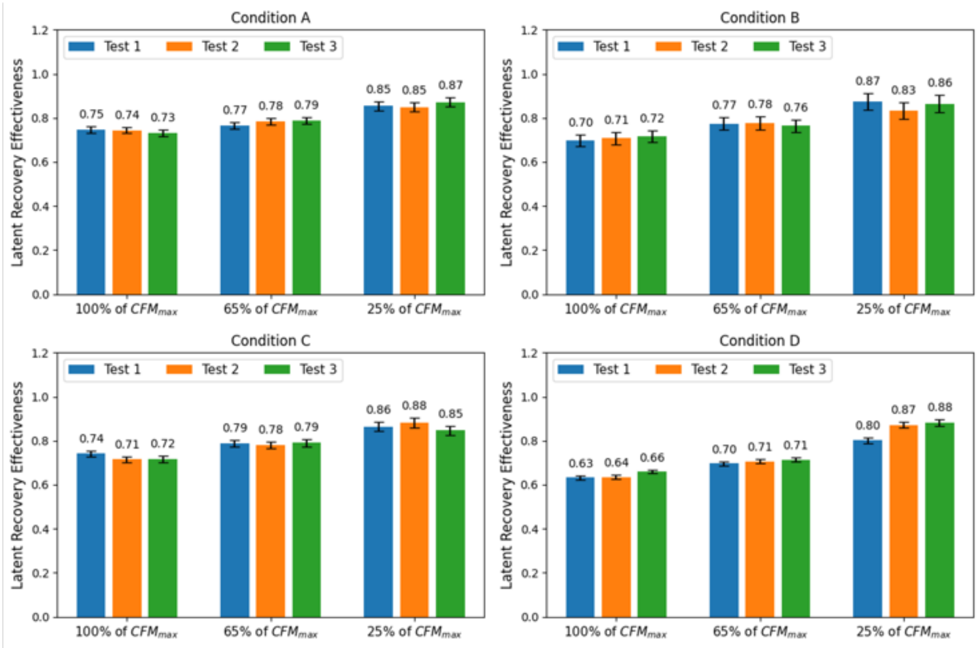

(c)

Figure 3.15: Recovery effectiveness of Unit D: (a) apparent sensible recovery effectiveness (including fan impacts), and (b) sensible recovery effectiveness (at the heat exchange core), and (c) latent recovery effectiveness.

3.4.4 Adjusted sensible recovery efficiency

Figure 3.16 presents the ASRE results for the Unit D under four test conditions at varying airflow rates. Across all conditions, sensible recovery efficiency was higher in Conditions C and D than in A and B. While most conditions showed a gradual improvement in ASRE at lower airflow rates, Condition D stood out as an exception, remaining nearly constant across all three flow rates. Condition A at 25% of maximum airflow exhibited slightly more deviation between trials compared to the rest of the dataset, though overall test repeatability remained acceptable.

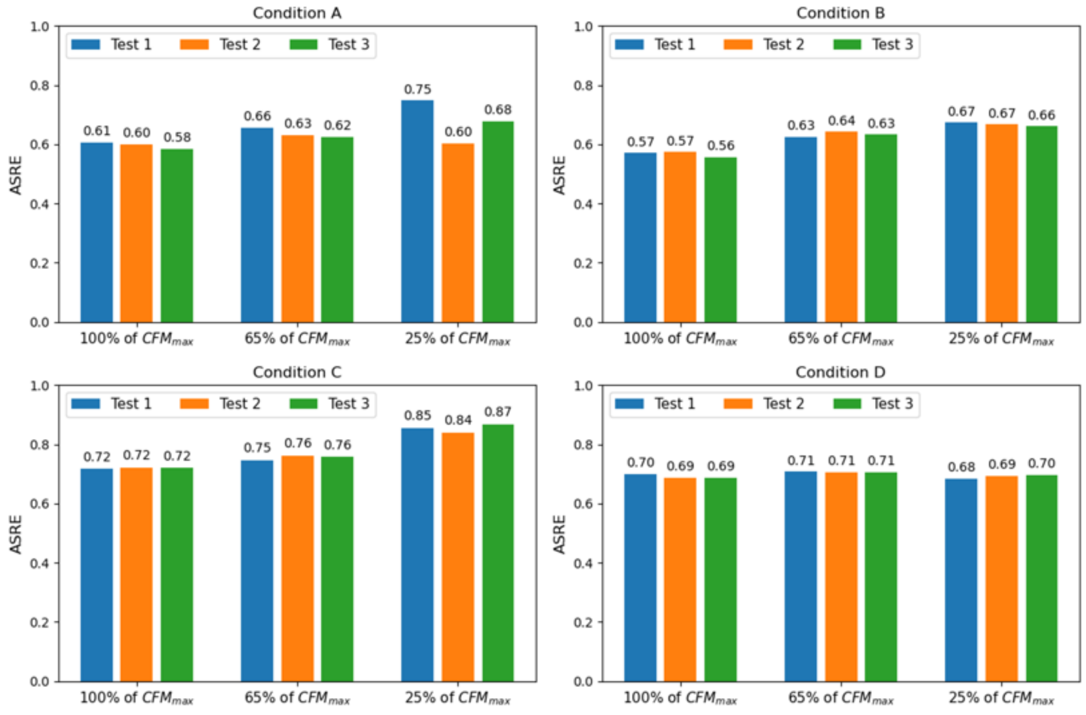

Figure 3.16: Adjusted sensible recovery efficiency (ASRE) of Unit D.

3.5 Low-temperature test results

As summarized in Table 1, test conditions E and F are defined in CSA SPE-18 as optional low-temperature operating conditions. Condition E is intended to support the identification or estimation of parameters relevant to cold-weather frost control, while condition F is specified both to support assessment of frost-control behavior, and also to evaluate long-term cold-weather performance under more severe outdoor conditions.

In the present study, test E was conducted on Units B, C, and D in accordance with the requirements of SPE-18 (although it is specified as an optional "as needed" test in the standard). Since Units A and B share the same defrost behavior, one of them was tested. However, test condition F could not be implemented due to limitations of the psychrometric chamber at Purdue University, which was unable to achieve the required minimum outdoor temperature specified by the standard. To address this constraint, an alternative low-temperature condition, denoted as E', was defined and only to enhance the assessment of frost-control behavior. Under condition E', the outdoor air temperature was set to the lowest value attainable by the existing Purdue test facilities, while maintaining all other test parameters consistent with the intent of the standard. This approach allowed partial assessment of low-temperature performance within the practical limits of the available laboratory infrastructure.

For each test unit, a single test sequence was conducted at each low-temperature condition. Within each sequence, the unit was evaluated at three distinct airflow rates to characterize airflow-dependent performance behavior under cold-weather operation.

3.5.1 Unit B Tested

The frost control logic implemented in Unit A and Unit B is identical and relies on an electric preheater installed upstream of the energy exchanger (EX) core and downstream of the preheater on the outdoor air side. The control strategy is designed to prevent frost formation within the core under low-temperature operating conditions and can be summarized as follows:

- When the exhaust air temperature leaving the HX-core (in the exhaust air stream) falls below a predefined threshold, the electric preheater is activated to raise the temperature of outdoor air entering the HX-core until the exhaust air temperature reaches the threshold. The average power is thus modulated between 0 and full power by the on-off ratio of the heater using the feedback.
- If the preheater is operating at full load and the exhaust air temperature entering the HX-core remains below the target temperature, the unit transitions to a protection mode that progressively bypasses outdoor air, subject to any programmed minimum supply air temperature, and ultimately shuts down the fan(s) if that limit cannot be maintained.

Based on this control logic, the system behavior observed during the low-temperature tests can be clearly interpreted using Figure 3.17. Under condition E, the preheater is activated only when the unit is tested at 25% of the nominal airflow (250 CFM) rate when the exhaust air temperature falls below the predefined threshold of approximately 5°C (41°F), indicating the initiation of frost-protection operation. Following preheating, the exhaust air temperature increases sufficiently, and the preheater is subsequently deactivated. As a result, the test data show that the preheater cycles on and off during this operating condition.

The lab test results for this unit are anomalous and did not follow the expected control sequence when the lower temperature test E' was conducted. Following the lab test, the same unit was tested in the field, where its behavior was further examined. The anomaly is attributed to an inadvertent misconfiguration during testing, where the supply air low-temperature limit setpoint was left at the unit default of 15°C (59°F) rather than the intended 13°C (55°F), likely triggering premature shutdown. Previous lab testing conducted by Purdue on the same unit produced results consistent with the manufacturer's described frost control sequence, and those results are used in the subsequent SCOP calculations.

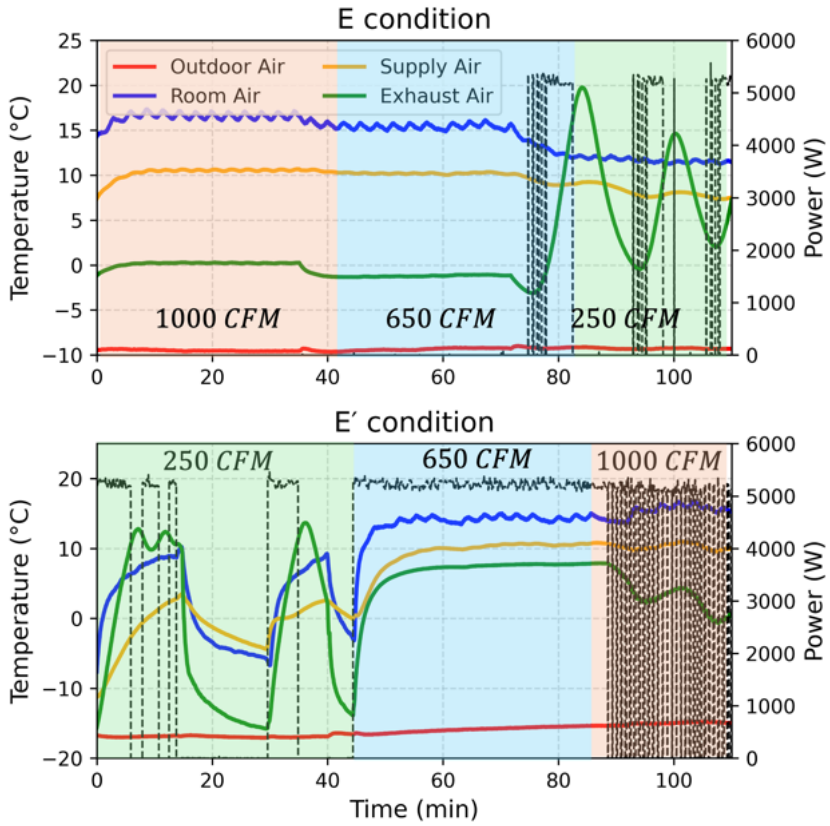

Figure 3.17: Low temperature tests results for Unit A

3.5.2 Unit C

Based on the low-temperature test results, the frost control strategy of Unit C and its corresponding system response can be interpreted in conjunction with the measured temperature trends shown in Figure 3.18.

Unit C employs a pressure-based frost detection and mitigation strategy that monitors the pressure drop across the enthalpy wheel. Under normal, frost-free operation, an initial baseline pressure drop is established. As frost accumulates on the wheel surface under low-temperature conditions, the associated increase in flow resistance leads to a rise in the measured pressure drop across the wheel. When this pressure drop exceeds the baseline value by a predefined threshold of 0.2 in H_2O, the frost control logic is designed to activate. In response, the controller reduces the wheel rotational speed to its minimum setting in order to increase the wheel's exposure to the warmer exhaust air stream and decrease the rate of heat transfer away from the exhaust air, thus increasing exhaust air temperature and promoting passive frost removal.

However, this pressure-based frost mitigation behavior was not clearly observed during the low-temperature tests. As shown in Figure 3.18, when the airflow rate was sequentially reduced from 1500 CFM to 1000 CFM and then to 500 CFM under Condition E, no corresponding activation of the wheel speed reduction mode was detected, and the measured pressure drop across the enthalpy wheel remained largely unchanged. Under the more severe E' condition at 500 CFM, the frost protection logic escalated directly to a full protective shutdown, during which both the fans and the enthalpy wheel were stopped to prevent further icing and potential mechanical damage at approximately 20 minutes and 40 minutes in Figure 3.18. Notably, this shutdown occurred despite the absence of a significant increase in the observed pressure drop across the wheel.

To verify and confirm this behavior, the fans and wheel were manually restarted following the initial shutdown event. Upon restart, the unit briefly resumed operation; however, as the exhaust air temperature continued to decrease and dropped below approximately -10°C, the frost protection logic was re-engaged, again resulting in a complete shutdown of both the supply fan and the wheel. This repeated response confirms the repeatability and robustness of the protective shutdown mechanism under extreme cold-weather conditions, while also suggesting that, at very low temperatures and airflow rates, the frost control strategy, like units A and B, employs one or more additional stage(s) of frost protection beyond the first-stage strategy.

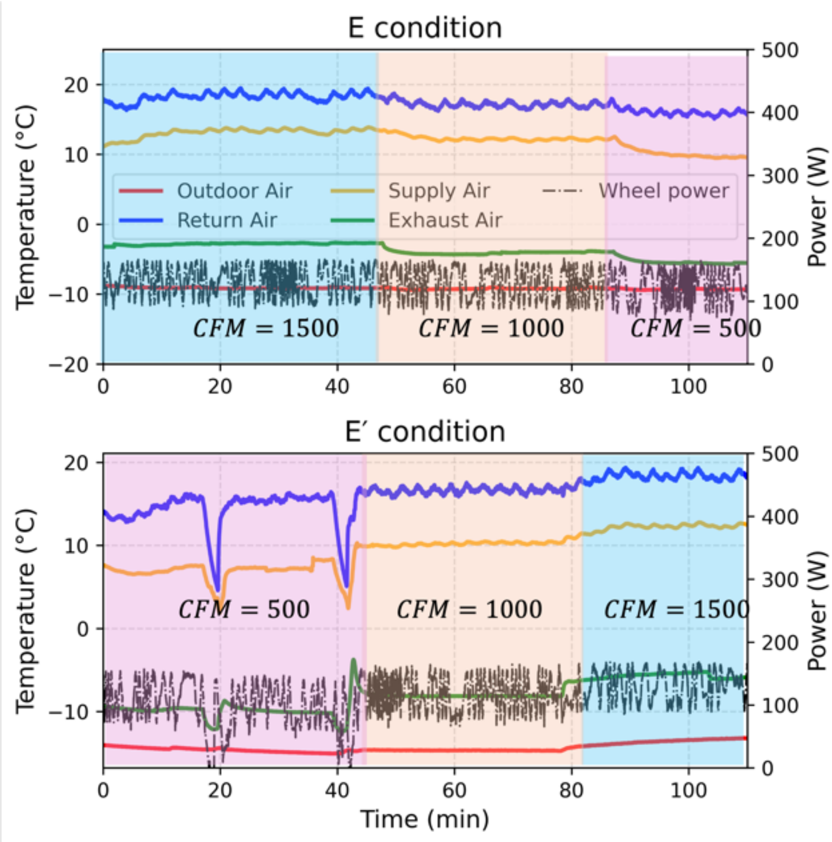

Figure 3.18: Low temperature tests results for Unit C

3.5.3 Unit D

Unit D employs a frost control strategy that periodically suspends the supply air (SA) flow while maintaining the room-exhaust airflow, allowing relatively warmer indoor air to pass through the heat exchanger core and remove the frost in the HX-core.

Figure 3.19 illustrates the measured airflow response of Unit D during the low-temperature tests under conditions E and E'. As shown in both operating conditions, the supply airflow is intentionally reduced to near zero for approximately 1 minute at regular intervals of about 6 to 7 minutes. This cyclic interruption-and-recovery pattern is consistently observed across all tested airflow setpoints (1000 CFM, 650 CFM, and 250 CFM), indicating that the frost control logic is time-based rather than demand-based. The results confirm that Unit D relies on periodic supply-air shutdown as its primary frost mitigation mechanism.

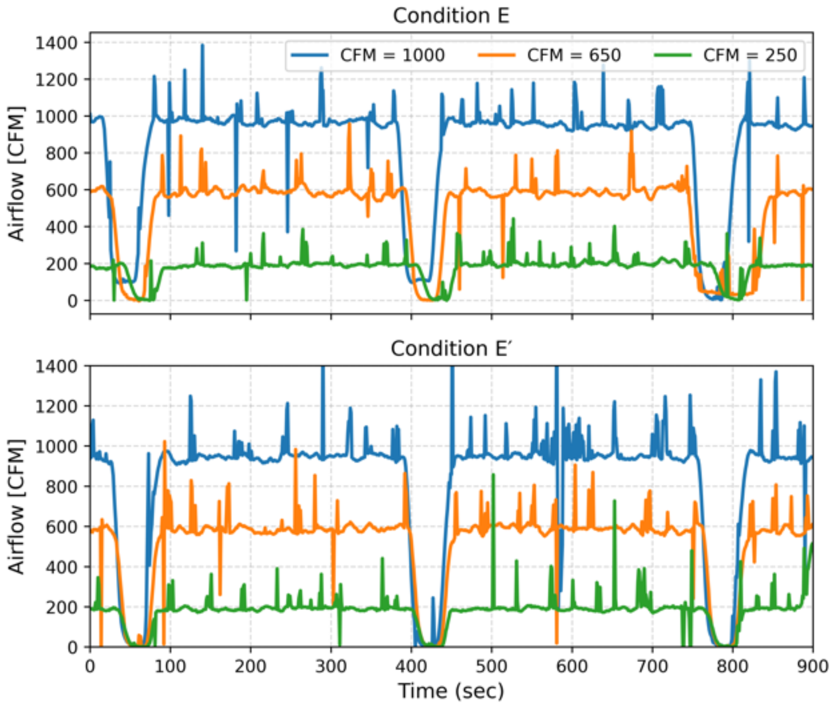

Figure 3.19: Low temperature tests results for Unit D

This metric is defined as the frost-control duty cycle in this study, representing the fraction of time within one hour that the supply fan is disabled during a complete frost-control cycle, as shown in Eq. 3.1. Based on this duty cycle, the effective recovered energy rate under frost-control operation is determined using Eq. 3.2.

$$\text{DutyCycle}_{\text{frost}} = \frac{time_{\text{off}}}{time_{\text{total}}} = \frac{\sum_{i=1}^{N} time_{\text{off},i}}{time_{\text{total}}} \tag{3.1}$$

$$\dot{Q}_{\text{rec,eff}} = (1 - \text{DC}_{\text{frost}})\, \dot{Q}_{\text{rec,on}} \tag{3.2}$$

4 Model Development for SCOP Calculations

The energy performance model is used to apply the test results to other operating conditions that are required for seasonal calculation. The energy performance model is developed by first modeling the main components and subsequently integrating them into a complete system representation. In accordance with the typical ERV configuration, the primary components influencing overall performance are the HX-core, fans, other anxiliary energy loads, and the frost control strategy.

4.1 Fan curves

The fan model is essential for determining both the heat transferred to the airstream at a given airflow rate and the corresponding power consumption. The fan motor power is represented using a quadratic regression as shown in Eq. 4.1, developed by curve-fitting the measured fan power imparted to the airstream at three discrete airflow operating points.

$$\dot{q}_{in,SF/EF} = b_0 + b_1 \cdot \dot{Q}_{SA/EA} + b_2 \cdot \dot{Q}^2_{SA/EA} \tag{4.1}$$

where:
$b_0, b_1, b_2 =$ constant, first, and second order regression coefficients as determined;
$\dot{Q}_{SA/EA} =$ airflow of the airstream (supply or exhaust).

Figure 4.1 shows the measured fan power data and the fitted quadratic fan curves for the supply-air (SA) and exhaust-air (EA) fans of Units A, B, C and D. As described by Eq. 4.1, the fan model is used to determine (i) the electrical power consumption at a given airflow rate and (ii) the corresponding sensible heat added to the airstream by the fan motor. The regression coefficients (b_0, b_1, b_2) were obtained by curve-fitting fan power measured at three discrete airflow operating points and then applied across the operating range shown in each panel.

Across all units, fan power increases nonlinearly with airflow, and the quadratic model provides good agreement with the measured data over the full operating range. Units A and B exhibit similar fan power characteristics, due to the same airflow ranges and fan sizing. Unit C operates over a substantially higher airflow range and correspondingly shows higher fan power consumption, while Unit D exhibits lower absolute fan power at higher air flows and higher power at 25% of rated airflow. In all cases, the SA fan power is consistently higher than the EA fan power at a given airflow, indicating higher filter resistance on the supply side of the unit.

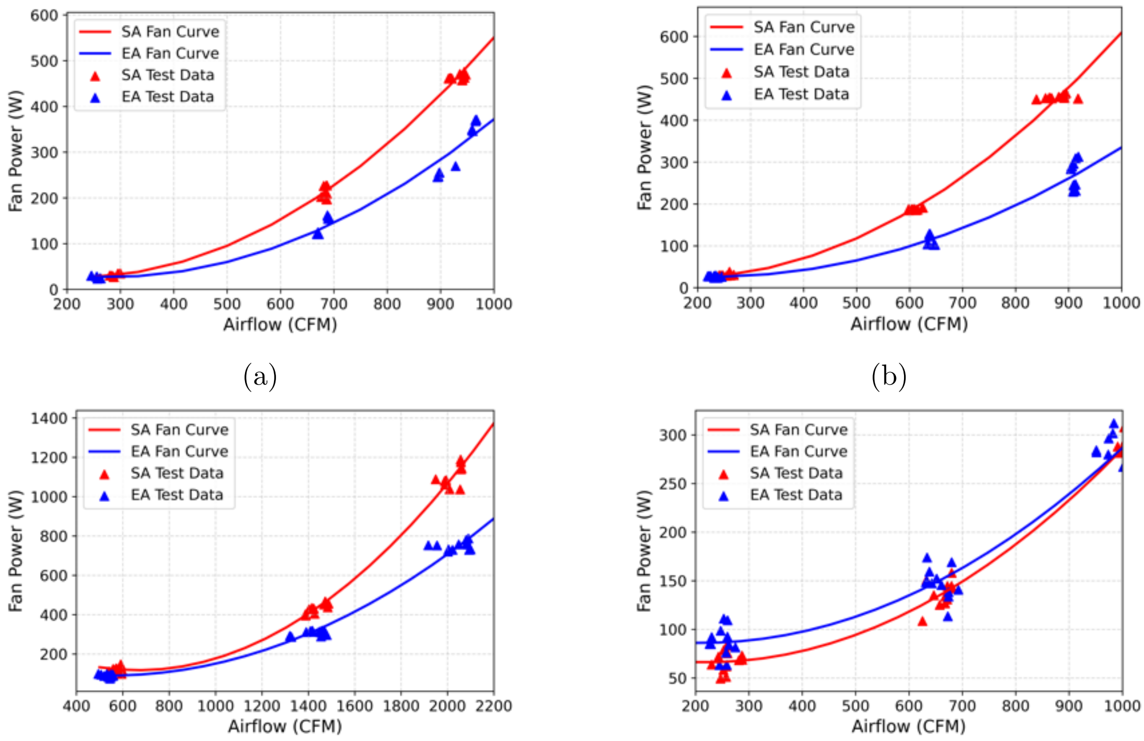

(a) (b) (c) (d)

Figure 4.1: Fan curves for all test units: (a)Unit A, (b) Unit B, (c) Unit C, and (d) Unit D.

Unit	Fan Type	b_0	b_1	b_2
Unit A	Supply Fan	65.822	-0.367	0.000852
	Exhaust Fan	76.684	-0.362	0.000658
Unit B	Supply Fan	45.045	-0.273	0.000837
	Exhaust Fan	52.061	-0.231	0.000514
Unit C	Supply Fan	356.078	-0.714	0.000534
	Exhaust Fan	177.254	-0.317	0.000290
Unit D	Supply Fan	83.974	-0.160	0.000362
	Exhaust Fan	100.512	-0.136	0.000322

Table 2: Fan curve regression coefficients for each unit

4.2 Heat exchanger effectiveness

$$\varepsilon_{s/l} = \frac{1 - e^{-Ntu_{s/l}(1-C_{s/l})}}{1 - C_{s/l}e^{-Ntu_{s/l}(1-C_{s/l})}} \tag{4.2}$$

$$\varepsilon_{s/l} = 1 - e^{C_{s/l} \cdot Ntu_{s/l}^{0.22} \cdot e^{-C_{s/l} \cdot Ntu_{s/l}^{0.78}} - 1} \tag{4.3}$$

where $\varepsilon_{s/l}$ is the core effectiveness that can be calculated at various operating conditions, with subscript s is *sensible* or l is *latent*. $\varepsilon_{s/l}$ in Eq. 4.2 applies to counter-flow HX-core configuration, while Eq. 4.3 applies to cross-flow configurations. The appropriate equation should be selected according to the HX-core configuration used. $\varepsilon_{s/l}$ is dimensionless, and generally expressed as a percent decimal fraction multiplied by 100. $Ntu_{s/l}$ is a defined number of sensible (s) or latent (l) heat transfer units, as follows:

$$Ntu_s = \frac{UA_s}{m_{min}c_p}; \qquad Ntu_l = \frac{UA_l}{m_{min}} \tag{4.4}$$

where UA_s is a single value representing an imaginary heat transfer rate times a surface area. UA varies with airflow;

$$UA_s = a_0 + a_1\dot{Q} + a_2\dot{Q}^2; \qquad UA_l = b_0 + b_1\dot{Q} + b_2\dot{Q}^2 \tag{4.5}$$

where Q is supply air flow ($\dot{Q}_{SA}$), $m^3/s(ft^3/min)$; a_0, a_1, a_3 and b_0, b_1, b_2 are constant, first-order and second-order regression coefficients.
$C_{s/l}$ is unitless coefficient as defined for sensible (s) and latent (l), as follows:

$$C_s = \frac{min(\dot{m}_{SA}c_p, \dot{m}_{EA}c_p)}{max(\dot{m}_{SA}c_p, \dot{m}_{EA}c_p)}; \qquad C_l = \frac{min(\dot{m}_{SA}, \dot{m}_{EA})}{max(\dot{m}_{SA}, \dot{m}_{EA})} \tag{4.6}$$

If $\dot{m}_{min} = \dot{m}_{max}$, then $C_{s/l}$ should be set to 0.999 because $C_{s/l}$ cannot be equal to 1.

To assess the model's sensitivity to test-to-test variability, a complete set of training datasets was constructed by selecting one test from each operating condition. For the sensible-effectiveness analysis of the HX-core, one test was chosen from Conditions A, B, C, and D for each curve-fitting instance. Rather than employing random sampling, all possible combinations were explicitly enumerated to ensure full coverage of the test space. Because each condition contains three independent tests, this yields $3^4 = 81$ unique combinations, resulting in 81 independently trained curves. This exhaustive approach ensures that every feasible assembly of experimental tests is represented, thereby enabling a comprehensive evaluation of repeatability and model robustness. For the latent-effectiveness model training, Condition D was excluded because condensation occurred within the core under that condition, and the latent-effectiveness model described above is not applicable. Consequently, selecting one test from Conditions A, B, and C produces $3^3 = 27$ unique combinations, resulting in 27 trained latent-effectiveness curves.

All fitted curves were evaluated on an airflow grid from maximum to minimum, denoted as $\{x_j\}_{j=1}^{N}$ with $N = 20$. The mean curve and the standard deviation of the fitted curves at each grid point were computed as

$$\mu(x_j) = \frac{1}{M}\sum_{i=1}^{M} y_i(x_j) \tag{4.7}$$

$$\sigma(x_j) = \sqrt{\frac{1}{M-1}\sum_{i=1}^{M}\left[y_i(x_j) - \mu(x_j)\right]^2} \tag{4.8}$$

where $M = 81$ is the total number of fitted curves and $y_i(x_j)$ is the value of the ith fitted curve evaluated at grid point x_j.

4.2.1 Unit A

Figure 4.2 illustrates the sensible-effectiveness curve together with its repeatability band derived from all 81 possible curve-fit combinations. The mean fitted curve (red line) shows a smooth and monotonic decrease in sensible effectiveness as the supply airflow increases from approximately 250 to 1000 CFM, consistent with typical ERV performance characteristics. A narrow 95% confidence band is observed across the entire airflow range, indicating strong repeatability of the fitted curve despite variability in the raw measurements. The confidence interval is slightly wider at low airflows, where measurement sensitivity is higher, but it remains within a small absolute range, demonstrating that the curve shape is not significantly affected by the choice of repeated measurement.

The coefficient of variation (CV), shown on the secondary axis, remains below 0.8% over the entire operating range. The CV curve peaks near $500 CFM$ but does not exceed 1%, confirming that the relative variation of the fitted curves is very low. This indicates that the curve-fitting procedure is highly stable and that measurement repeatability has minimal impact on the predicted effectiveness.

The plotted raw data for Conditions A–D also align well with the mean curve trend, further supporting the consistency of the underlying measurements. Overall, the repeatability analysis demonstrates that both the fitted model and the measured data exhibit excellent consistency, and the resulting performance curve can be considered robust for subsequent analysis and reporting.

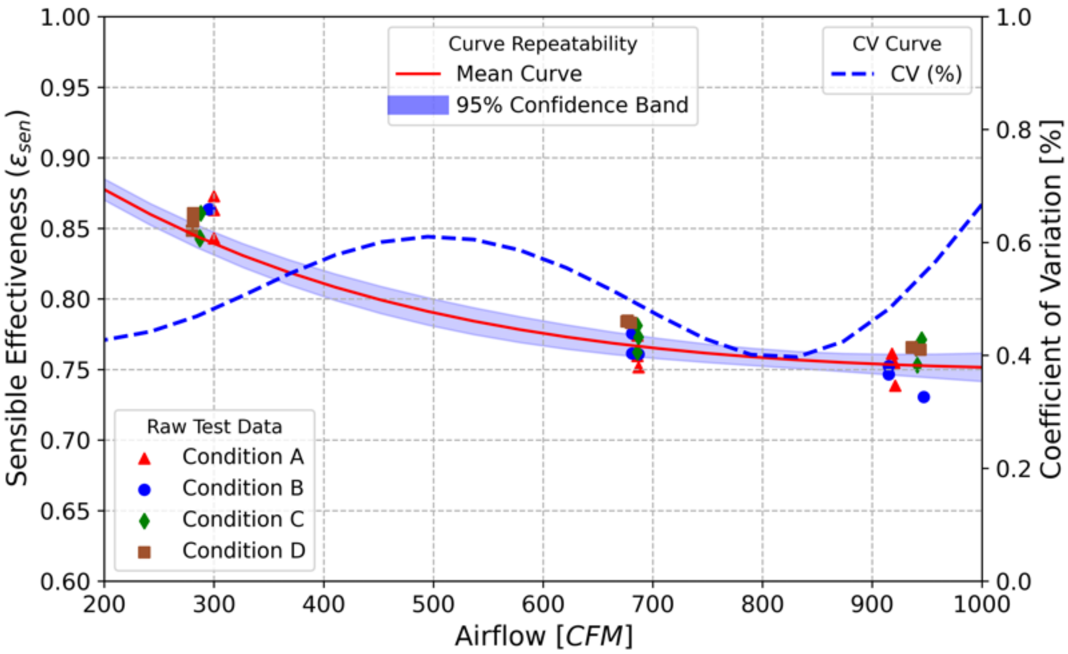

Figure 4.2: Heat exchanger model training results of Unit A.

4.2.2 Unit B

Figure 4.3 presents the heat exchanger model training results for Unit B, illustrating both sensible and latent effectiveness as functions of airflow together with repeatability metrics. In both cases, effectiveness decreases smoothly with increasing airflow, reflecting reduced residence time and heat–mass transfer opportunity at higher flow rates. The fitted mean curves capture this trend well, with the raw test data from all operating conditions clustering closely around the model predictions.

The shaded 95% confidence bands remain narrow across most of the operating range, indicating limited test-to-test variability and a well-constrained model fit. The coefficient of variation (CV) provides additional insight into repeatability: variability is lowest in the mid-range of airflow, where the majority of test points are concentrated, and increases toward the low- and high-flow extremes where fewer data points are available and measurement sensitivity is higher. The combination of smooth mean trends, tight confidence bounds, and modest CV levels demonstrates good repeatability of the experimental data and supports the robustness of the trained sensible and latent effectiveness models for Unit B.

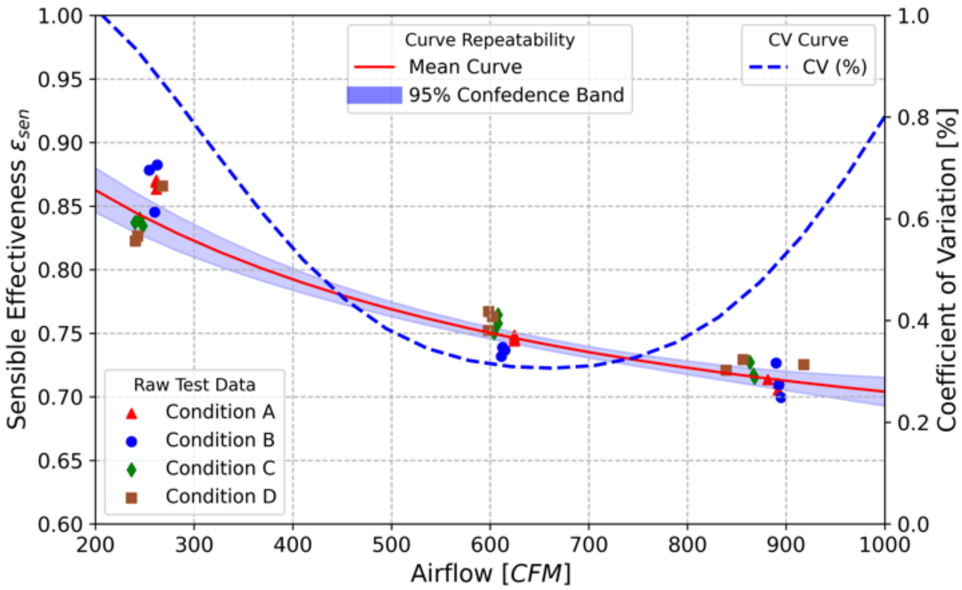

(a)

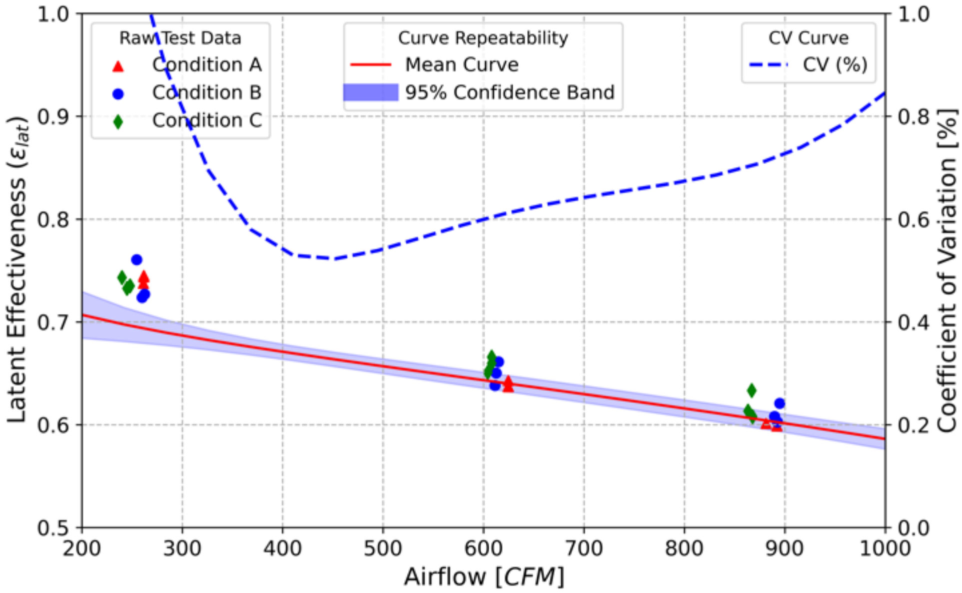

(b)

Figure 4.3: Heat exchanger model training results of Unit B: (a) sensible effectiveness,and (b) latent effectiveness.

4.2.3 Unit C

Figure 4.4 shows the heat exchanger model training results for Unit C, highlighting both the airflow dependence of effectiveness and the consistency of the underlying test data. Compared with Unit B, Unit C exhibits higher effectiveness at lower airflow and a more gradual decline as airflow increases, indicating a stronger baseline heat and mass transfer capability of the core. The raw data from different operating conditions collapse well onto a single trend, suggesting that airflow is the dominant independent variable governing effectiveness for this unit.

The repeatability characteristics also differ from Unit B. For sensible effectiveness, the coefficient of variation exhibits a broader mid-range peak, reflecting greater sensitivity of sensible performance to test-to-test variations at intermediate flow rates. In contrast, latent effectiveness shows relatively uniform variability over most of the operating range, with increased scatter only at the highest airflow where moisture transfer is more limited. Despite these differences, the confidence bands remain well bounded, indicating that the fitted models remain stable and that the observed variability is systematic rather than random. These results confirm that Unit C demonstrates distinct effectiveness behavior while maintaining sufficient repeatability for reliable model development.

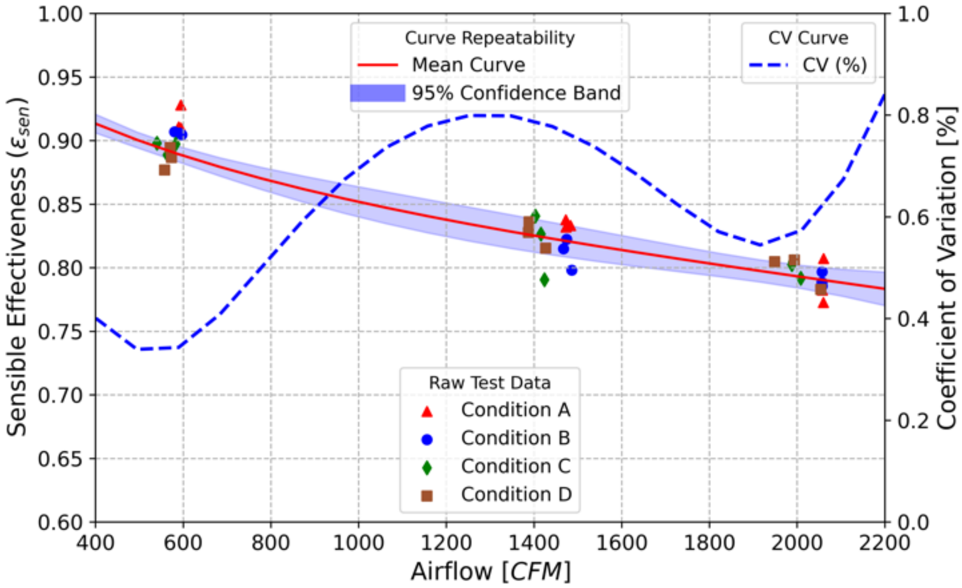

(a)

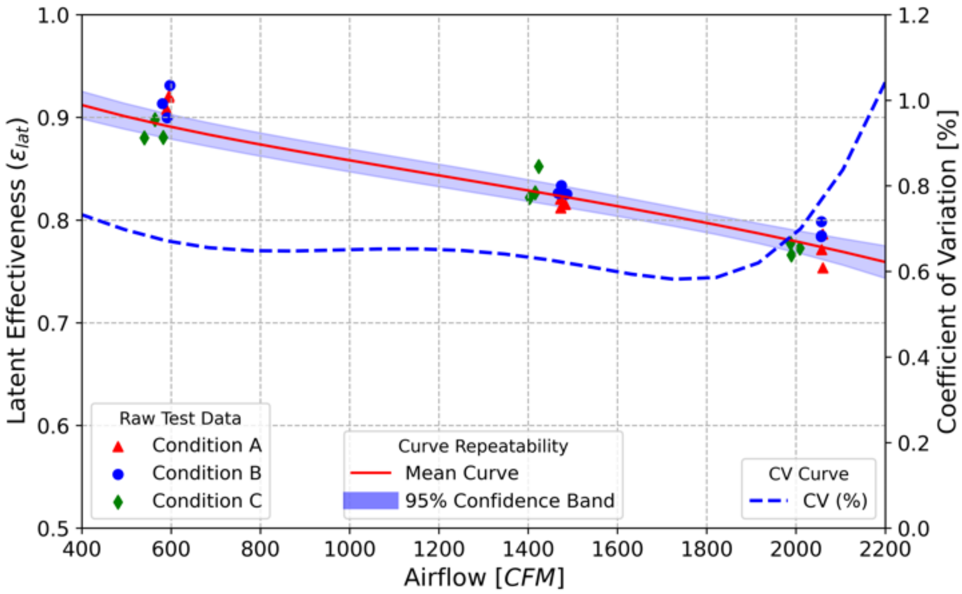

(b)

Figure 4.4: Heat exchanger model training results of Unit C: (a) sensible effectiveness,and (b) latent effectiveness.

4.2.4 Unit D

Figure 4.5 presents the heat exchanger model training results for Unit D and reveals effectiveness characteristics that are distinct from those observed for Units B and C. For both sensible and latent effectiveness, the mean curves show a clear decline with increasing airflow; however, the slope is steeper at lower airflow, indicating that Unit D is more sensitive to changes in face velocity in the low-flow regime. This suggests that core performance for Unit D benefits strongly from increased residence time, but degrades more rapidly as airflow increases. The repeatability behavior of Unit D also differs from the other units. The coefficient of variation is relatively high at low airflow, decreases to a minimum at mid-range airflow, and then increases again toward the upper flow limit. This U-shaped CV trend indicates that measurement and operational variability are most pronounced near the flow extremes, where latent and sensible transfer processes are more sensitive to small deviations in boundary conditions. Despite this, the confidence bands remain reasonably bounded, indicating that the fitted models remain stable and that variability is systematic rather than random. Overall, the results demonstrate that Unit D exhibits stronger airflow sensitivity and more pronounced repeatability variation, underscoring the importance of including sufficient mid-range airflow data when developing performance models for this unit.

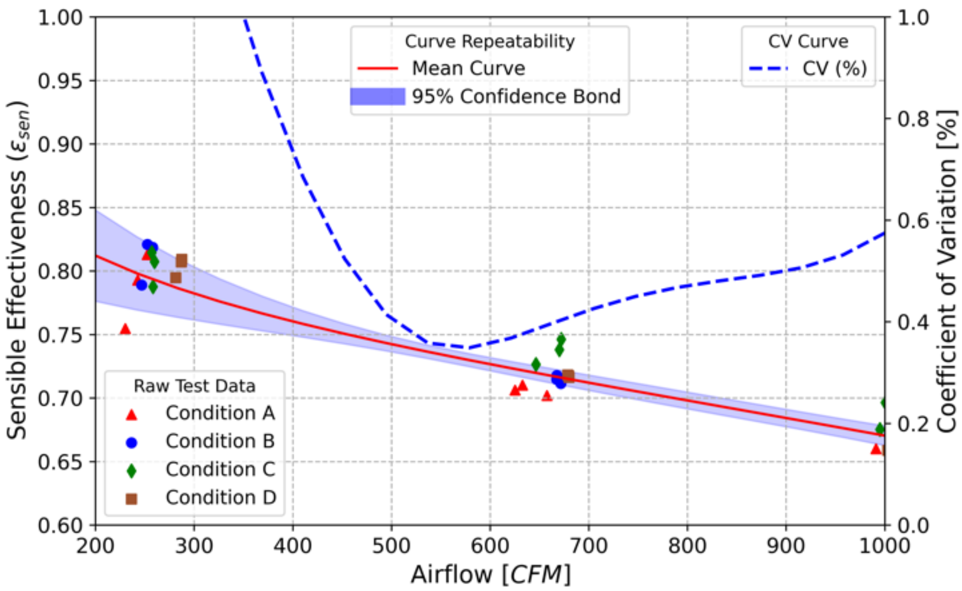

(a)

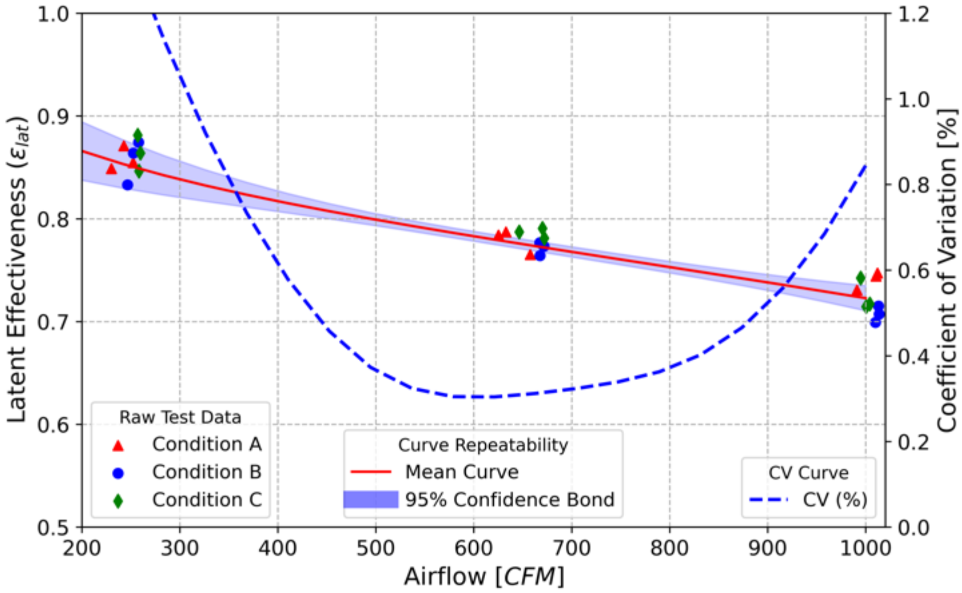

(b)

Figure 4.5: Heat exchanger model training results of Unit D: (a) sensible effectiveness, and (b) latent effectiveness.

5 Seasonal Efficiency

To enable a consistent and climate-representative evaluation of energy recovery system performance, a seasonal coefficient of performance (SCOP) framework based on temperature-bin aggregation is adopted in standard CSA SPE-18. While the coefficient of performance (COP) at a given outdoor air condition reflects the instantaneous ratio of recovered energy to electrical power input, a seasonal formulation is required to assess system performance over a full range of outdoor conditions and operating hours.

For a given operating mode and climate, the seasonal coefficient of performance (SCOP) for the cooling or heating season is defined as the ratio of the total recovered energy to the total electrical energy input, aggregated over all predefined outdoor temperature bins, as shown in Equation 5.1. To better represent efficiency using seasonal aggregation rather than occupancy profiles, and to allow fair comparisons independent of cooling latent recovery (which may be beneficial in some applications and detrimental in others), the equations for $SCOP_{mode}$ and $SCOP_{total}$ in SPE-18 have been replaced by a single seasonal SCOP equation that is applied separately to cooling and heating seasons.

$$SCOP_{\text{season}} = \frac{\sum_{\text{season}} \left[\sum_{n=1}^{31} N_{\text{bin}} \cdot \dot{q}_{s,\text{SA,net,n}} \times CF \right]}{\sum_{\text{season}} \left[\sum_{n=1}^{31} N_{\text{bin}} \times \dot{q}_{\text{total,n}} \right]} \tag{5.1}$$

where:
$SCOP_{season}$ = the seasonal SCOP for a given season includes the defined bin hours for cooling or for heating, respectively:

a) cooling, occupied and unoccupied;

b) heating, occupied and unoccupied.

n = the bin number, where bins are increments of 3°C (5.4 °F) and bins represent outdoor temperature of -42°C (43.6 °F) at bin number 1 and 48°C (118.4 °F) at bin number 31;

N_{bin} = the number of hours in the defined temperature bin for that climate and operating mode as defined in CSA SPE-18 Annex B for 8 different climates: ;

CF = cooling factor equal to -1 for cooling season hour and 1 for heating hours;

$\dot{q}_{\text{total},n}$ = the total energy input at that operating condition, equal to the sum of $\dot{q}_{\text{in,SF}}$, $\dot{q}_{\text{in,SD}}$, $\dot{q}_{\text{in,Saux}}$, $\dot{q}_{\text{in,EF}}$, $\dot{q}_{\text{in,ED}}$, and $\dot{q}_{\text{in,Eaux}}$.

The formulation explicitly accounts for sensible energy in the supply air stream. A cooling factor is applied to maintain consistent sign conventions between heating and cooling modes, enabling a unified SCOP formulation across all operating conditions.

The bin-weighted SCOP formulation provides a robust basis for comparing system performance across 8 different climates (subarctic, very cold, cold and dry, cold and humid, marine, mixed, hot and dry, hot and humid). It uses two operating modes (occupied and unoccupied) as well as whether the building HVAC is in cooling or heating mode during that bin for the defined prototypical small office building. It also aligns with the intent of standardized seasonal performance metrics used for regulatory evaluation and energy modeling.

During the simulation of $SCOP_{season}$, the operating airflow rates and indoor-side conditions are prescribed. In accordance with CSA SPE-18, the indoor air conditions are specified as a dry-bulb temperature of 24°C (75.2°F) and a wet-bulb temperature of 17°C (62.6°F) during the cooling season, and a dry-bulb temperature of 21°C (69.8°F) and a wet-bulb temperature of 11.4°C (52.5°F) during the heating season.

The airflow rate is set to 75% of the maximum (nominal) airflow during occupied periods and 25% of the maximum (nominal) airflow during unoccupied periods. The supply and exhaust airflow rates are maintained in balance for all operating conditions.

Furthermore, the recovered energy calculated for each outdoor temperature bin explicitly accounts for the unit's operating mode, including full recovery, economizer operation, and frost control, as well as whether the building HVAC is in cooling or heating mode during that bin. In full recovery mode, both the outdoor air and room air streams pass entirely through the HX-core, enabling heat (and, where applicable, moisture) transfer between the two airstreams.

Two distinct economizer operation strategies are applied in this study. In economizer mode, the outdoor air is fully or partially bypassed around the HX-core to provide "free cooling" to the conditioned space. Economizer operation is therefore modeled only during cooling hours, and the bypass fraction is determined based on the prevailing operating conditions and the manufacturer's documented control sequences. In this study, the economizer control strategy applied for Unit A, B, and D follows the illustrative example provided in SPE-18. Specifically, when the outdoor air temperature is below 24 °C and above 13 °C, the outdoor air stream fully bypasses the HX-core. When the outdoor air temperature falls below 13 °C, the outdoor air is partially bypassed to maintain a supply air temperature of 13 °C at the HX-core outlet, with the bypass damper progressively closing until it is fully closed under colder conditions.

Unit C, representing a rotary-wheel type ERV, utilizes a stop-start control strategy. When the outdoor air temperature is between 13°C and 24°C, the wheel is stopped, resulting in a bypass factor of 1.0. During this period, only the supply and exhaust fans operate to provide ventilation to the space. Once the outdoor temperature drops below 13°C, the unit resumes Full Recovery Mode, and the bypass factor returns to 0.

In frost control mode, the control sequences are derived from the measured low-temperature test results for each unit and are summarized as follows:

- For Units A and B, frost protection is managed through a multi-stage process involving preheating, air bypassing, and ultimately, system shutdown. The exhaust air temperature leaving the energy exchange core is continuously monitored. If this temperature falls below 5°C, an electric preheater located at the outdoor air intake, upstream of the core, is activated to raise the temperature of the entering outdoor air. If conditions are so severe that the preheater operates at full capacity and the exhaust air temperature leaving the core still drops below 1°C, the unit implements a bypass strategy where a portion of the outdoor air is routed around the core. If the temperature cannot be maintained even with a full bypass, the unit initiates a protective shutdown, halting both the supply and exhaust fans to prevent potential core damage from frost accumulation.

- For Unit C, frost protection is achieved through a simplified shutdown strategy. When the exhaust air temperature leaving the energy exchange core drops below -20°C , both the supply and exhaust fans are temporarily suspended, halting airflow through the core until conditions are sufficiently warm to resume normal operation.

- For Unit D, a duty-cycle-based frost control strategy is employed. When the exhaust air temperature leaving the heat exchange core falls below 2 °C (36 °F), the supply fan is periodically suspended for 1 minute out of every 6 minutes. This intermittent operation allows warmer room air to flow through the core and promote passive frost removal.

This mode-dependent representation ensures that the recovered energy assigned to each temperature bin accurately reflects the actual operational behavior of each unit under varying climatic conditions and control strategies, particularly under low-temperature operation where frost mitigation significantly influences both delivered fresh air rate and energy recovery performance.

5.1 Energy recovery profile and SCOP for Unit A

Unit A operates as a sensible-only heat recovery system, facilitating thermal exchange between airstreams without moisture transfer. System performance was evaluated up to a nominal airflow rate of 933 CFM, representing the maximum flow rate measured during testing when the unit was set for the maximum rated flow of 1000 CFM. In this analysis, the occupied airflow rate was set at 699 CFM (75% of measured maximum airflow), while the unoccupied airflow rate was 233 CFM (25% of measured maximum airflow).

As illustrated in Figure 5.1, the sensible recovered energy rate during the cooling season increases as the temperature difference between the indoor and outdoor grows larger. When the outdoor air (OA) temperature falls below the indoor temperature, the system enters an economizer operation mode where the OA bypasses the heat exchanger (HX) core to provide “free cooling” to the space. To maintain a constant supply air temperature as OA temperatures continue to decrease, the system modulates by redirecting a portion of the air through the HX core. This modulation results in a measured decrease in the recovered energy rate, particularly when the OA temperature is between -3°C and 10°C, as shown in Figure 5.1. Throughout the cooling season, while the unit transitions between full recovery and economizer operations, the total power consumption of the unit remains constant.

During the heating season, the recovered energy rate generally increases as outdoor temperatures drop, though performance is heavily influenced by airflow settings and frost control strategies. Under the occupied airflow rate (699 CFM), the electric preheater activates for frost control when OA temperatures fall below 0°C. Once the preheater reaches its maximum capacity, the system is forced to bypass a portion of the OA around the HX core, which leads to a decline in the rate of increasing recovered energy. In contrast, at the unoccupied airflow rate (233 CFM), the preheater does not reach its maximum capacity even when outdoor temperatures drop below -20°C. Consequently, at this lower flow rate, the system is able to maintain effective heat recovery without the need for a bypass during frost control mode.

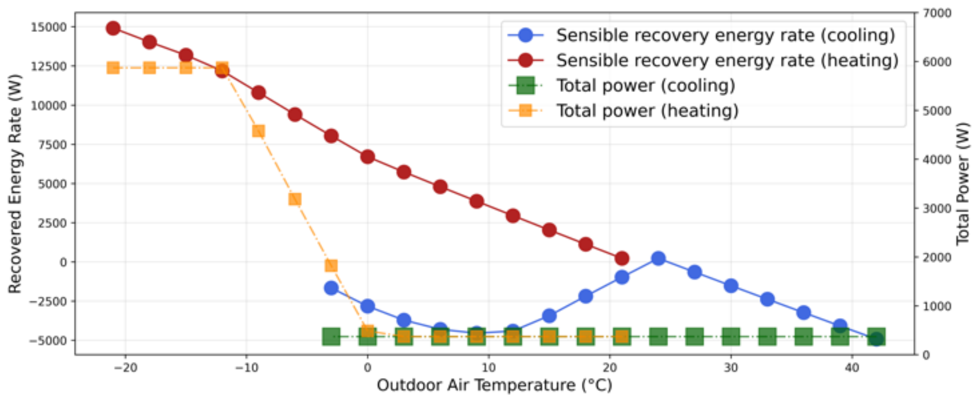

(a)

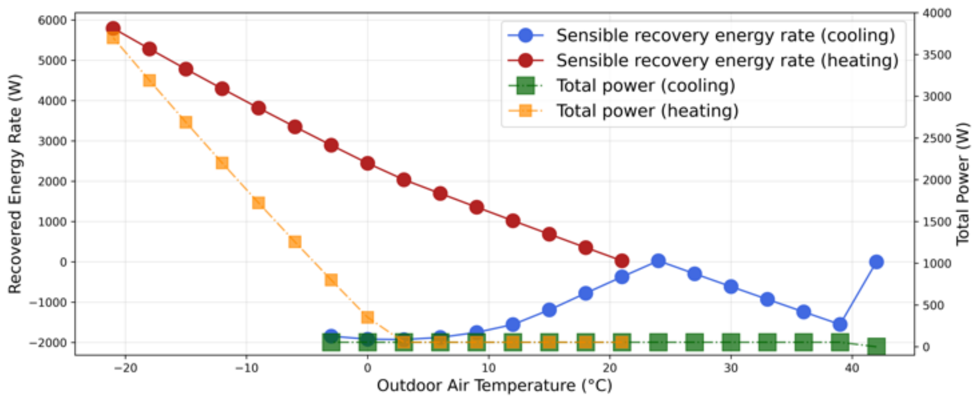

(b)

Figure 5.1: Recovered energy rate for Unit A: (a) occupied (b) unoccupied.

Figure 5.2 illustrates the total sensible recovered energy and associated unit energy consumption across the full range of outdoor temperature bins for two distinct climatic con-

ditions: a cooling-dominated mixed climate and a heating-dominated cold and humid climate. These results were derived by multiplying the sensible energy recovery rates from Figure 5.1 by the total bin hours for each corresponding outdoor temperature.
In the mixed climate, energy recovery occurs across a broad temperature spectrum, though the magnitude of total recovery is most significant during moderate to high outdoor temperatures. While Figure 5.1 indicates that the highest rates of energy recovery occur at extreme outdoor temperatures, Figure 5.2 reveals relatively low total energy recovery during full recovery cooling modes due to the limited number of annual hours at those high temperature bins. Note that cooling energy recovery is signed; that is, a negative value is conserving actively cooled indoor air (above 20 °C) or introducing pre-cooled outdoor air during economizing (below 20 °C). Also note the varying x- and y-axis scales for each climate. During economizer operation, the highest levels of total energy recovery are observed at an outdoor temperature of 12°C. This is attributed to the high number of bin hours at this temperature combined with the high amount of "free cooling" resulting from a significant temperature difference between the indoor and outdoor. Heating recovery in this climate is concentrated in the lower temperature bins but remains low relative to the heating-dominated scenario.

Performance in the cold and humid climate is characterized by a heavy concentration of recovered energy in the heating domain. Sensible recovered energy for heating increases significantly as outdoor temperatures drop toward 0°C. However, as temperatures descend further into the freezing range, the impact of the frost control strategy becomes more pronounced. Due to these extreme low temperatures, the unit's energy consumption for heating increases sharply to support the preheating required for frost prevention. This consumption peaks at temperatures where the preheater reaches its maximum capacity, at which point the energy recovery rate begins to stabilize or decline as a portion of the outdoor air is bypassed.

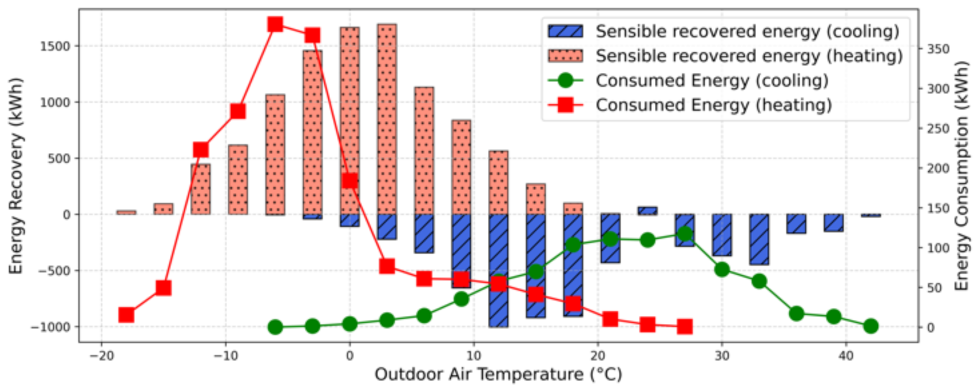

(a)

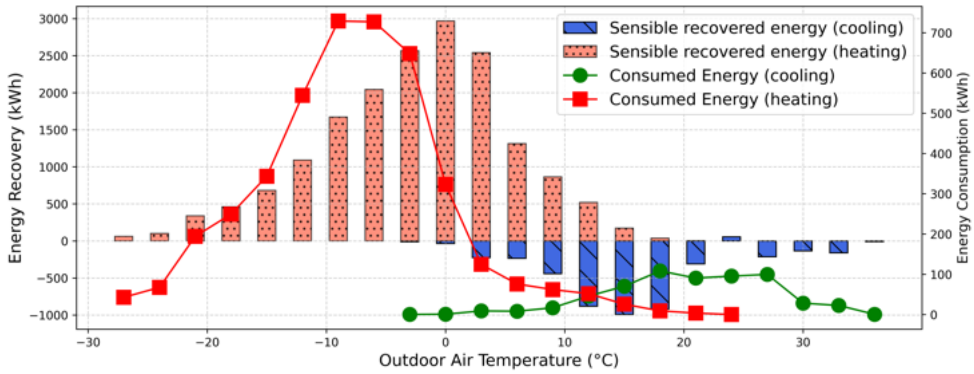

(b)

Figure 5.2: Recovered energy and energy consumption of Unit A for climates: (a) mixed (b) cold and humid.

The total seasonal efficiency of the unit, represented by the $SCOP_{total}$ in Figure 5.3, varies significantly across the eight climate zones for both cooling and heating modes. To verify the repeatability of the SCOP calculations based on lab test results, three groups of SCOP values are plotted for each climate zone, derived from three distinct sets of coefficient tuning from independent testing data. The minimal variance between these data points indicates high repeatability and reliability of the laboratory testing procedures.

In the cooling domain, the system exhibits higher SCOP values in colder regions where, during the cooling season, the units predominantly operate in economizer mode despite the relatively limited hours of cooling operation. The maximum cooling SCOP is recorded in the subarctic climate, peaking at approximately 14.9. The hot-humid climate demonstrates the lowest cooling performance, with SCOP values declining to a range of 5.8–5.9. Across all climate zones, cooling SCOP remains relatively stable, though a marginal difference in SCOP is observed across the three tested data groups.

The heating SCOP values are generally lower than those observed in cooling for cold climates, primarily due to the necessary activation of frost control. The marine climate exhibits the highest heating SCOP, with values between 12.5 and 12.7. This peak performance is attributed to moderate winter outdoor temperatures that allow for maximum recovery without frequently triggering the energy-intensive electric preheater. In contrast, the subarctic and very cold climates show significantly lower heating SCOP values, ranging from 2.7 to 3.6. The unit maintains a high heating SCOP (above 10.0) in hot-dry and hot-humid climates. While total heating hours and indoor/outdoor temperature differences in these regions are limited, the system operates with high SCOP because frost control is not required.

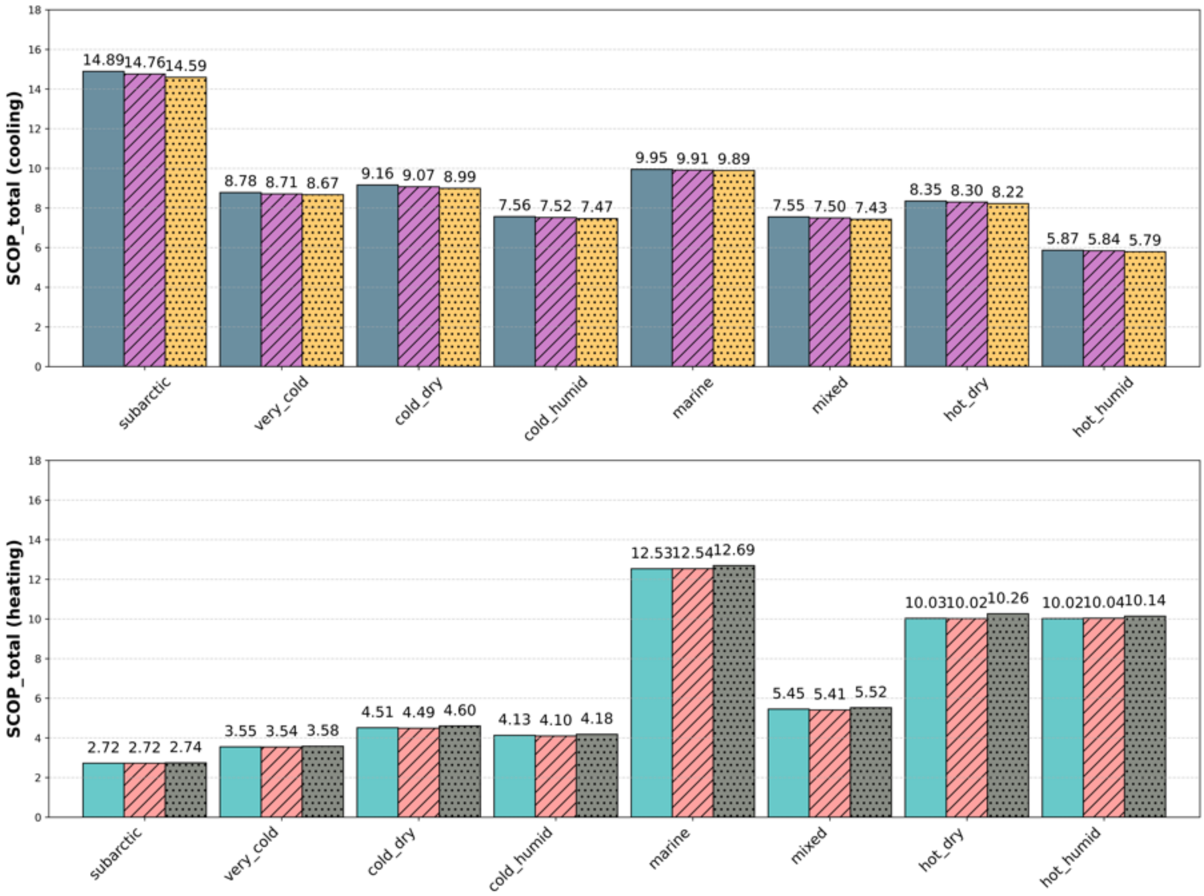

Figure 5.3: Total SCOP of Unit A: (top) cooling, (bottom) heating (clear=Test 1, hatched = test 2, dots = test 3)

5.2 Energy recovery profiles and SCOP for Unit B

In contrast to the sensible-only operation of Unit A , Unit B functions as an energy recovery system that facilitates both sensible and latent thermal exchange between the two airstreams. The performance of this unit was evaluated up to a nominal airflow rate of 910 CFM, which represents the maximum flow rate measured during testing. Following the established analytical framework, Unit B was assessed under two primary operational conditions: an occupied airflow rate of 683 CFM (75% of nominal) and an unoccupied airflow rate of 228 CFM (25% of nominal).

Figure 5.4 illustrates the sensible and latent recovered energy rates across a wide range of outdoor temperatures. To calculate the latent energy recovery, the corresponding outdoor dewpoint temperatures were determined based on the standard appendix for a mixed climate in cooling mode and a cold and humid climate in heating mode. During the cooling season, the system exhibits robust energy recovery across both sensible and latent components. In high-temperature conditions between 25°C and 30°C, the latent recovery energy rate equals or exceeds the sensible rate, reflecting the unit's capacity to manage significant moisture loads alongside temperature.

In the heating domain, the sensible recovery rate is similar to the performance observed for Unit A. The system's performance is heavily dictated by airflow settings and frost control logic. Under the occupied airflow rate (683 CFM), the electric preheater activates for frost control when outdoor air (OA) temperatures fall below 0°C. Once the preheater reaches maximum capacity, a portion of the OA is bypassed around the heat exchanger core, resulting in a plateau or subsequent decline in the recovered energy rate. Conversely, at the unoccupied airflow rate (228 CFM), the preheater does not reach its maximum capacity even as temperatures drop toward -20°C, allowing the system to maintain stable heat recovery without requiring a bypass.

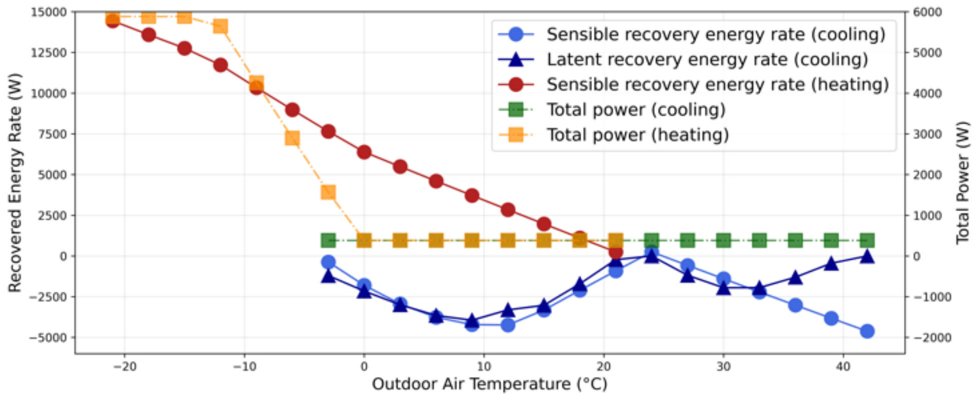

(a)

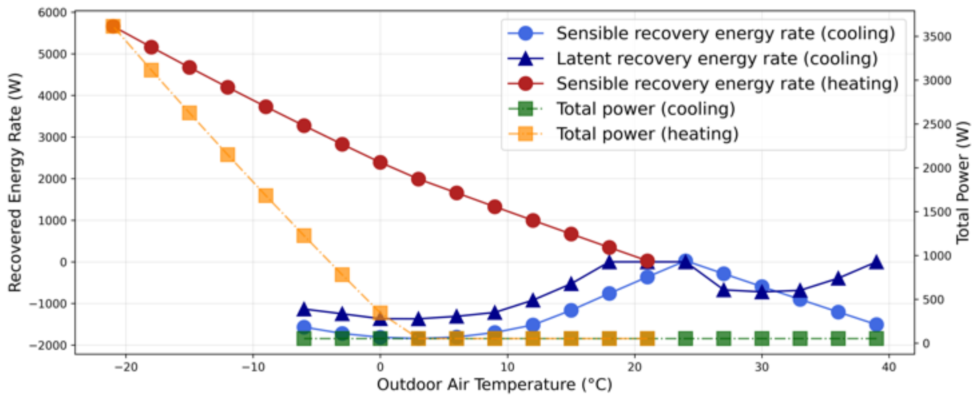

(b)

Figure 5.4: Recovered energy rate for Unit B: (a) occupied (b) unoccupied.

Similar to Unit A, Figure 5.5 illustrates the total recovered energy for mixed as well as cold and humid climates, which was calculated by multiplying the sensible and latent energy recovery rates from Figure 5.4 by the annual bin hours for each corresponding outdoor temperature. In this analysis, latent recovered energy is displayed during the cooling season when the conditioned space requires dehumidification, in accordance with SPE-18, whereas it is not factored into the heating season calculations.

The data indicates that latent energy recovery is particularly significant during the hot and humid summer months, as Unit B addresses substantial moisture loads alongside sensible cooling. While Figure 5.4 indicates that the highest rates of energy recovery occur at extreme outdoor temperatures, Figure 5.5 reveals relatively low total energy recovery during full recovery cooling modes due to the limited number of annual hours at those high temperature bins. When the outdoor air is colder and drier than the indoor environment, the “free cooling” process simultaneously reduces both the sensible and latent loads within the space. In the mixed climate specifically, the highest levels of total recovery occur at an OA temperature of 12°C due to the high bin hours and the effectiveness of this full economizer mode. Performance in the cold and humid climate is characterized by a heavy concentration of recovered energy in the heating domain, where sensible recovered energy increases significantly as outdoor temperatures drop toward 0°C.

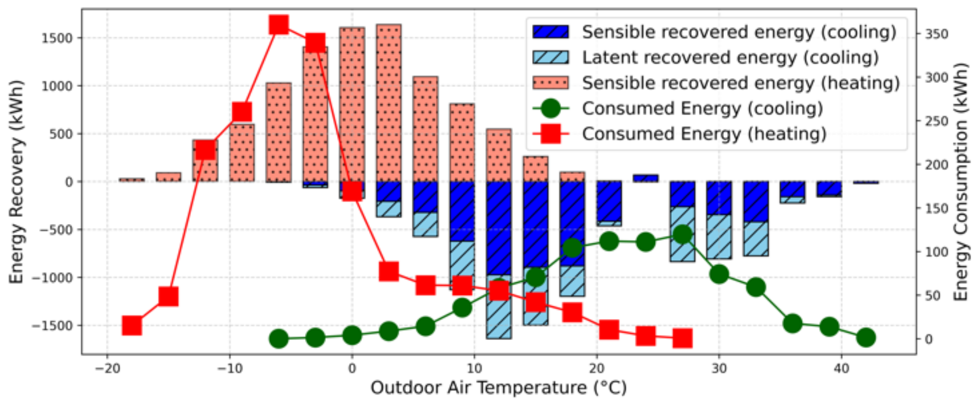

(a)

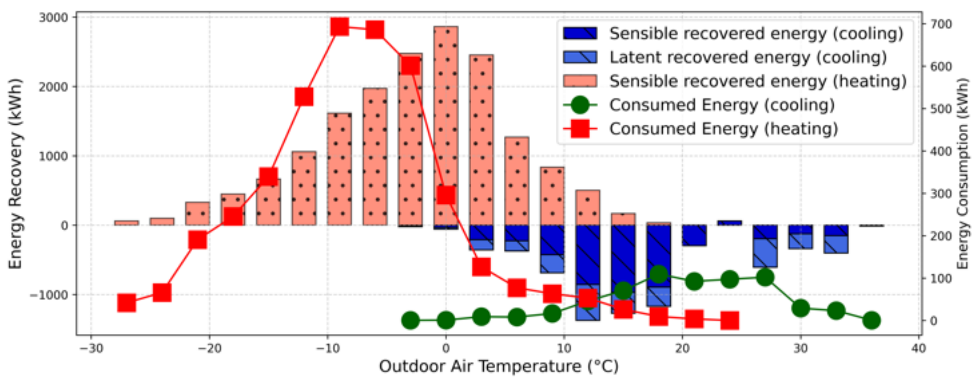

(b)

Figure 5.5: Recovered energy and energy consumption of Unit B for climates: (a) mixed (b) cold and humid.

Figure 5.6 illustrates the cooling and heating SCOP for each climate. Although the contribution of latent exchange in Unit B is displayed according to SPE-18, this study will focus only on the sensible portion of cooling SCOP. To ensure the reliability of these findings, three groups of SCOP values were plotted for each climate zone, derived from distinct sets of coefficient tuning from independent laboratory testing data. The minimal variance between these data points confirms high repeatability and reliability in the calculation procedures.

For both sensible cooling and heating, the SCOPs follow a very similar profile to those of unit A, which is the same unit with an HRV heat exchanger. All the SCOPs are slightly lower for unit B, which may be due to the heat exchanger design that is designed to accommodate latent heat exchange. Figure 5.6 shows that the SCOP is significantly higher when the latent recovery is included, than the sensible-only in all regions. This gap is most pronounced in hot-humid and hot-dry climates, reflecting the unit's ability to manage substantial latent (moisture) loads alongside temperature. However, this study recommends that latent cooling recovery be removed from the cooling SCOP metric, and that the latent performance model still be published so that it can be employed as needed for design and simulation purposes. The heating SCOP values are generally lower than those observed in cooling for cold climates, primarily due to the activation of frost control. The marine climate exhibits the highest heating efficiency, with SCOP values between 12.1 and 12.2. This is attributed to moderate outdoor temperatures that allow for maximum energy recovery without frequently triggering the energy-intensive electric preheater. In subarctic and very cold climates, heating SCOP is significantly lower, ranging from 2.7 to 3.6, due to the system's frost control logic.

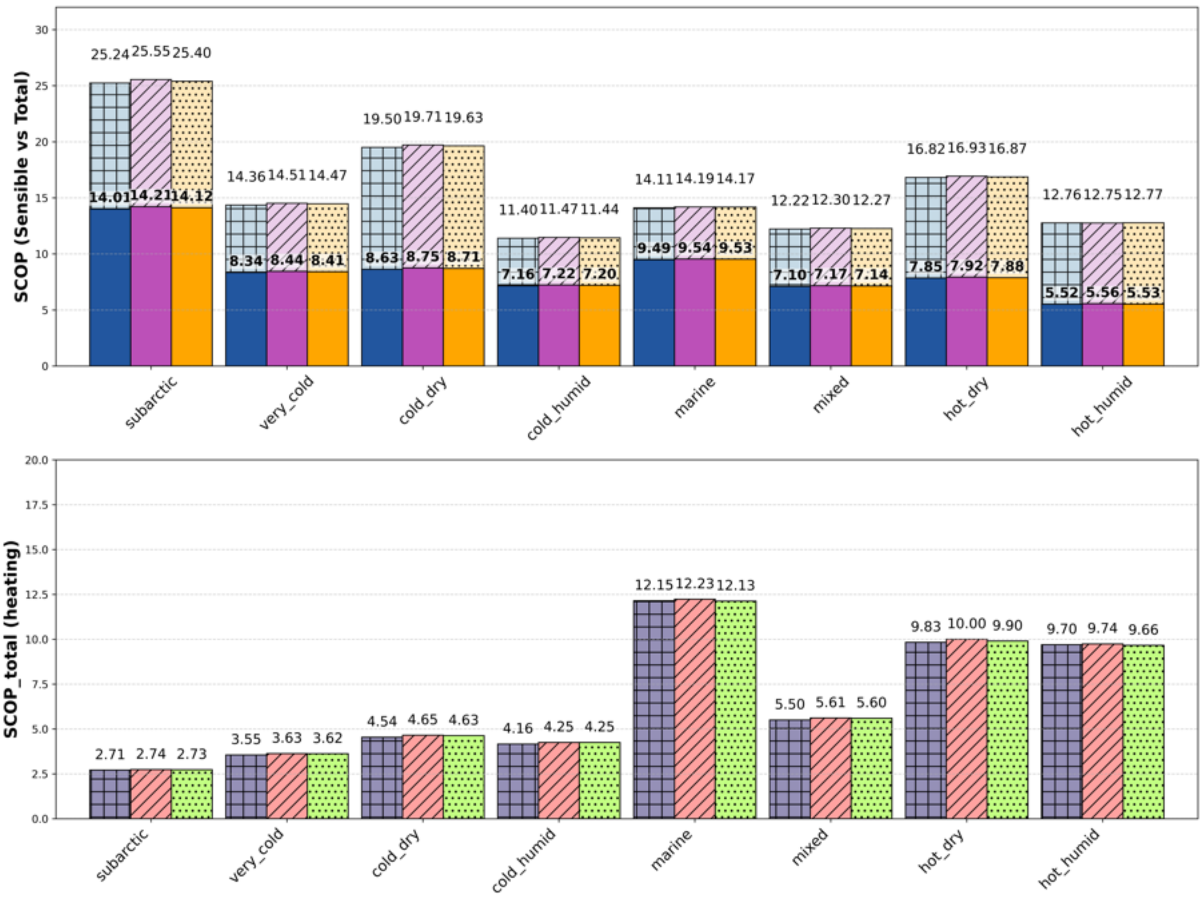

Figure 5.6: Total SCOP of Unit B: (top) cooling, (bottom) heating (clear=Test 1, hatched = test 2, dots = test 3).

5.3 Energy recovery profiles and SCOP for Unit C

Unit C exhibits a distinct performance trend, as illustrated in Figure 5.7. This divergence is primarily attributed to the fact that Unit C utilizes an enthalpy wheel, whereas Unit B employs a fixed-plate heat exchanger. Furthermore, Unit C applies distinct economizer and frost protection strategies that significantly alter its operational profile compared to Unit B. Unit C employs a distinct operational logic for its economizer mode. As the OA temperature decreases from 24°C to 15°C, both sensible and latent recovery rates increase steadily. This performance is achieved by stopping the rotation of the enthalpy wheel, allowing the system to maximize "free cooling". A notable advantage of this strategy is the reduction in power consumption during this interval, as the energy required to drive the wheel motor is eliminated. When the OA temperature falls below 12°C, the economizer mode is terminated, and the system modulates airflow. This transition initially results in a significant reduction in the recovered energy rate; however, as the OA temperature continues to decline, the recovery rate begins to rise again due to the increasing thermal gradient between the indoor and outdoor environments. Consequently, the unit's power consumption returns to standard operational levels as the recovery components are reactivated. The heating performance of Unit C diverges significantly from Unit B, particularly regarding frost protection. During the heating season, the energy recovery rate for Unit C increases linearly as the OA temperature decreases, maintaining this consistent trend down to -24°C. Unlike Unit B, which activates an electric preheater and initiates air bypass at 0°C to prevent frost, Unit C does not require frost control activation within this temperature range. As a result, the unit maintains stable power consumption throughout the heating season and avoids the recovery penalties associated with bypassing the heat exchanger core.

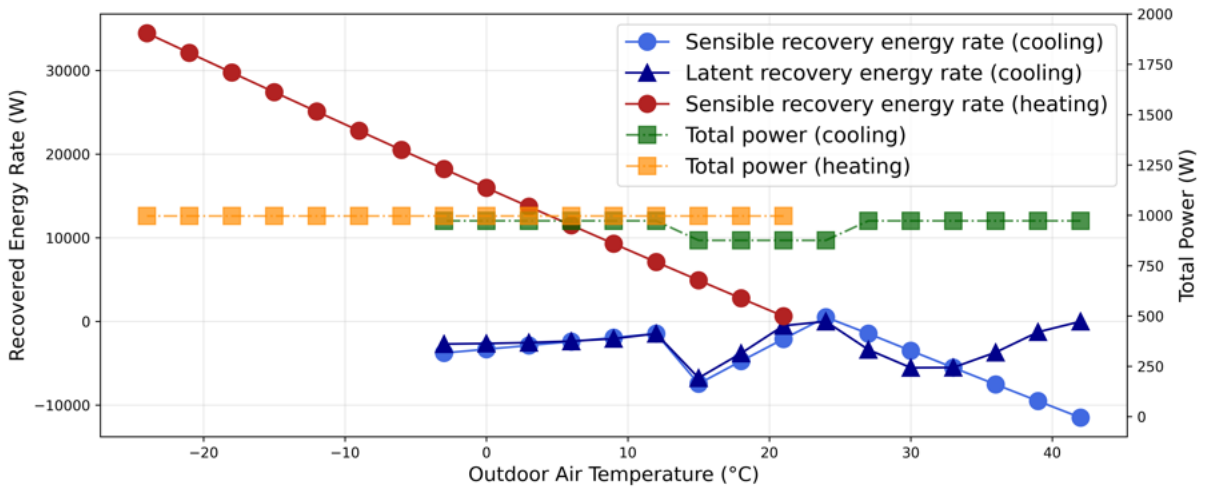

Figure 5.7: Recovered energy rate for Unit C.

Figure 6.8 presents the SCOP of Unit C across the eight climate zones for both cooling and heating modes. As with the preceding units, three groups of SCOP values are plotted for each climate zone, each derived from an independent set of coefficient tuning from laboratory testing data. The minimal spread among the three data groups confirms the high repeatability of the test results and the robustness of the empirical model.

In the cooling domain, the relationship between climate zone and SCOP follows a pattern broadly consistent with Units A and B, with higher SCOP observed in colder regions where economizer operation predominates. Of course, a higher SCOP in a cooler climate likely represents less energy savings, because of the relatively smaller actual cooling load in those climates, so SCOP should always be considered in relationship with the total seasonal loads. The notably lower cooling $SCOP_{total}$ relative to Unit reflects the higher power input to unit C, per unit of air flow. This is in turn largely driven by the fan motors that are notably less efficient at the lower, unoccupied, air flow rate (where the impact is also the most significant). Also, unit C requires power to the wheel motor, which is modest but fairly constant under all operating conditions (see Figure 5.10). Across warmer climates, the latent SCOP increases progressively from cold-dry through hot-dry zones, peaking in the hot-dry and hot-humid climates at approximately 8.7–8.8. This trend is attributable to the enthalpy wheel's latent recovery capacity, which becomes increasingly beneficial as outdoor humidity loads intensify in warmer climates — an inversion of the pattern observed in sensible-only Unit A.

In the heating domain, Unit C exhibits substantially higher heating SCOP values compared to the previously discussed units across all climate zones. This is a direct consequence of its simplified wheel modulation (followed by shutdown) frost control strategy: rather than activating an energy-intensive electric preheater, Unit C temporarily suspends fan operation when the exhaust air temperature leaving the energy exchange core drops below 0°C. This approach avoids the significant energy penalty associated with electric preheating, thereby maintaining favorable SCOP values even in the coldest climates. The subarctic climate records the highest heating SCOP, with values of approximately 19.1–19.3, while the hot-humid climate yields the lowest heating SCOP at approximately 8.1–8.2. The relatively modest variation across climate zones in heating mode reflects the consistent effectiveness of the wheel modulation defrost strategy, which does not impose a variable preheating load as outdoor temperatures decline, as well as a significantly reduced rate of frost accumulation in the heat exchanger wheel itself. The three independently tuned SCOP groups show minimal divergence across all climate zones, further affirming the reliability and repeatability of the seasonal performance characterization for Unit C.

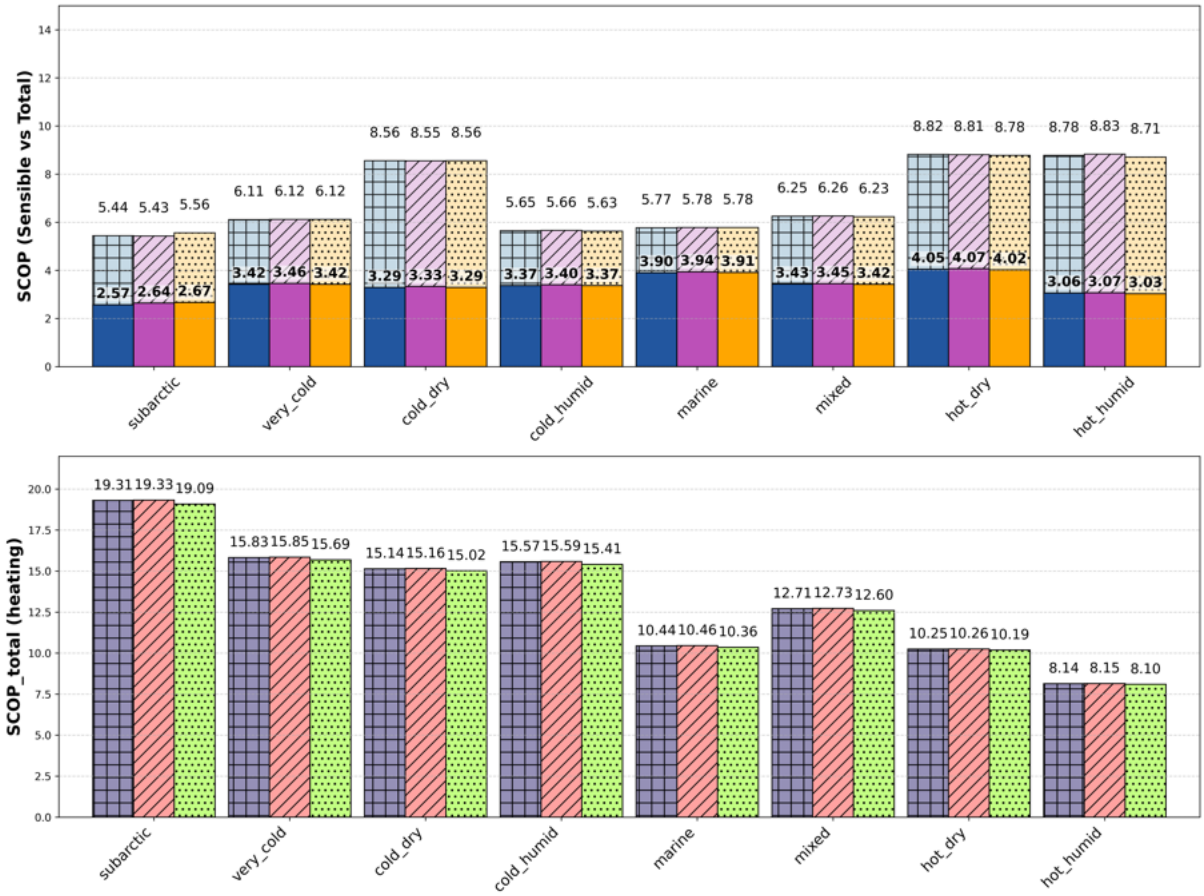

Figure 5.8: Total SCOP of Unit C (clear=Test 1, hatched = test 2, dots = test 3).

5.4 Energy recovery profiles and SCOP for Unit D

Figure 6.9 presents the SCOP of Unit D across the eight climate zones for both cooling and heating modes. Similarly, three groups of SCOP values are plotted for each climate zone, corresponding to independent sets of coefficient tuning from distinct laboratory test datasets. The close agreement among these three groups across all climates confirms the high repeatability of the test-based performance models and supports the reliability of the resulting seasonal efficiency estimates.

In the cooling domain, Unit D demonstrates a climate dependence broadly similar to that of Unit B, with higher sensible SCOP achieved in colder climates where economizer operation is dominant. As observed with Unit B, the gap between sensible and latent persists across all climate zones, indicating a consistent contribution of latent recovery.

In the heating domain, Unit D achieves high SCOP values across all climate zones, a characteristic attributable to its duty-cycle-based frost control strategy. The supply fan is periodically suspended for one minute in every six-minute cycle when the exhaust air temperature leaving the core falls below 2°C. This intermittent strategy allows warmer room air to flow through the core and promote passive defrosting, thereby avoiding the sustained energy penalty of resistive heating. The subarctic climate registers the highest heating SCOP, approximately 20, while the hot-humid climate records the lowest at approximately 8.6. Across all intermediate climate zones, heating SCOP values remain elevated, reflecting the effectiveness of the duty-cycle approach in preserving energy recovery performance even under low-temperature conditions. The three independently derived SCOP groups exhibit minimal variance across all eight climate zones, confirming the repeatability of the testing procedures and the stability of the fitted performance models for Unit D.

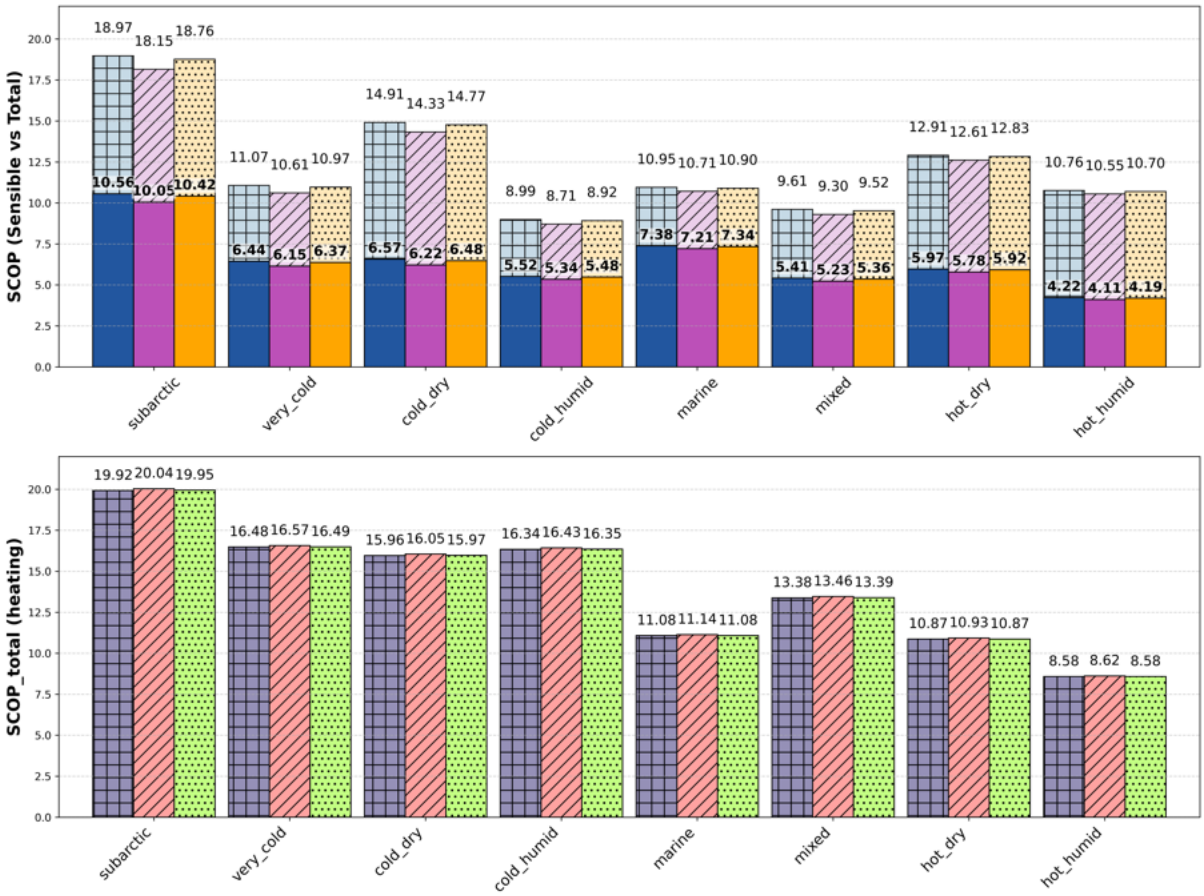

Figure 5.9: Total SCOP of Unit D (clear=Test 1, hatched = test 2, dots = test 3).

5.5 Summary and Cross-Unit Comparison

Among the four units evaluated in this study, Units B and D are the most directly comparable in terms of heat exchanger technology: both are plate-type ERVs capable of simultaneous sensible and latent recovery, tested at similar nominal airflow rates. Unit A, a plate-type HRV with sensible-only exchange, and Unit C, a wheel-type ERV, represent distinct technology classes and therefore serve as important reference points that bracket the performance space defined by Units B and D.

In the cooling domain, maintaining the focus on sensible SCOP, the most significant distinction among the four units is the difference in fan motor efficacy, and overall power requirement, as a function of airflow. Units A and B use the same fans, with slight variations because of differences in heat exchanger design. Although unit C has the highest sensible effectiveness of all the units (Fig 3.11 (b)), followed by units A and B (Figs 3.3 (b) and 3.7 (b))), unit C has significantly lower airflow efficacy (in CFM/W) at the unoccupied speed of 25%, as shown in Fig 5.10. Unit C also requires power for the wheel rotation motor; although it has a similar airflow efficacy to Units A and B between 50-100% of its rated air flow, the added wheel motor power pushes the overall air flow efficacy to the lowest of the four at every flow rate. Unit D, although it has slightly higher airflow efficiency than units A and B at the higher flow rates, drops to almost match Unit C at the unoccupied 25% flow rate, less than 40% that of units A and B. The lower airflow efficacy of unit C may partly be explained by the higher rated flow (double that of the other 3 units), but is also affected by the added power of the wheel motor, and the net result dominates the cooling SCOP of unit C despite its very high recovery effectiveness. Cooling SCOP for Unit D ends up in the middle, driven by lower recovery effectiveness than units A and B and low fan efficacy at the unoccupied condition, but counterbalanced by a high flow efficacy at the occupied condition.

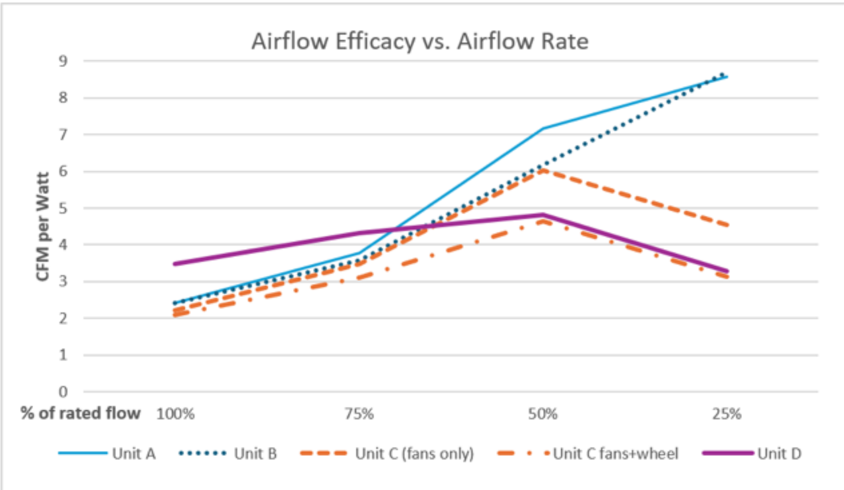

Figure 5.10: Airflow efficacy vs. airflow rate.

The heating comparison reveals a different and in several respects more instructive picture, because the primary driver of performance is frost control strategy. Unit A and Unit B share an identical electric preheater-based defrost mechanism, and their heating SCOP profiles are correspondingly similar. Unit B's values follow the same pattern. The close alignment between Units A and B in heating SCOP confirms that the preheater imposes an energy penalty severe enough to largely negate whatever additional recovery potential Unit B's membrane core offers over Unit A's sensible-only plate. Units C and D, by contrast, avoid resistive preheating entirely. Unit C employs a wheel-speed modulation strategy followed by a second shut-down stage, while Unit D uses a duty-cycle-based approach. Both achieve substantially higher heating SCOP across all cold climates at the expense of reduced ventilation rates in cold outdoor conditions (in the case of unit C, only very cold conditions). The two non-preheater units track each other closely across all climates, with Unit D holding a modest but consistent advantage in the coldest zones attributable to its duty-cycle strategy maintaining partial airflow continuity through the core — whereas Unit C's full shutdown strategy halts recovery entirely during defrost events at the coldest temperatures.

The comparison across all four units therefore resolves into two analytically distinct groupings that cut across technology class. In the cooling domain, the grouping is defined by the air-moving efficacy of the unit, with units A and B showing high efficacy, and C and D having lower efficacy, especially at lower airflow rates. Also, economizer strategy affects the cooling performance. In latent recovery, which this study recommends removing from the cooling SCOP metric, additional energy savings depends on climate and heat exchanger type. In the heating domain, the grouping is defined by frost control strategy: Units C and D achieve heating SCOP values four to five times higher than Units A and B in cold and very cold climates, despite spanning two different heat exchanger technologies, while Units A and B — one a plate-type HRV and one a plate-type ERV — converge to nearly identical heating SCOP because latent recovery is excluded from the heating season SCOP calculation and both units share the same resistive preheating logic, which imposes an energy penalty as outdoor temperatures decline. This result carries a direct implication for how the CSA SPE-18 framework should be applied and communicated.

6 Tracer Gas Testing

6.1 Tracer Gas Testing Setup

Tracer gas leakage testing was conducted to quantify crossflow leakage between air streams in both the plate-type HRV and wheel-type ERV units. Sulphur Hexafluoride (SF_6) was selected as the tracer gas for testing.

Two airflow configurations were implemented. The plate-type HRV was tested in an open-loop configuration, where all airstreams were open to ambient environment. In contrast, the wheel-type ERV was tested with a closed Room Air–Exhaust Air (RA–EA) loop. In the closed-loop configuration, the exhaust stream was recirculated to the room air inlet, allowing tighter control of tracer gas conditions, reducing the influence of ambient dilution and reducing tracer gas usage. SPE-18 shows only the open-loop configuration, but Purdue recommends that the procedure be changed to incorporate the half-closed loop as an option.

Tracer gas was injected upstream of the Room Air (RA) station to establish a concentration gradient across the energy recovery core. Gas concentrations were measured at the Outdoor Air (OA), Supply Air (SA), and Room Air (RA) stations. Differential pressure transducers were installed at OA, SA, RA, and EA locations to monitor static pressure relationships throughout the tests.

The Air Transfer Ratio, representing exhaust air contamination to the supply stream, is calculated as

$$R = \frac{B_2 - B_1}{B_3} \times 100\% \tag{6.1}$$

where B_1, B_2, and B_3 denote the tracer gas concentrations at OA, SA, and RA, respectively. The values indicate contaminant transfer from the exhaust/room side to the supply air stream.

Three pressure relationships were evaluated for both units: condition 1: approximately balanced pressure between RA–EA and OA–SA, condition 2: RA–EA greater than OA–SA, and condition 3: RA–EA less than OA–SA. For each condition, steady-state periods were identified and averaged for quantitative analysis.

6.2 Plate-Type HRV Results

Figure 6.1 presents the measured pressure differentials during the three test conditions for unit A. It clearly indicates different pressure conditions between the balanced, positive differential, and negative differential cases.

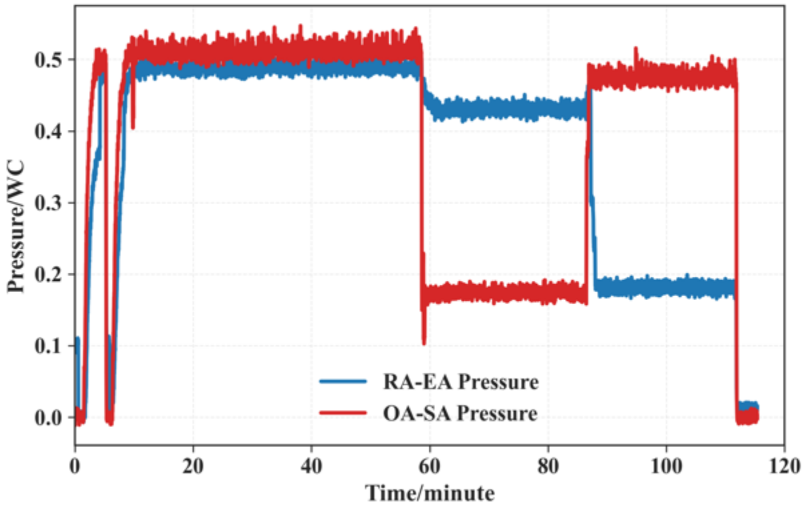

Figure 6.1: Pressure differential profiles for the plate-type HRV under the three test conditions.

The corresponding Air Transfer Ratios are shown in Figure 6.2, and the averaged steady-state concentrations are summarized in Table 3.

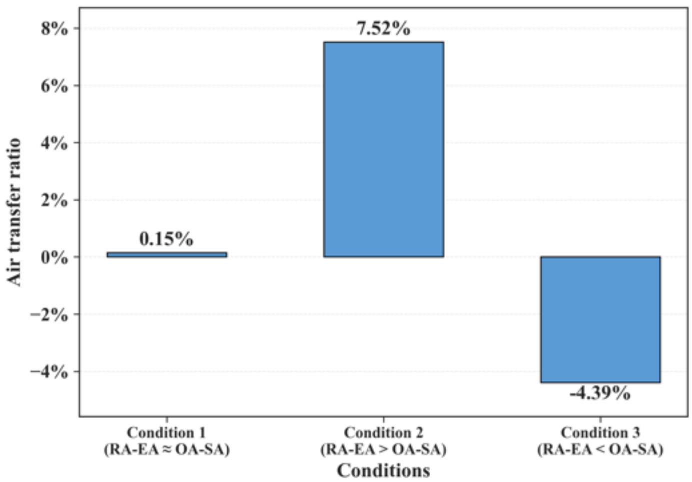

Figure 6.2: Air Transfer Ratio for the plate-type HRV under the three pressure conditions.

	Condition 1 (Balanced)	Condition 2 (RA–EA > OA–SA)	Condition 3 (RA–EA < OA–SA)
OA Concentration (ppm)	219.42	247.21	233.79
RA Concentration (ppm)	391.29	491.80	408.68
SA Concentration (ppm)	220.00	284.20	215.85
RA–EA Pressure (in. w.c.)	0.490	0.431	0.182
OA–SA Pressure (in. w.c.)	0.513	0.174	0.476
Air Transfer Ratio (%)	0.15	7.52	-4.39

Table 3: Plate-Type HRV Tracer Gas Results

Under balanced pressure, the plate-type unit exhibited negligible leakage, with an Air Transfer Ratio of 0.15%, indicating effective separation between air streams. When the RA–EA pressure exceeded the OA–SA pressure, the transfer ratio increased substantially to 7.52%, demonstrating strong pressure-driven cross-contamination from the exhaust side to the supply side. Conversely, when RA–EA was lower than OA–SA, a transfer ratio of -4.39% was observed, indicating a reverse pressure gradient that suppressed contaminant migration into the supply stream.

Because the system operated in an open-loop configuration, the OA concentration was influenced by ambient conditions. This introduces additional variability in the calculated ratios, particularly under small differential conditions.

6.3 Wheel-Type ERV Results

The wheel-type ERV, Unit C, was tested with a closed RA–EA loop, resulting in significantly lower tracer gas usage. Figure 6.3 presents the pressure differentials achieved during the three test conditions.

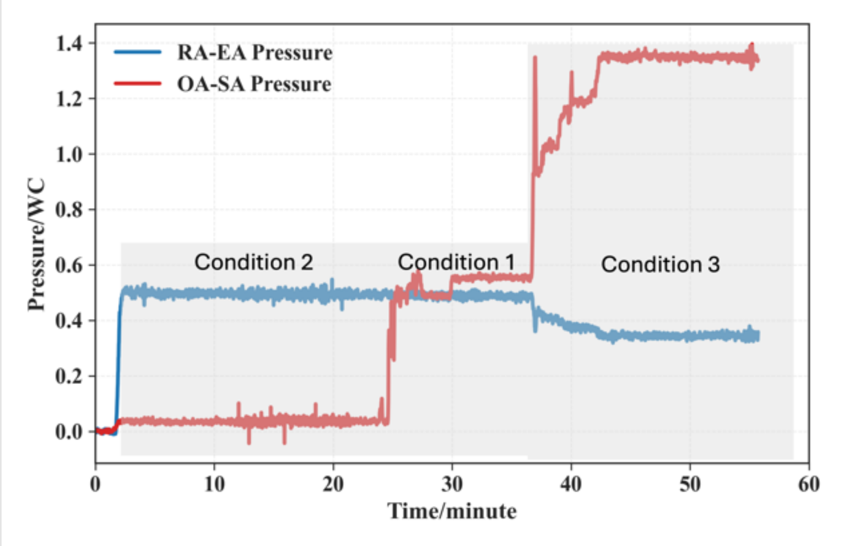

.

Figure 6.3: Pressure differential profiles for the wheel-type ERV under the three test conditions (note that conditions 1 and 2 are reversed in time sequence)

The calculated Air Transfer Ratios are shown in Figure 6.4, with averaged concentrations summarized in Table 4.

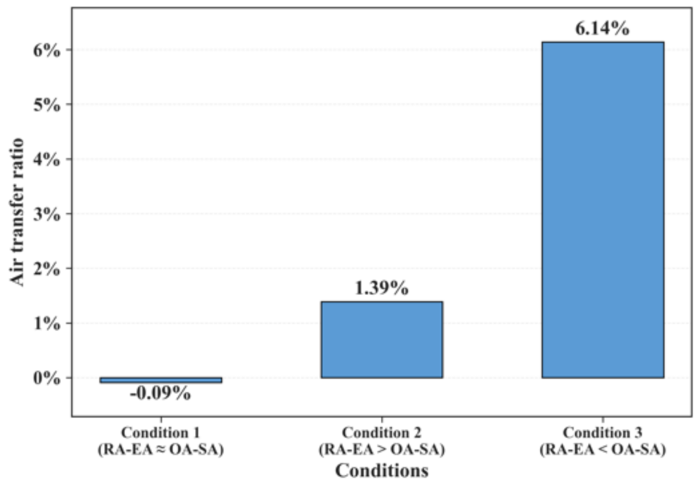

Figure 6.4: Air Transfer Ratio for the wheel-type ERV under the three pressure conditions.

	Condition 1 (Balanced)	Condition 2 (RA–EA > OA–SA)	Condition 3 (RA–EA < OA–SA)
OA Concentration (ppm)	22.61	18.16	25.69
RA Concentration (ppm)	244.31	410.64	360.64
SA Concentration (ppm)	22.40	23.87	47.84
RA–EA Pressure (in. w.c.)	0.489	0.496	0.344
OA–SA Pressure (in. w.c.)	0.555	0.034	1.349
Air Transfer Ratio (%)	-0.09	1.39	6.14

Table 4: Wheel-Type ERV Tracer Gas Results

Under balanced pressure, the wheel-type unit exhibited near-zero transfer (-0.09%), indicating effective separation under equilibrium conditions. When RA–EA exceeded OA–SA, the transfer ratio increased to 1.39%, which is lower than the corresponding plate-type result. However, when RA–EA was lower than OA–SA, the transfer ratio increased to 6.14%. This behavior differs from the plate-type unit and suggests that leakage mechanisms in the rotary wheel include not only pressure-driven flow but also rotational carryover and seal-related effects.

6.4 Comparison and Discussion

The two units demonstrate different leakage characteristics. The plate-type exchanger exhibits predominantly pressure-driven behavior, with leakage strongly dependent on the direction and magnitude of the static pressure differential. In contrast, the wheel-type exchanger shows measurable transfer even under pressure conditions that would suppress leakage in a fixed-plate core. This behavior indicates the presence of additional transport mechanisms associated with the rotating wheel, including rotational carryover and seal-related leakage paths.

It should be noted that the airflow and pressure configurations differed between the two tests. For the wheel-type unit, the RA–EA loop was closed, and the pressure in this loop could not be independently adjusted during testing. Only the OA–SA loop pressure was actively controlled. In contrast, the open-loop configuration of the plate-type unit allowed independent adjustment of both air streams. As a result, the absolute pressure levels in the wheel-type close-loop setup were higher than those in the plate-type tests, which may influence leakage behavior and the resulting transfer ratios. Therefore, in addition to pressure differential, absolute pressure levels may also influence seal deformation and internal leakage pathways, particularly for rotary systems.

Operational control of tracer gas concentration also differed between configurations. In the open-loop test, tracer gas concentration was influenced by ambient dilution and potential accumulation in the surrounding environment. This configuration required substantially higher tracer gas consumption to maintain measurable concentration levels. In the closed-loop configuration, the system was highly sensitive to tracer gas injection because the injected mass remained within the recirculating loop. To maintain a stable steady-state concentration, the injection rate needed to approximately balance the leakage rate, requiring careful adjustment at low injection flow rates. Throughout testing, continuous manual tuning was necessary to maintain concentration stability.

The maximum observed transfer ratio was 7.52% for the plate-type unit and 6.14% for the wheel-type unit under the tested conditions. Overall, the results highlight the importance of pressure management for both technologies while demonstrating that rotary systems require consideration of carryover and other internal transport mechanisms beyond purely static pressure relationships.

7 Summary and Suggestions

This study evaluated the CSA SPE-18 test standard for heat and energy recovery ventilators through laboratory testing of four commercial units, with the objective of assessing test repeatability, developing empirical performance models, and providing actionable feedback for standard refinement. It integrates laboratory testing, performance metric evaluation, empirical model development, and Seasonal Coefficient of Performance (SCOP) analysis for four commercial HRV/ERV units representing plate-type HRV, plate-type ERV, and wheel-type ERV technologies. Energy performance testing was conducted in accordance with CSA SPE-18, including testbed configuration, prescribed indoor and outdoor boundary conditions, airflow balance requirements, and testing tolerances. Core performance metrics—net and recovered sensible and latent heat, apparent and sensible recovery effectiveness, and adjusted sensible recovery efficiency—were calculated following the definitions in the standard (with the exception that ASRE is calculated differently from SHRE as defined in the standard, based on ASRE in C439). Measurement uncertainty and uncertainty propagation were explicitly evaluated to quantify confidence in the reported results.

The experimental data were further used to develop airflow-dependent performance models for fan power and heat exchanger effectiveness. These models were subsequently applied to seasonal simulations across representative climate regions and operating schedules to calculate SCOP for each unit. In addition, tracer gas testing was performed for the plate-type HRV and the wheel-type ERV to assess exhaust air transfer and leakage behavior.

Based on the results of this study, the following feedback and recommendations are provided to support refinement and effective implementation of CSA SPE-18:

1. Despite the presence of multiple measurement uncertainties in airflow, temperature, humidity, and power measurements, repeatability across repeated energy performance tests was found to be good. The three empirical performance models, each developed from an independent test dataset, produced SCOP values that were in close agreement with one another, suggesting that the results are robust across the repeated trials. This indicates that CSA SPE-18 test data are sufficiently robust for model-based seasonal performance evaluation, even when some individual test-point uncertainties are non-negligible.

2. The most severe low-temperature test condition (Condition F) was found to be difficult to reliably achieve and sustain in laboratory settings at Purdue. Furthermore, a single low-temperature test condition is insufficient to identify and characterize the wide range of manufacturer-specific frost control strategies observed across different HRV/ERV designs. During Condition E and Condition F testing, unit behavior is strongly influenced by proprietary control logic, which may include airflow reduction, supply fan cycling, preheating, wheel speed modulation, or protective shutdown. The study recommends that test condition F be made optional, or reformulated to represent condition E' (the lowest achievable temperature). Fur-

thermore, operation at condition F for a full 72 hours is likely to remain impractical for larger commercial systems, so this study recommends that the 72-hour test be omitted or made optional.

3. The study recommends that frost control strategies be explicitly classified by manufacturers (e.g., airflow modulation, preheating, intermittent operation, shutdown-based protection). Low-temperature testing procedures should then be optional and adapted based on the identified control strategy, rather than applying a uniform test sequence to all units. This approach would improve the interpretability, comparability, and diagnostic value of low-temperature test results within the CSA SPE-18 framework.

4. Test conditions and operating tolerances for mass flow rate and airflow balance should be explicitly defined within the standard.

5. The effectiveness metric currently referred to as SHRE should be renamed ASRE, with the corresponding equation updated accordingly. The rationale for this change is discussed in sections 2 and 3 in this report.

6. The terminology "mode" in the SCOP framework should be replaced with "season", with calculations restructured to reflect distinct all-heating and all-cooling seasons. The annual SCOP computation should be removed accordingly.

7. Tracer gas testing for exhaust air transfer and crossflow leakage was found to be technically demanding, requiring highly controlled test facilities, specialized instrumentation, and significant operational cost. While the method provides valuable diagnostic information, it is not readily achievable in many laboratory environments. The study supports maintaining tracer gas testing as an optional component of CSA SPE-18, rather than a mandatory requirement, particularly for laboratories focused on energy performance evaluation.

8. A number of additional corrections to equations and other technical provisions identified during this study should be incorporated into a future revision of the standard.

This study demonstrates that SPE-18 provides a strong and technically sound foundation for laboratory energy performance testing and seasonal efficiency evaluation of HRV/ERV systems. The feedback and recommendations presented herein are intended to support continued refinement of the standard, improve its practical applicability across diverse laboratory facilities, and enhance its ability to capture real-world operational behavior—particularly under low-temperature conditions.

References

AHRI. (2014). *AHRI standard 1060: Performance rating of air-to-air exchangers for energy recovery ventilation equipment* (tech. rep.). Air-Conditioning, Heating, and Refrigeration Institute. Arlington, VA.

CSA. (2019). *CSA C439: Standard methods of test for the rating of the performance of heat/energy-recovery ventilators* (tech. rep.). CSA. Mississauga, ON.

CSA. (2024). *CSA SPE-18:24 – performance testing of heat recovery ventilators and energy recovery ventilators* (tech. rep.). CSA Group. Mississauga, ON.